THESIS
2

MICHIGAN STATE UNIVERSITY LIBRARIES
3 1293 01563 5844

This is to certify that the

dissertation entitled

Multifragmentation in ^{84}Kr + ^{197}Au Collisions at Beam Energies of E/A = 35, 55, 70, 100, 200, and 400 MeV

presented by

Cornelius Fitzgerald Williams

has been accepted towards fulfillment
of the requirements for

PhD degree in Physics

Major professor

Date 1/5/96

MSU is an Affirmative Action/Equal Opportunity Institution

O-12771

LIBRARY
Michigan State
University

PLACE IN RETURN BOX to remove this checkout from your record.
TO AVOID FINES return on or before date due.

DATE DUE	DATE DUE	DATE DUE

MSU Is An Affirmative Action/Equal Opportunity Institution
c:\circ\datedue.pm3-p.1

Multifragmentation in ^{84}Kr + ^{197}Au Collisions at Beam Energies of E/A = 35, 55, 70, 100, 200, and 400 MeV

by

Cornelius Fitzgerald Williams

A DISSERTATION

Submitted to
Michigan State University
in partial fulfillment of the requirements
for the degree of

DOCTOR OF PHILOSOPHY

Department of Physics and Astronomy

1996

ABSTRACT

Multifragmentation in ^{84}Kr + ^{197}Au Collisions at Beam Energies of E/A = 35, 55, 70, 100, 200, and 400 MeV

by

Cornelius Fitzgerald Williams

This dissertation concerns investigations of multifragmentation processes induced by ^{84}Kr + ^{197}Au collisions at beam energies of E/A = 35, 55, 70, 100, 200, and 400 MeV. The experimental data in this dissertation reveal the fragment multiplicities to increase with incident energy to a maximum at about E/A=100 MeV and to decrease thereafter with the onset of nuclear vaporization. The measured fragment charge distributions have been characterized by power law distributions in the fragment charge. The extracted exponents increase monotonically, reflecting an evolution towards steeply falling charge distributions with increasing incident energy. The measured fragment transverse energy distributions are characterized by mean values that increase with incident energy, consistent with the onset of a collective outward expansion. This latter expansion can be placed within a systematics that includes data obtained from collisions of identical projectiles and targets.

These experimental data were compared to several dynamical and statistical multifragmentation models. The Quantum Molecular Dynamics model (QMD) was generally unable to describe the experimental trends, a failure that may be related to the classical heat capacities of the computational nuclei. The Statistical Multifragmentation

Model (SMM), on the other hand, could successfully describe the average fragment multiplicities, and charge distributions, but failed to describe the dependence of the fragment charge distribution on the fragment multiplicity. This latter failure indicates an internal inconsistency within the SMM approach whose origin will require additional theoretical study.

This dissertation is dedicated to my family for all the support that they have given me, and to all of the administrative assistants and secretaries who are always around when you need them.

ACKNOWLEDGMENTS

To finish many things in life one needs the help of others in some form or another. When one has finished these things it is often good to take a look back and thank all of those who have helped reach one's goal.

The first person I like to and must give thanks to is my Lord and Savior, Jesus Christ. He has allowed my to finish this dissertation and he has given me everything I needed to finish it, including the time and the right people to help. And I pray that he will continue to use me as I am needed.

I would also like to say thank you to my family, who have encouraged and supported me in every way possible.

To my advisor, Dr. William Lynch, I say thank you for all of your help and support in working with me to complete this dissertation.

I would also like to say thanks to my advisor committee for their time, Dr. Wolfgang Bauer, Dr. Raymond Brock, Dr. Thomas Glasmacher, and Dr. Wayne Repko.

Before I go any farther, I would like to give my personal thanks to all of the members of the "Miniball" group at MSU from 1990-1996.

To all the collaborators, I must give great thanks to you, since your work was of course a major part of me finishing: Michigan State University, D.R. Bowman, M.

Chartier, J. Dinius, C.K. Gelbke, T. Glasmacher, D.O. Handzy, W.C. Hsi, M.J. Huang, M.A. Lisa, G.F. Peaslee, L. Phair, C. Schwarz, M.B. Tsang, W. Bauer, C.M. Mader; Washington University, G. Van Buren, R.J. Charity, L.G. Sobotka; Indiana University, D. Fox, R.T. deSouza, T.M. Hamilton; Laboratoire National SATURNE, M-C. Lemaire, S.R. Souza; Gesellschaft für Schwerionenforschung, G.J. Kunde, U. Lynen, J. Pochodzalla, H. Sann, W. Trautmann; Instituto de Fisica, Universidade de São Paulo, N. Carlin; Lawrence Livermore National Laboratory, G. Peilert; University of Wisconsin, W.A. Friedman; Institute for Nuclear Research, A. Botvina.

To collect the data for this dissertation we had to use two facilities, the National Superconducting Cyclotron Laboratory at Michigan State University and Laboratoire National SATURNE in Saclay France, and I would like to take the time to thank the staff at both locations for their assistance. Since one of these facilities is in a different country, I would like to thank all of those who made it possible to ship the needed equipment to France and back, especially Graham Peaslee.

Next I would like to give special thanks to the following people; Fan Zhu, Wen-Chien Hsi, James Dinius, Christine Hampton, Njema Frazier, Steve Russell, John "Larry" Bendler, Sergio Souza, Min-Jui Huang, and Sally Gaff, all graduate students whom had to deal with me.

A personal thanks to all those at NSCL that have supported me over the years with words of wisdom and a good push every now and then, especially, Jim Vincent, Allyn McCartney, John Marcotte, John Bonofiglio, Timothy Hoepfner, Jill Franke, Renan Fontus, Jack Ottarson, Greg Humenik, Gary Horner, Andrew Thulin, Jackie Bartlett, and Michal Garbek.

Also I like to give a personal thanks to everyone on the faculty and staff of the Physics Department at Michigan State University, especially Stephanie Holland, Victoria Simon and Jean Strachan.

To Dr. H. Alan Schwettman, Dr. John C. Hiebert, and Dr. Robert A. Kenefick, I say thank you helping me get started in experimental research.

To all fellow graduate students, present, passed, and still to come, I wish you all luck and I will be praying for you.

I realize that I have just given thanks to many people who have help with me finishing this dissertation in one way or another, still there are many that have been left out and to those that I have not mentioned I say thanks and God bless you.

Supported by the National Science Foundation under Grant numbers PHY-90-15255 and PHY-92-14992 and the U.S. Department of Energy under Contract number DE-FG02-87ER-40316.

Table of Contents

List of Tables ix

List of Figures x

Chapter 1 Introduction 1
- 1.1 Background and Motivation 1
- 1.2 Theoretical Background 3
  - *1.2.1 Molecular Dynamics Models* 4
  - *1.2.2 Statistical Models of Fragment Emission* 7
- 1.3 Thesis Organization 11

Chapter 2 Experimental Design 13
- 2.1 Miniball/Miniwall Design 13
- 2.2 Detectors 20
  - *2.2.1 Miniball* 20
  - *2.2.2 Miniwall* 22
  - *2.2.3 Ion Chambers* 22
- 2.3 Target 27
- 2.4 Solid Angle Coverage of the Miniball/Miniwall Array 27
- 2.5 Electronic Readout of the Miniball/Miniwall Array 30
  - *2.5.1 Photomultiplier Tubes* 30
  - *2.5.2 Electronic Setup* 32

Chapter 3 Data Analyses 38
- 3.1 Particle Identification 38
  - *3.1.1 PID Spectrum* 38
  - *3.1.2 Problem Detectors* 46
  - *3.1.3 PDT Spectrum* 46
- 3.2 Energy Calibration 52
  - *3.2.1 Light Output Equation* 52
  - *3.2.2 Saturation Effect* 53
  - *3.2.3 Determining the Parameters* 56

Chapter 4 Data and Calculations 61
4.1 Impact Parameter Selection 61
4.1.1 Equation 61
4.1.2 Total Charge 65
4.2 Intermediate Mass Fragment Multiplicities 65
4.2.1 Experimental Data 69
4.2.2 QMD Calculations 73
4.2.3 QMD+SMM Calculations 74
4.2.4 SMM Calculations 77
4.3 Charge Distributions 80
4.3.1 Experimental Data 82
4.3.2 Comparisons with QMD Calculations 87
4.3.3 Comparisons with QMD+SMM Calculations 87
4.3.4 Comparisons with SMM Calculations 88
4.4 Multiplicity Dependence of the Charge Distribution 91
4.5 Collective Flow 99
4.6 Collective Expansion 101

Chapter 5 Conclusion 106
5.1 Main Results 107
5.1.1 Fragment Yields 107
5.1.2 Charge Distributions 108
5.1.3 Collective Expansion 110
5.2 Future Outlook 111

Bibliography 113

List of Tables

Table 2.1 Information on the number of detectors in a ring, the solid angle of a detector in that ring, the polar angle of a ring, and the range in the polar angle and azimuthal angle that each detector covers. The letter W by the first six rings indicates that these are Miniwall rings........ 24

Table 3.1 Values for the parameters a_i, b_i, and c_i of the functions $\alpha(Z)$, $\beta(Z)$ and $\gamma(Z)$ given in equation 3.9a, 3.9b, and 3.9c, where $Z/A = 0.5$........ 59

Table 4.1 Parameters of SMM calculations chosen so that calculations will match the experimental data........ 78

List of Figures

Figure 1.1 The upper panel shows the temperature, T, versus the excitation energy per nucleon, E^*/A, for 1/3 nuclear matter density, the solid line, and 1/6 nuclear matter density, the dashed line. The bottom panel shows corresponding values for $\langle N_{IMF} \rangle$........ 12

Figure 2.1 Photograph of the Miniball array when mounted in the 92" scattering Chamber at MSU. The picture shows is the main configuration (rings 3' through 11) used in these experiments........ 14

Figure 2.2 Shown here are rings 2-6 of the Miniwall detection array, ring 1 is also attached, but is recessed so it is not visible in the photo. The CsI(Tl) crystal are facing the camera. They are about 3 cm in thickness. The photomultiplier tubes are contained in the μ-metal tubes shown here........ 16

Figure 2.3 A half-plane schematic diagram of the Miniball/Miniwall array. The individual detector rings are labeled, 3' to 11 for the Miniball and 1 to 6 for the Miniwall. While the polar angle for each ring is indicated correctly, the drawing has been simplified and the exact position of each the Miniwall detectors may be slightly different than the actual experimental setup position. The dashed horizontal lines shows where the beam axis is located........ 18

Figure 2.4 These are the front views of the detectors in the Miniball/Miniwall array. They are labeled according to the ring number and by the a letter (B for the Miniball and W for the Miniwall) telling to which array they belong. The number in parentheses tells the number of detectors in that ring........ 19

Figure 2.5 Schematic diagram of individual detector elements [deSo 90]........ 21

Figure 2.6 Photograph of the photomultiplier assembly. The scintillator and the first matching light guide are removed. The ring glued to the μ-metal shield defines the alignment of the can that houses the voltage divider; this can has been removed to expose the voltage divider........ 23

Figure 2.7 A schematic diagram of the Ion Chamber Telescope........ 26

Figure 2.8 Isometric view of the target insertion mechanism mounted on ring 8........ 28

Figure 2.9 Schematic of the upgraded active voltage divider used for the Miniball detectors [Hsi 95]........ 31

Figure 2.10 Schematic electronics diagram of the electronics for the Miniball array alone. The Disc, Split., DGG, Fera, Amp., L.U. and FI/FO labels indicate the locations of discriminators, splitters, delay/gate generators, Fera ADC's, amplifiers, logical units and the fan in/fan out models respectively.. 33

Figure 2.11 This is schematic drawing of the analog signal of the phoswich detectors. The fast, slow, and tail gates of the Miniball are shown. The top numbers show when the gates open after the first gate has opened. The time intervals shown are the time durations for the gates.. 34

Figure 2.12 Schematic diagram of the data acquisition electronics for the Miniwall array alone.. 36

Figure 3.1 Fast versus Slow spectrum of detector 4-18 of the Miniball (ring 4 and position 18) for ^{84}Kr + ^{197}Au collisions at E/A = 55 MeV.. 39

Figure 3.2 Fast versus Slow spectrum of detector 6-8 of the Miniwall (ring 6 and position 8) for ^{84}Kr + ^{197}Au collisions at E/A = 55 MeV... 40

Figure 3.3 Tail versus Slow spectrum of detector 3'-20 of the Miniball (ring 3' and position 20) for ^{84}Kr + ^{197}Au collisions at E/A = 55 MeV.. 41

Figure 3.4 Tail versus Slow spectrum of detector 6-8 of the Miniwall (ring 6' and position 8) for ^{84}Kr + ^{197}Au collisions at E/A = 55 MeV... 42

Figure 3.5 This is a plot of a Slow versus PID spectrum of detector 3'-20 of the Miniball. Visible are the different charge lines making it easier to draw the gates for particle identification when analyzing the data.. 44

Figure 3.6 This is a plot of a Slow versus PID spectrum of detector 6-8 of the Miniwall. Visible are the different charge lines making it easier to draw the gates for particle identification when analyzing the data.. 45

Figure 3.7 Tail versus Fast spectrum of detector 8-5 of the Miniball (ring 8 and position 5) from the ^{84}Kr + ^{197}Au collisions at E/A = 55 MeV...................................... 47

Figure 3.8 This is a plot of the Tail versus Slow and the variables that are used to make the PDT function. In the plot you can clearly see the relationships between Tail_1, Tail_2 and Tail_r.. 49

Figure 3.9 This is a plot of a PDT versus Slow spectrum of detector 3'-20 of the Miniball. Visible are the Hydrogen isotopes, protons, deuterons, and tritons, as well as the Helium isotopes, 3He and ^{4}He.. 50

Figure 3.10 This is a plot of a PDT versus Slow spectrum of detector 6-8 of the Miniwall. Visible are the Hydrogen isotopes, protons, deuterons, and tritons, as well as the Helium isotopes, 3He and ^{4}He.. 51

Figure 3.11 The upper panel shows the results obtain for the fractional deviation when using ^{12}C as the reference particle. The line is linear fit to the ^{12}C data and defines the function f(Ch#), the fractional deviations. The light output for the Miniball and Miniwall was less then the output predicted by equation 3.8. The lower panel shows how the result for f(Ch#) obtained with ^{12}C compares to the deviation observed from the ^{6}Li data 55

Figure 3.12 This is the calibration curve with the saturation correction for the ^{4}He and the ^{12}C particles. The top line is the ^{4}He energy calibration curve and the bottom line is the ^{12}C energy calibration curve using equation 3.8. The filled in symbols are the energy calibration data points using the saturation correction. The open symbols are the energy calibration data points without the saturation correction 57

Figure 3.13 This plot shows the calibration curves for the detected particles with Z/A = 0.5. Also plotted are the calibration data for: ^{4}He, (solid circles), ^{6}Li, (open fancy crosses), ^{10}B, (crosses), ^{12}C, (open circles), ^{14}N, (solid squares), ^{16}O, (open diamonds), and ^{20}Ne, (open squares) particles 60

Figure 4.1 The normalized probability distributions for the charged particle multiplicity N_C for E/A = 35, 55, 70, 100, 200, and 400 MeV. The reduced impact parameter, $\hat{b}$, is shown at the top of the panels. The open circle indicates the middle impact parameters, $0.3 < \hat{b} < 0.66$ 63

Figure 4.2 The dependence of reduced impact parameter, $\hat{b}$, upon the charged particle multiplicity, N_C, for E/A = 35, 55, 70, 100, 200, and 400 MeV 64

Figure 4.3 The dependence of the total charge, $\langle Z_{tot} \rangle$, on the total charged particle multiplicity for E/A = 35, 55, 70, 100, 200, and 400 MeV 66

Figure 4.4 The dependence of the total charge, $\langle Z_{tot} \rangle$, upon the reduced impact parameter, $\hat{b}$, for E/A = 35, 55, 70, 100, 200, and 400 MeV 67

Figure 4.5 The dependence of the mean intermediate mass fragment multiplicity, $\langle N_{IMF} \rangle$, upon the charged particle multiplicity for E/A = 35, 55, 70, 100, 200, and 400 MeV 70

Figure 4.6 The dependence of the mean intermediate fragment multiplicity, $\langle N_{IMF} \rangle$, upon the reduced impact parameter, $\hat{b}$, for E/A = 35, 55, 70, 100, 200, and 400 MeV 71

Figure 4.7 The upper panel shows a comparison between the measured mean charge particle multiplicity, <N_C>, and QMD calculations for central collisions as a function of incident energy. The lower panel shows the corresponding values for the mean IMF multiplicity, <N_{IMF}>. The solid dots are the experimental data points. The corresponding statistical uncertainties are smaller than the data points. The dashed lines are from unfiltered QMD calculations. The solid and dotted lines are QMD calculations filtered by the experimental acceptence. The solid square is the prediction of QMD calculations without the Pauli potential.. 72

Figure 4.8 The upper panel shows a comparison between the measured mean charge particle multiplicity, <N_C>, and QMD+SMM calculations for central collisions as a function of incident energy. The lower panel shows the corresponding values for the mean IMF multiplicity, <N_{IMF}>. The solid dots are the experimental data points. The corresponding statistical uncertainties are smaller than the data points. The dashed lines are from unfiltered QMD+SMM calculations. The solid and dotted lines are from QMD+SMM calculations filtered by the experimental acceptance........................ 75

Figure 4.9 The upper panel shows a comparison between the measured mean charge particle multiplicity, <N_C>, and SMM calculations for central collisions as a function of incident energy. The lower panel shows the corresponding values for the mean IMF multiplicity, <N_{IMF}>. The solid dots are the experimental data points. The corresponding statistical uncertainties are smaller than the data points. The dashed and dot-dashed lines describe unfiltered SMM calculations which include radial and rotational flow, respectively. The dotted and solid lines are the corresponding filtered SMM calculations.. 79

Figure 4.10 The probability of emitting a fragment of charge, Z, per collision in center collision at all six incident energies. The solid dots are the experimental data points. The statistical uncertainties of the data are smaller than the data points. The solid line is the power law fit.. 83

Figure 4.11 Comparison of the energy dependence of the charge distribution exponent τ from the data to QMD and QMD+SMM calculations for central ^{84}Kr + ^{197}Au collisions. The solid line describes the τ values from the QMD calculations using the Pauli potential. The dashed line describes the τ values from QMD+SMM calculations. The solid square is the τ value at E/A = 50 MeV from a QMD calculation that does not use the Pauli potential. The solid points are values for τ extracted from the experimental data.. 84

Figure 4.12 The probability of emitting a charge, Z, per mid-impact parameter collision at the six incident energies. The solid dots are the experimental data points. The statistical uncertainties of the data are smaller than the data points. The solid lines are the power law fits.. 85

Figure 4.13 Comparison of the energy dependence of the charge distribution exponent τ from the data to QMD and QMD+SMM calculations for mid-impact parameter ^{84}Kr + ^{197}Au collisions. The solid line describes the τ values from the QMD calculations using the Pauli potential. The dashed line describes the τ values from QMD+SMM calculations. The solid square is a τ value at E/A = 50 MeV from a QMD calculation that does not use the Pauli potential. The solid dots are values for τ extracted from the experimental data 86

Figure 4.14 Comparison of the measured energy dependence of the charge distribution exponent τ from the data to SMM calculations for central ^{84}Kr + ^{197}Au collisions. The dashed and dashed-dotted lines describes the τ values from SMM calculations assuming radial and rotational flow, respectively, before secondary decay is allowed to occur. The dotted and solid lines describes the corresponding τ values for SMM calculations after secondary decay of the excited fragments. The solid dots are values for τ extracted from the experimental data 89

Figure 4.15 Charge conservation parameter *c* as a function of transverse energy E_t for the ^{84}Kr + ^{197}Au system at incident energies of E/A = 35 - 400 MeV 93

Figure 4.16 IMF multiplicity gated α-α correlation functions for the ^{84}Kr + ^{197}Au system at E/A = 35 MeV and $E_t < 100$ MeV 95

Figure 4.17 Left hand panel: *c* plotted as a function of incident energy and central collisions for data (solid points) and SMM predictions (open points). Right hand panel: *c* plotted as a function of source size used in the SMM calculations for E/A = 200 MeV. The doubled dashed lines bound the value for *c* consistent with the experimental data 97

Figure 4.18 Comparison of the measured mean transverse energy, $<E_t>$, (solid points) to SMM calculations with radial (dashed lines) and rotational (solid lines) flow as a function of fragment charge at E/A = 35, 55, 70, 100, 200, and 400 MeV and $\hat{b} < 0.25$ 100

Figure 4.19 Comparison of the measured mean transverse energy, $<E_t>$, (solid points) to QMD calculations without the Pauli potential (solid squares) at E/A = 50 MeV, QMD and QMD+SMM calculations with the Pauli potential (solid and dashed lines, respectively), as a function of fragment charge at E/A = 35, 55, 70, 100, 200, and 400 MeV and $\hat{b} < 0.25$. Note, charged particles are not produced with Z > 4 within the QMD model for 35 MeV at this reduced impact parameter 102

Figure 4.20 The mean collective velocity. <β>, versus the excitation energy per nucleon, E^*/A of the participant source. The solid squares are from the analysis of the ^{84}Kr + ^{197}Au system. The other data are described in the text..104

Chapter 1

Introduction

1.1 Background and Motivation.

The experimental exploration of the properties of bulk nuclear matter at extrem densities and temperatures began in earnest over a decade ago. A series of experiments the Bevalac at Lawrence Berkeley Laboratory (LBL) [Gutb 89a, Stöc 86] initiated th prospects for a creation of nuclear shock wave in supersonic nucleus-nucleus collision and related investigations are now being carried out at places like the Nationa Superconducting Cyclotron Laboratory at Michigan State University (NSCL), th Gesellschaft für Schwerionenforschung, (GSI) and the Alternating Gradient Synchrotro (AGS) at Brookhaven National Laboratory. These experiments have succeeded i placing constraints upon the compressibility of nuclear matter at high densities. Aroun the same time, an interest in the properties of nuclear matter at subnuclear densities wa aroused by a series of pioneering measurements at Fermilab, NSCL and the 88" cyclotro at LBL [Hirs 84, Chit 83, Sobo 83]. Discussion of these latter measurements in th context of a low density phase transition of liquid-gas character [Curt 83, Saue 76, Bon 85a, Gros 82, Fai 82] played an important role in increasing the interest in this area and continues to motivate work, including the present dissertation, in this area.

The emission of intermediate mass fragments (IMF's; $3 \leq Z \leq 20$) is the mai observable that is presumed to be connected with a transition between liquid and gaseou phases of nuclear matter [Curt 83, Hirs 84, Gros 82, Bond 85a]. However, the notion of liquid-gas phase transition is already present in evaporation theories of nuclear deca wherein nucleons and light clusters (d, t, α) are emitted from the surfaces of a hot nucleu [Weis 37]. The emission of heavier IMF's at low emission rates is a prediction o evaporation theories [Frie 83a, Lync 87]. The observation of very high IM multiplicities, however, lies outside of the realm of prediction of evaporation theorie [Bowm 91, Frie 83a]. Such an observation suggests a different mode of decay via a bul disintegration [Bond 85a, Frie 83a, Gros 82] which, if it occurs over an appropriat timescale, could allow the existence of a phase equilibrium between nuclear liquid drop (IMF's) and vapor (nucleons and light particles) within the breakup volume. Thi possibility, if this occurs, differs significantly from the phase changes which occur durin evaporation since a hot evaporating nucleus can never be in equilibrium with th surrounding vacuum.

After initial inclusive fragmentation experiments, there was a waiting period i the latter part of the last decade during which various multifragment detection arrays wer constructed. At the NSCL, the Miniball array was completed and began its firs experiments in 1990. Soon after that, it was determined that bulk multifragmen disintegrations were observed in collisions between heavy nuclei [Bowm 91, deSo 91]. then becomes important to determine the experimental domain in incident energy an projectile and target masses for the optimal experimental exploration of this new deca mechanism. Therefore, the Miniball group, in conjunction with groups at Washingto University, Saclay and GSI agreed to carry out a set of experiments in Europe using th

Miniball/Miniwall array. Two sets of measurements were done, the first one was of measurements of ^{197}Au + ^{197}Au collisions at the Schwerionen Synchrotron accelerator located at GSI, and the other was a series of measurements of ^{84}Kr collisions at the Laboratoire National Saturne (LNS), synchrotron accelerator loc Saclay. These experiments allowed us to map out the fragmentation process as a f of incident energy and impact parameter.

This dissertation concerns itself with the measurement of ^{84}Kr + ^{197}Au re at SATURNE and with a follow up experiment at the lower energies using beam the NSCL. Altogether reactions at six different incident energies, E/A = 35, 55, 7 200, and 400 MeV were measured, giving a good systematic information over a u broad dynamic range. These measurements reveal that the beams provided by the are close to ideal for the examination of multifragmentation processes. In c central collisions at significantly higher energies produce breakup configurations too highly excited and expand too violently for any possibility of phase equilibrium

1.2 Theoretical Background

Theoretical approaches can be subdivided into models which try to calc equilibrated multifragment decay and others which try to model the time evolutio system via dynamical or rate equation approaches. Among models which equilibrium one can count multiparticle phase space models like the St Multifragmentation Model (SMM) [Bond 85a, Botv 87], Berlin [Gros 82], or [Bert 83, Fai 82] approaches. Time dependent approaches include the eva approaches like the Expanding Evaporation Source (EES), model [Frie 88], or m dynamical models such the Quantum Molecular Dynamics (QMD) model [Peil 89] or Quasiparticle Dynamical models (QPD) [Boal 83]. Clearly, an accurate fully dynamical approach is preferable to any other, since it should also relax and describe an equilibrated decay configuration given sufficient time.

1.2.1 Molecular Dynamics models

Prior to this dissertation, considerable credibility was given to the results of molecular dynamics calculations [Peil 91, Peil 92] based upon numerical techniques similar to those employed in the solution of the semi-classical Boltzman - Uehling - Uhlenbeck (BUU), or Vlasov - Uehling - Uhlenbeck (VUU) equation [Bert 83, Pan 95]. Probably the most frequently employed models of this type are the QMD models developed by the Frankfurt-Nante collaboration [Aich 86, Peil 89].

The initial implementation of this approach differs little conceptually from the BUU, VUU, or Landau-Vlasov theories [Greg 87]. The nucleons are represented by Wigner transforms of the form [Aich 86, Peil 89]:

$$f(\vec{r},\vec{p},t)=\left(\frac{1}{\pi\hbar}\right)^3 \exp\left(\frac{-[\vec{p}_0-\vec{p}(t)]^2 L^4-[\vec{r}_0-\vec{r}(t)]^2\hbar^2}{\hbar^2 L^2}\right). \tag{1.1}$$

Solutions within the QMD model are attained by classically propagating nucleons according to Hamilton's equations of motion and the Hamiltonian:

$$H=\sum_i \frac{\vec{p}_{oi}^{\,2}(t)}{2m}$$

$$+\frac{1}{2}\sum_{i\neq j}\int d\vec{r}_i d\vec{r}_j d\vec{p}_i d\vec{p}_j \left\{V_{ij}^{\mathrm{Strong}}+V_{ij}^{\mathrm{Coul}}+V_{ij}^{\mathrm{Yuk}}\right\} f(\vec{r}_i,\vec{p}_i,t) f(\vec{r}_j,\vec{p}_j,t) \tag{1.2}$$

Here, $\vec{p}_{oi}$ is the average of the Guassian wave packet of the ith particle, m is the mass o the particle, V_{ij}^{Coul} is the two body Coulomb potential and V_{ij}^{SK} is the two body stron potential, approximated here by an effective interaction of the Skyrme type. The tw body Skyrme potential is of the form:

$$V^{SK} = t_1 \cdot \delta\left(\vec{r}_i - \vec{r}_j\right) + t_2 \cdot \delta\left(\vec{r}_i - \vec{r}_j\right) \cdot \delta\left(\vec{r}_i - \vec{r}_k\right) \tag{1.3}$$

and V^{Yuk} is a local Yukawa term of the form:

$$V^{Yuk} = \frac{V_{Yuk}^{o} \cdot \exp\left(-\left|\vec{r}_1 - \vec{r}_2\right| / \gamma_{Yuk}\right)}{\left|\vec{r}_1 - \vec{r}_2\right| / \gamma_{Yuk}} . \tag{1.4}$$

In addition to these two body effective potentials described by the Skyrme interaction scattering via the residual interaction is implemented by a classical collision integra which incorporates phase-space “Pauli” blocking factors in the final state. This Pauli blocking correction to the collision integral is the essential ingredient that distinguishe this model from classical molecular dynamics. Unfortunately, this distinction is mor formal than real, since it is practically impossible to completely enforce the Pau exclusion principle with this approach. Calculations reveal that both ground state an weakly excited nuclei are unstable with respect to decay via pathways that a inconsistent with the Pauli exclusion principle. This failure renders the calculation unreliable when extended over long time periods. It therefore prevents getting a accurate description of the multifragment disassembly in collisions at lower incide energies where the decay timescales are characteristically long.

To address this deficiency, theorists tried to improve the implementation of Pauli principle by introducing a two-body "Pauli" potential which acts in phase space [Peil 89, Boal 83]. In the case of the "QMD with Pauli potential" model, the Hamiltonian is written in the following manner:

$$
\begin{aligned}
H = {} & \sum_{i} \frac{\vec{\mathrm{p}}_{oi}^{2}(\mathrm{t})}{2\mathrm{m}} \\
& + \frac{1}{2}\sum_{i\neq j}\int d\vec{\mathrm{r}}_i d\vec{\mathrm{r}}_j d\vec{\mathrm{p}}_i d\vec{\mathrm{p}}_j \left\{\mathrm{V}_{ij}^{\mathrm{Strong}} + \mathrm{V}_{ij}^{\mathrm{Coul}} + \mathrm{V}_{ij}^{\mathrm{Yuk}}\right\} f(\vec{\mathrm{r}}_i,\vec{\mathrm{p}}_i,\mathrm{t}) f(\vec{\mathrm{r}}_j,\vec{\mathrm{p}}_j,\mathrm{t}) \\
& + \frac{1}{2}\sum_{i\neq j}\int d\vec{\mathrm{r}}_i d\vec{\mathrm{r}}_j d\vec{\mathrm{p}}_i d\vec{\mathrm{p}}_j \left\{ \mathrm{V}_{\mathrm{Pau}}^{0}\left[\frac{\hbar}{\vec{\mathrm{q}}_{\mathrm{o}}\vec{\mathrm{p}}_{\mathrm{o}}}\right]^{2} \exp\left\{-\frac{\vec{\mathrm{r}}_{ij}^{2}}{2\vec{\mathrm{q}}_{\mathrm{o}}^{2}} - \frac{\vec{\mathrm{p}}_{ij}^{2}}{2\vec{\mathrm{p}}_{\mathrm{o}}^{2}}\right\} \mathrm{d}_{\mathrm{t}_i \mathrm{t}_j} \mathrm{d}_{\sigma_i \sigma_j} \right\} \\
& \times f(\vec{\mathrm{r}}_i,\vec{\mathrm{p}}_i,\mathrm{t}) f(\vec{\mathrm{r}}_j,\vec{\mathrm{p}}_j,\mathrm{t}) \qquad (1.5)
\end{aligned}
$$

Values for the parameters in equation 1.1 and equation 1.2 are given in ref. [Peil 91]. The inclusion of the Pauli potential makes it possible to create stable computational ground state nuclei. This, in turn, permits the extension of numerical simulations to long breakup timescales.

While permitting a numerically stable technique for calculating dynamical multifragmentation, the "QMD with Pauli potential" model displays features that are not consistent with quantum mechanics. For example, the repulsive Pauli potential scatters particles to prevent the overpopulation of phase space. Such scattering corresponds to a change of state in quantum mechanics. True Pauli blocking, on the other hand, prevents a change of state whenever the collisional rearrangement would result in a phase space overpopulation. Thus, true Pauli blocking lengthens the mean free path of particles near the Fermi surface while the Pauli potential actually shortens the mean free path [Prat 95, Wile 91]. A second shortcoming is that the computational nuclei simulated by the "QMD with Pauli potential" model and other similar models with "Pauli" potentials, all exhibit classical heat capacities [Peil 91, Lync 87].

This latter limitation is particularly vexing because it prevents the realistic modeling of the later stages of multifragmentation whenever such stages occur over timescales commensurate with statistical emission timescales [Lync 87]. Unphysically low temperatures occur in "QMD with Pauli Potential" model calculations in which large classical heat capacities replace the smaller quantal heat capacities extrapolated from compound nuclear decay measurements [Lync 87]. When this happens, statistical emission processes are greatly inhibited due to the resulting unphysically low temperatures.

These limitations were not apparent at the initiation of this dissertation but became very apparent after comparisons between our data and other similar data to the results of simulations using the QMD model with the Pauli potential. These comparisons are presented in Chapter IV of this dissertation.

1.2.2 Statistical Models of Fragment Emission

Fragment yields can be calculated within statistical models in the limit of global equilibrium [Bond 85a, Botv 87, Gros 82, Fai 82, Pan 85] or via equations which describe the emission rates [Frie 83a, Frie 88, Boal 83]. Investigations using either approach can reproduce the available multifragmentation data provided that fragmentation occurs at subnuclear density. Within global equilibrium approaches, the requirement that roughly spherical fragments do not overlap dictates multifragment decay configurations with densities less than a third of normal nuclear matter density. Within the Expanding Evaporation Source (EES) rate equation approach of Friedman [Frie 88], the relative fragment multiplicities are only enriched to the level that is experimental observed, provided the system expands to less that 0.4 normal nuclear matter density [Bowm 91, Frie 88]. Thus, it is a common prediction of either approach that multifragmentation principally occurs after the system expands to subnuclear density.

In this dissertation, comparisons have been primarily made to the Statistical Multifragmentation Model (SMM) of Botvina, Bondorf and collaborators [Bond 85, Botv 87]. In this model, fragments and light particles are consider as Boltzman particles moving in a reduced free volume:

$$V=\chi V_o \tag{1.6}$$

In this equation $V_o = 4\pi r_o^3 A_{tot}/3$ with $r_o = 1.17$ fm, A_{tot} is the total nucleon number, and χ is a model parameter, described below; V is the total volume of the system minus the volume occupied by the fragments.

Accurately sampling the multiparticle phase space is difficult. This is achieved in the SMM approach using the following steps [Bond 85, Botv 87]:

(i) The number of ways to break a prefragment of mass A, into fragments with a multiplicity, M, is computed in a combinatorial approach [Bond 85, Snep 88]. These partitions $\{N_{A,Z}\}$are then sampled according to their combinatorial weights.

(ii) Each partition $\{N_{A,Z}\}$ has a well defined set of fragments and nucleons. An additional multiplicative weight coming from the phase space for each fragment is assigned to each partition $\{N_{A,Z}\}$and is written as follows:

$$W(\{N_{A,Z}\}) = \exp[S(\{N_{A,Z}\},T,V)]. \tag{1.7}$$

Here the total entropy is written as:

$$S(\{N_{A,Z}\},T,V) = \Sigma_{A,Z} N_{A,Z}\, S_{A,Z}(T). \tag{1.8}$$

In this expression, $N_{A,Z}$ is the multiplicity of fragments of A and Z, $S_{A,Z}(T)$ is the "entropy" of individual fragments of A and Z, and T is the "temperature" of the decay configuration. In defining the "entropy" and "temperature" an implicit ensemble averaging over the various ways of sharing energy within a partition was taken.

(iii) Both entropies and excitation energies for individual fragments were calculated from an empirical liquid drop expression for the free energy:

$$F_{A,Z}(T) = -T\ln\left(g_{A,Z}\frac{\chi V_o A}{\lambda^3}\right) + \frac{T}{N_{A,Z}}\ln N_{A,Z}! + \left(W_o - \frac{T^2}{\varepsilon_o}\right)A$$

$$+\beta(T)A^{2/3} + \gamma\frac{(A-2Z)^2}{A} + \frac{3}{5}\frac{Z^2 e^2}{R_{A,Z}}\left(1 - \frac{1}{(1+\chi)^{1/3}}\right). \tag{1.9}$$

Here, $g_{A,Z}$ is the degeneracy factor which used for light fragments and is set equal to 1 for A > 4, W_o = -16 MeV is the bulk energy parameter, ε_o = 16 MeV, $\chi V_o = V$, is the free volume that the fragment moves in, and the asymmetry coefficient γ = 25 MeV. The nucleon thermal wavelength, λ, is given by:

$$\lambda = \left(\frac{2\pi\hbar^2}{mT}\right)^{1/2}, \qquad (1.10)$$

where m is the mass of a nucleon. The surface free energy parameter β(T) is zero for $T \geq T_c$, but for $T < T_c$ has the following form:

$$\beta(T) = \beta_0 \left(\frac{T_c^2 - T^2}{T_c^2 + T^2}\right)^{5/4}, \qquad (1.11)$$

where β_o is a constant with the value of 18 MeV. The ratio of the saturation density over the freezeout density is given by the parameter χ. In the model χ is related to the multiplicity M of the emitted particles by:

$$\chi = \left[1 + \frac{d}{R_0}\left(M^{1/3} - 1\right)\right]^3 - 1, \qquad (1.12)$$

where $R_o = 1.17\,A_0^{1/3}$, and 2d is the crack width between fragments at freezeout. The "temperature" of the system is calculated from the total free energy by requiring a fixed energy in the event. The "entropy" of an individual fragment $S_{A,Z}$ (T) can be calculated from the empirical liquid drop formula for the free energy, $F_{A,Z}$ (T), given in equation 1.9. Then $S(\{N_{A,Z}\},T,V)$ is obtained by summing $S_{A,Z}$ (T) over fragments and a multiplicative weight $W(\{N_{A,Z}\})$ can be assigned for each partition.

(iv) The secondary decay of the various excited fragments at "temperature" T is then calculated.

(v) The experimental observables are obtained by averaging over simulated events generated in a Monte Carlo approach. The calculations do consider the various weights of each partition and the various decay pathways for the excited fragments.

The top panel in figure 1.1 shows the relationship between temperature and total excitation energy per nucleon predicted within this approach, where the total system is $Z_{tot} = 158$ and $A_{tot} = 394$. For 3 MeV $\leq E^{*}/A \leq$ 8 MeV, the temperature is predicted to increase only gradually with fragment mass. Proponents of this model believe this behavior to be an indicative of the enhanced heat capacity characteristic of a phase transition from a Fermi liquid to a nucleonic gas. The bottom panel of figure 1.1 shows the corresponding relationship between the fragment multiplicity and the total excitation energy per nucleon. In the domain where the temperature remains roughly constant, the fragment multiplicity grows rapidly. At higher values of the excitation, energy where the temperature begins to climb rapidly, the fragment multiplicity declines sharply. Advocates of this model interpret this decline as a consequence of the onset of vaporization.

1.3 Thesis Organization

Chapter 2 describes the experimental setup, and Chapter 3 describes the spectra and analysis procedures. Chapter 4 describes the final physics results and provides comparisons to various fragmentation models. Chapter 5 provides a summary and discussion of the physics conclusions of this dissertation. An outlook toward future investigations is also discussed.

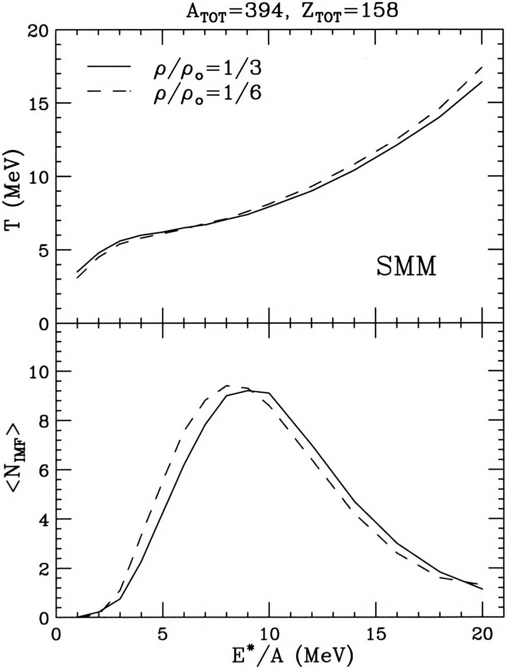

Figure 1.1 The upper panel shows the temperature, T, versus the excitation energy per nucleon, E^*/A, for 1/3 nuclear matter density, the solid line, and 1/6 nuclear matter density, the dashed line. The bottom panel shows corresponding values for $<N_{IMF}>$.

Chapter 2

Experimental Design

To cover the wide range of incident energies used by this thesis, it was necessary to conduct experiments at two different facilities. The measurements for the lower incident energies of E/A = 35, 55 and 70 MeV were performed at the National Superconducting Cyclotron Laboratory (NSCL) located at Michigan State University (MSU) in East Lansing, Michigan. The measurements at the higher incident energies of E/A = 100, 200 and 400 MeV were performed at the Laboratoire National SATURNE (LNS) located in Saclay, France. The beams at LNS had lower intensities than the beams at NSCL which made the analysis more difficult to carry out.

This chapter describes the two experimental setups, including the detectors, the electronics and the geometrical arrangements in the scattering chamber. While there are differences that exist between the two experimental setups, these differences are relatively minor. For this reason the Miniball/Wall array is described first in general terms, and the changes of the components that relate specifically to the SATURNE or NSCL experiments are explained when describing those components.

2.1 Miniball/Miniwall Array

The Miniball phoswich detector array is designed to operate in a vacuum vessel. The layout of the Miniball/Miniwall array is described in this section and a description of

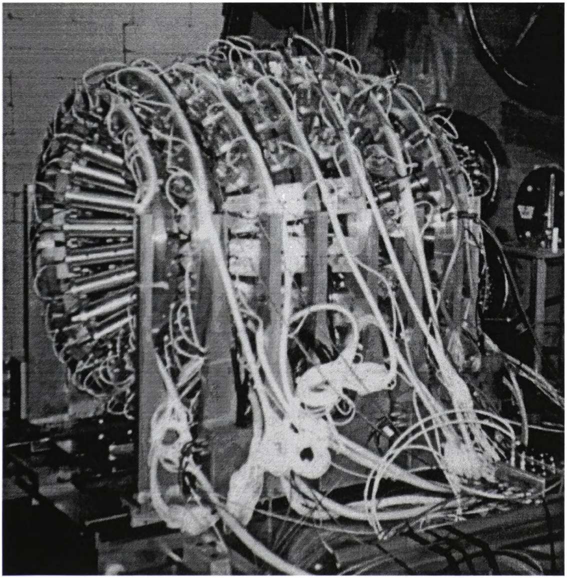

Figure 2.1 Photograph of the Miniball array when mounted in the 92" scattering Chamber at MSU. The picture shows is the main configuration, (rings 3' through 11), used in these experiments.

the individual detectors is given in section 2.2. Figure 2.1 is a photo of the Miniball taken while it was in the 92 inch chamber at NSCL. The array consists of 11 independent coaxial rings centered the beam axis. For easy assembly and servicing, the individual rings are mounted on separate base plates that slide along two precision rails. The individual detectors can be removed or inserted without interfering with the alignment of neighboring detectors. The entire assembly is placed on an adjustable mounting structure which allows the array to be aligned to the beam axis.

The Miniwall array shown in figure 2.2 is also a phoswich detector array designed to work in a vacuum. It is constructed with six azimuthally symmetric rings where all the detectors in a ring are at the same polar angle. These rings are not mounted on individual supports like those in the Miniball; instead they are mounted on one plate. This plate is designed to fit on the same precision rails and use the same cooling system as the Miniball.

The rings and detector mounts are made out of aluminum, which provides good thermal conductivity between detectors and mounting structure. This allows the heat generated by the photomultiplier voltage divider network to conduct into the array superstructure where the heat is removed from the Miniball/Miniwall array by a cooling bar attached to the base plates. These bases are cooled by alcohol or other refrigerants which flow through an attached cooling line. By regulating the temperature of the cooling fluid, the temperature of the base plates are held at 15° C, leaving the individual detectors at approximately room temperature. This ensures that the array will reach an equilibrium temperature quickly when the phototubes are at full bias.

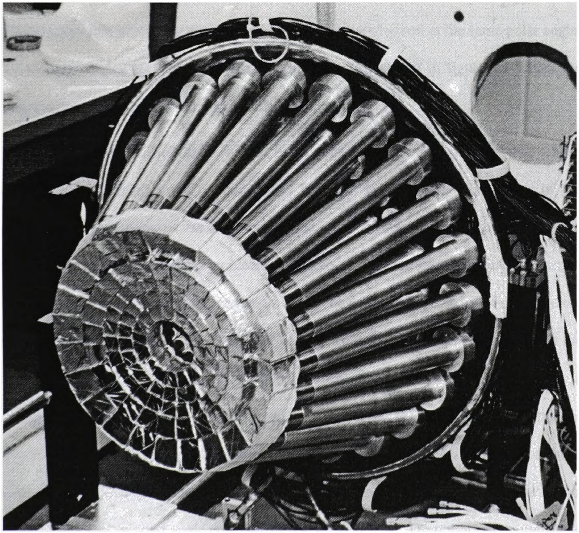

Figure 2.2 Shown here are rings 2-6 of the Miniwall detection array, ring 1 is also attached, but is recessed so it is not visible in the photo. The CsI(Tl) crystals are facing the camera. They are about 3 cm in thickness. The photomultiplier tubes are contained in the μ-metal tubes shown here.

Figure 2.3 shows a half-plane section of the array in the vertical plane containing the beam axis. The individual rings are labeled by ring numbers 1-6 for the Miniwall and 3'-11 for the Miniball, which increase in numbers from the forward to backward angles. The number of detectors in each ring is given in the parentheses next to the ring number. All detectors in a given ring are identical in shape and are located at the same polar angle. These polar angles are defined in the coordinate system shown in figure 2.3 where the target is the origin and the beam axis is the polar axis.

The angular distributions of the emitted particles are strongly forward peaked [Kim 92]. To equalize the counting rates between detectors the solid angles of the detectors at forward angles are smaller than those at backward angles. This variation in solid angles is achieved mainly by placing detectors at different distances from the target, allowing the size of the detectors to remain fairly constant. Still the shape of the detectors changed from ring to ring. The geometries of the front faces of the detectors (which are made from CsI(Tl) crystals) are shown in Figure 2.4. The front faces of each detector is labeled according to the ring number. In order to reduce the cost of fabrication, the edges of the front faces of the crystals were machined flat instead of curved, which could have allowed the polar angle corresponding to the edges of the detectors to be constant. This resulted in a loss of solid angle coverage on the order of 2%. These flat edges contribute to a loss in the solid angle that is comparable in magnitude to the loss in solid angle resulting from the gaps between individual detectors (which is needed to make allowances for mechanical tolerances and to allow optical isolation between neighboring crystals).

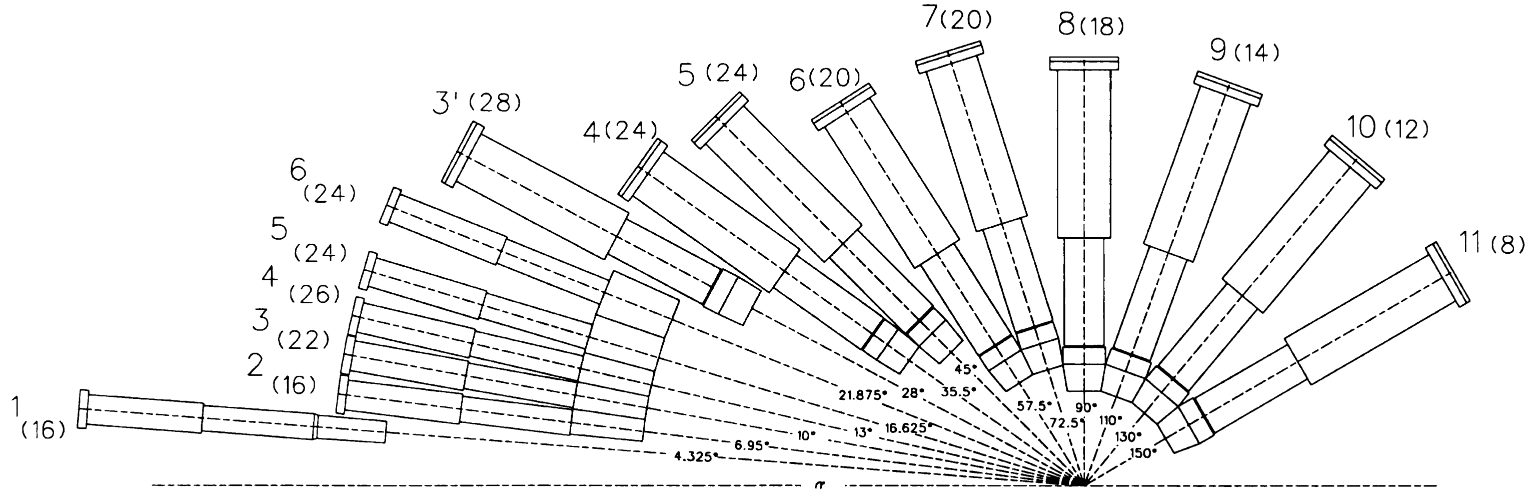
1 (16)
2 (16)
3 (22)
4 (26)
5 (24)
6 (24)
3' (28)
4(24)
5 (24)
6(20)
7(20)
8(18)
9 (14)
10 (12)
11 (8)
4.325°
6.95°
10°
13°
16.625°
21.875°
28°
35.5°
45°
57.5°
72.5°
90°
110°
130°
150°

Figure 2.3 A half-plane schematic diagram of the Miniball/Miniwall array. The individual detector rings are labeled, 3’ to 11 for the Miniball and 1 to 6 for the Miniwall. While the polar angle for each ring is indicated correctly, the drawing has been simplified and the exact position of each the Miniwall detectors may be slightly different than the actual experimental setup position. The dashed horizontal lines shows where the beam axis is located.

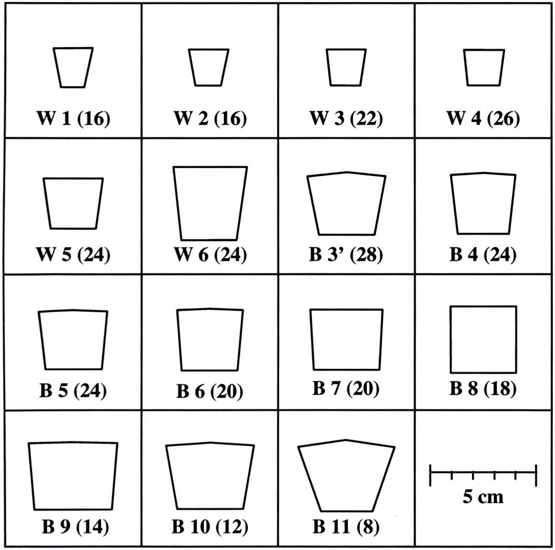
W 1 (16)
W 2 (16)
W 3 (22)
W 4 (26)
W 5 (24)
W 6 (24)
B 3' (28)
B 4 (24)
B 5 (24)
B 6 (20)
B 7 (20)
B 8 (18)
B 9 (14)
B 10 (12)
B 11 (8)
5 cm

Figure 2.4 These are the front views of the detectors in the Miniball/Miniwall array. They are labeled according to the ring number and by the a letter, (B for the Miniball and W for the Miniwall) telling to which array they belong. The number in parentheses tells the number of detectors in that ring.

The configuration of the arrays in the NSCL experiment differed from that at SATURNE by the inclusion of ring 1 of the Miniwall, and by the replacement of the phoswich detectors directly over the beam axis in rings 3' - 11 with Ion Chamber, Silicon, CsI(Tl) telescopes. These Ion Chamber telescopes were constructed at Indiana University, and were included to provide information about the fragment energy spectra at energies below the Miniball particle identification thresholds.

2.2 Detectors

2.2.1 Miniball

Each phoswich detector of the array is composed of a 40 μm (4 mg/cm^2) thick plastic scintillator and a 2 cm thick CsI(Tl) scintillator crystal. The plastic scintillator foil was spun from a Bicron BC-498X scintillator solution [deSo 90]. Figure 2.5 is a schematic of the detector design. To retain flexibility in the choice of scintillator foil thickness, the foil was placed on the front face of the CsI(Tl) crystal without any adhesive. The shape of the CsI(Tl) is dependent on which ring the detector is in. The back face of the CsI(Tl) scintillator is glued to a flat ultraviolet transmitting lightguide (UVT) Plexiglas with optical cement (Bicron BC600). This light guide is 12 mm thick and matches the geometrical shape of the back face of the CsI(Tl) crystal. This light guide is glued to a second cylindrical light guide, a piece of UVT Plexiglas 9.5 mm thick and 25 mm in diameter. The cylindrical guide is then glued to the front window of the photomultiplier tube, a Burle Industries model C83062E. Both the front and back faces of the CsI(Tl) crystals were polished so as to allow the transmission of light through them. The sides are sanded and wrapped with white Teflon tape to help reflect internal light and to prevent cross talk between neighboring detectors. To farther isolate the detectors from

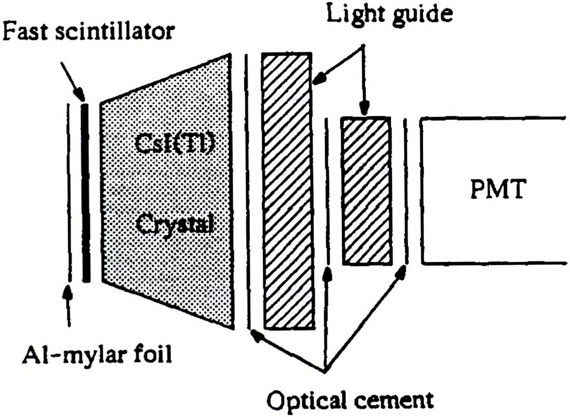
Light guide
Fast scintillator
CsI(Tl)
Crystal
PMT
Al-mylar foil
Optical cement

Figuer 2.5 Schematic diagram of individual detector elements [deSo 90] outside light, the front face of the phoswich assembly is covered by an aluminized mylar foil (0.15 mg/cm^2 mylar and 0.02 mg/cm^2 aluminum).

Figure 2.6 is a photograph of the basic photomultiplier assembly used in all of the Miniball detectors. In this photograph the phoswich detector and the matching trapezoidal light guide have not yet been attached. The photomultiplier tube and the cylindrical light guide are surrounded by a cylindrical μ-metal shield -- not shown in the figure 2.6. A precision machined aluminum ring is glued to the μ-metal shield surrounding the photomultiplier and the cylindrical light guide. This ring also helps to align the detection with respect to a precision-machined aluminum can that houses the voltage divider. It is this can that defines the detector's alignment when it is bolted to the rings of the array support structure.

2.2.2 Miniwall

This Miniwall array is made of six rings of phoswich detectors constructed in a manner very similar to those of the Miniball. The Miniwall detectors were made with 3 cm thick CsI(Tl) scintillator crystals and 8 mg/cm^2 thick scintillator foils spun from Bicron BC-498X scintillator solution. It should be noted that like the Miniball, the boundaries of the polar angles between the rings were approximated by machining the flat surfaces on the CsI(Tl) crystals very close to the boundaries corresponding to the ideal surfaces of constant polar angle. The resulting polar angles and the solid angles for detectors in each ring of the Miniball/Miniwall array are given in Table 2.1.

2.2.3 Ion Chamber

The Ion Chamber telescopes used in the experiment at MSU were built by R.T. de Souza at Indiana University. These telescopes where designed to have a low threshold

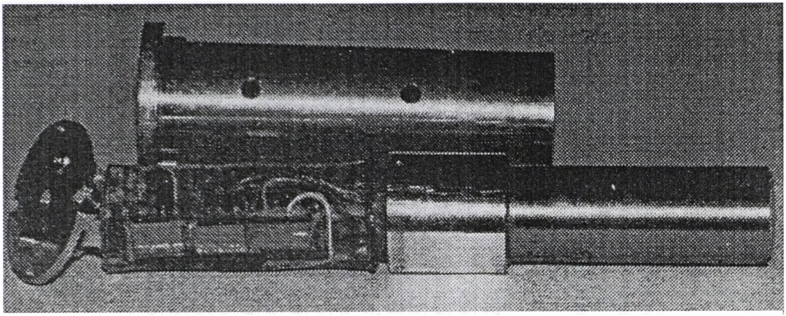

Figure 2.6 Photograph of the photomultiplier assembly. The scintillator and the first matching light guide are removed. The ring glued to the μ-metal shield defines the alignment of the can that houses the voltage divider; this can has been removed to expose the voltage divider.

Table 2.1 Information on the number of detectors in a ring, the solid angle of a detector in that ring, the polar angle of a ring, and the range in the polar angle and azimuthal angle that each detector covers. The letter W by the first six rings indicates that these are Miniwall rings.

Ring	Detector	ΔΩ(msr)	θ(°)	Δθ(°)	Δφ(°)
1(W)	16	1.11	4.375	2.15	22.50
2(W)	16	2.57	6.950	3.10	22.50
3(W)	22	2.59	10.000	3.00	16.36
4(W)	26	2.85	13.000	3.00	13.84
5(W)	24	5.56	16.625	4.25	15.00
6(W)	24	10.64	21.875	6.25	15.00
3'	28	11.02	28.000	6.00	12.86
4	24	22.90	35.500	9.00	15.00
5	24	30.80	45.000	10.00	15.00
6	20	64.80	57.500	15.00	18.00
7	20	74.00	72.500	15.00	18.00
8	18(-1)	113.30	90.000	20.00	20.00
9	14	135.10	110.000	20.00	25.70
10	12	128.30	130.000	20.00	30.00
11	8	125.70	150.000	20.00	45.00

energy and a high resolution. As shown in figure 2.7 the telescopes have three main active parts, an ion chamber, a silicon detector, and a CsI(Tl) Crystal scintillator. For more detailed information on the Ion Chamber telescopes see ref. [Fox 96].

The ion chamber is the first active component of the telescope, it has an electric field aligned along path of the ion, it is 55 mm long and uses seven square copper rings to shape its field. These rings are 2 mm thick with 4 mm of spacing between them with the central ring serving as the anode. The gas used in the ion chambers was CF_4 and was operated at pressures between 18 to 30 Torr.

The next active component in the telescope is a 500 µm thick silicon detector. The silicon detector was made by Micron Semiconductor and is a ion implanted, SiO_2 passivated silicon. Its active area is 30 mm by 30 mm, mounted on a 37 mm by 40 mm printed circuit board 1.28 mm thick.

The third component is a CsI(Tl) crystal, with a photodiode readout. These crystals are 30 mm thick and 37 mm square and were wrapped with Teflon tape and aluminized mylar to maximize the amount of light available for the photodiode. The photodiode used was a 2 cm by 2 cm Hamanatsu photodiode.

While the array can in principle be accurate calibrated, mistakes were made by the IUCF group in calibrating the ion chambers. These mistakes unfortunately reduced the utility of the ion chambers for this the experiment. For this reason, data from the ion chambers were not included in this dissertation.

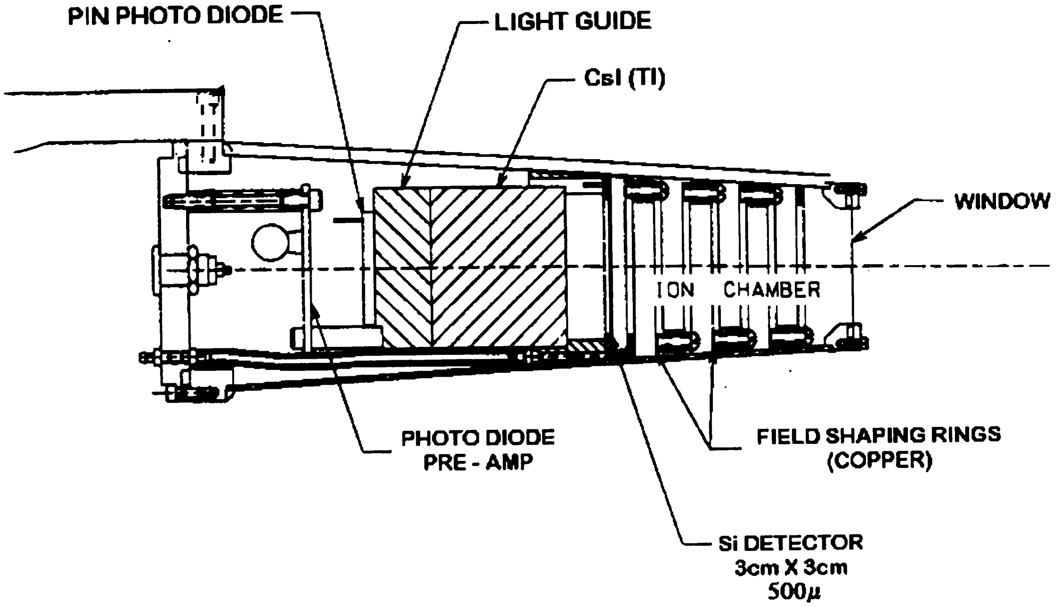
PIN PHOTO DIODE
LIGHT GUIDE
CsI (Tl)
WINDOW
ION CHAMBER
PHOTO DIODE
PRE - AMP
FIELD SHAPING RINGS
(COPPER)
Si DETECTOR
3cm X 3cm
500μ

Figure 2.7 A schematic diagram of the Ion Chamber Telescope

2.3 Target

Figure 2.8 is a drawing of the target insertion mechanism. The targets are mounted on frames made of flat shim stock 0.2 mm thick, which are attached to insertion rods with screws. These rods are mounted on a tray which can be moved parallel to the beam axis with the aid of small motor. An electromagnetic clutch is used to insert and retract the target rod when it is located in the appropriate position. A third drive rotates the target about the axis of the insertion rod. Being able to rotate the target can be helpful in determining the shadowing a detector experiences when it is located in the plane of the target frame.

2.4 Solid Angle Coverage of the Miniball/Miniwall Array

The original 11 ring configuration of the Miniball detection array is calculated to cover a solid angle corresponding to about 89% of 4π [deSo 90]. The 11 % loss in solid angle can be calculated in the following manner:

(i) beam entrance and exit holes (4% of 4π);

(ii) approximation of the curved surfaces corresponding to constant polar angle by planar surfaces (2% of 4π);

(iii) optical isolation of detectors and allowance for mechanical tolerances (4% of 4π);

(iv) removal of one detector to provide space for target insertion (1% of 4π).

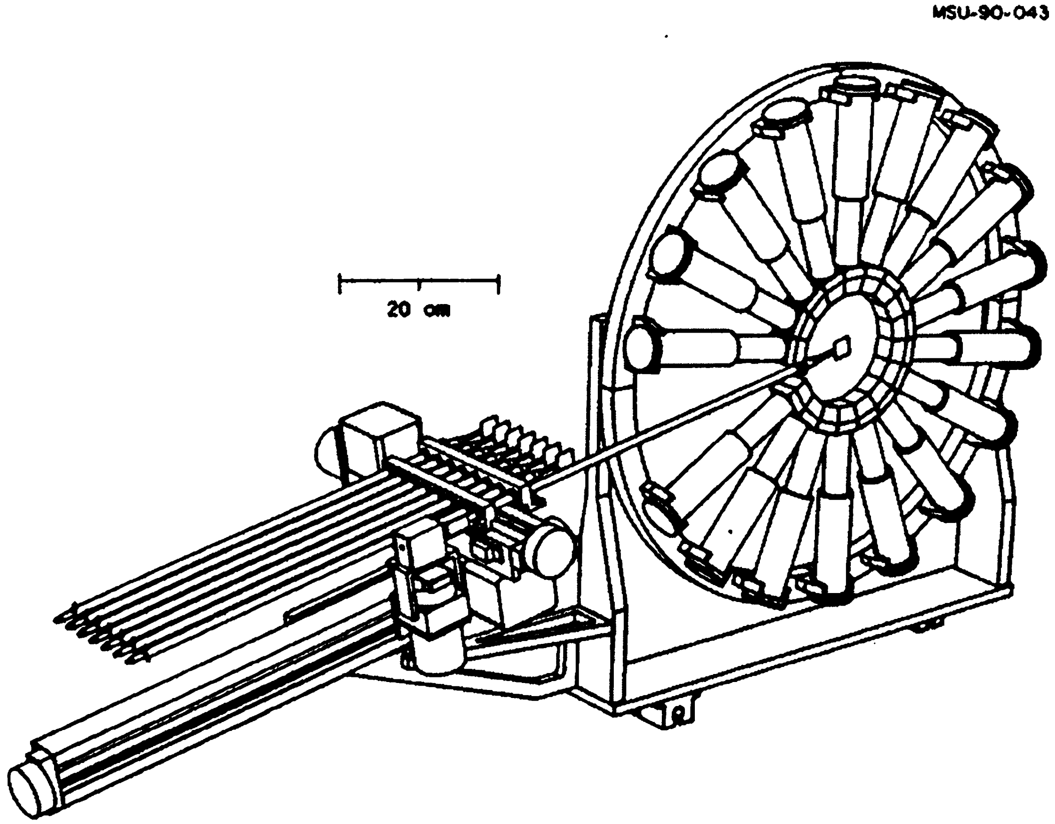
MSU-90-043
20 cm

Figure 2.8 Isometric view of the target insertion mechanism mounted on ring 8.

The Miniball was designed to handle the charged particle multiplicities produced in reactions like ^{40}Ar + ^{197}Au at E/A = 60 - 100 MeV [deSo 91, Kim 92, Phai 92]. Heavier projectiles have larger multiplicities, making the granularity of the Miniball insufficient to prevent double hits in some of the detectors of the Miniball array. To reduce this problem, original rings 1, 2, and 3 of the Miniball (with 12, 16, and 20 detectors covering $9° \leq \theta \leq 31°$) were replaced by rings 3, 4, 5, and 6 of the Miniwall array (with 22, 26, 24, and 24 detectors covering $8.5° \leq \theta \leq 25°$) constructed by Washington University, and a new Miniball ring 3' (with 28 detectors covering $25° \leq \theta \leq 31°$). This new forward array doubled the granularity of Miniball rings 1 - 3. Additional Miniwall rings 1 and 2 (with 16 and 16 detectors covering $5.4° \leq \theta \leq 8.5°$ and $3.225° \leq \theta \leq 5.4°$) were also constructed by Washington University to extend the coverage to even more forward angles. The configuration of the Miniball/Miniwall array contained 112 detectors in the Miniwall and 167 detectors in the Miniball in the experiment at Saturne. In the experiment at NSCL 128 Miniwall detectors and 167 Miniball detectors were used.

The new configuration of the Miniball/Miniwall array with its complete compliment of detectors is calculated to cover a solid angle corresponding to about 90% of 4π. The 10% loss in solid angles can be broken down in the following manner:

(i) beam entrance and exit holes (3% of 4π);

(ii) approximation of the curved surfaces corresponding to constant polar angle by planar surfaces (2% of 4π);

(iii) optical isolation of detectors and allowance for mechanical tolerances (4% of 4π);

(iv) removal of one detector to provide space for target insertion (1% of 4π).

At MSU when the Ion Chamber telescopes are added the coverage drops to about 87% of 4π. This is mostly because the telescopes are square and don't fit into the Miniball array as well as the detectors that they replace.

2.5 Electronic Readout of the Miniball/Miniwall Array

2.5.1 Photomultiplier Tube

The primary light produced by the plastic scintillator used in the phoswich detectors in this array has its maximum intensity at 370 nm. Now by adding a wavelength shifter to the solution the intensity maximum is shifted to 420 nm. However the scintillator foils are too thin for a fully effective wavelength shift, so the maximum emission remains in the far blue region of the spectrum. The CsI(Tl) crystals absorb this wavelength of light, this places a constraint on the maximum useful thickness of the CsI(Tl) crystals at about 3 cm. To minimize the absorption of light from the plastic scintillators by the light guides of the Miniball/Wall detectors, the light guides were made from UVT Plexiglas rather than ordinary Plexiglas.

The 10-stage Burle Industries model C83062E photomultiplier tube was chosen because its good timing characteristics (τ_R ~ 2.3 ns), large nominal gain (~10^7) [deSo 90], and linearity for fast signals. Each Miniball detector was soldered to its base to ensure a good electrical contact at all times. The Miniball was designed to operate in vacuum, therefore active bases (active divider chain) for the photomultiplier tubes were chosen to minimize the amount of heat generated by the detectors. A schematic of the active divider chain is given in figure 2.9. The final stages of the divider chain are of the

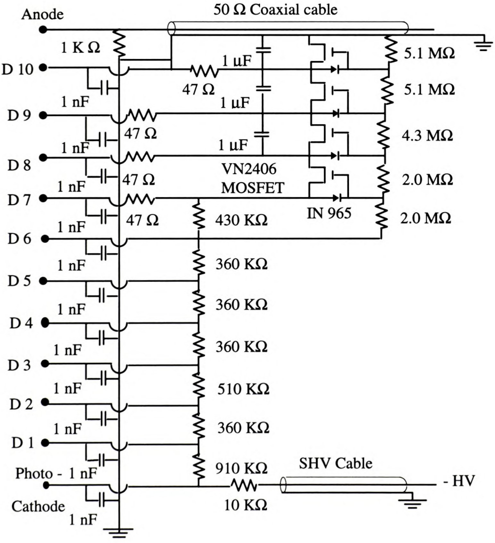
Anode
50 Ω Coaxial cable
1 K Ω
D 10
1 nF
D 9
1 nF
D 8
1 nF
D 7
1 nF
D 6
1 nF
D 5
1 nF
D 4
1 nF
D 3
1 nF
D 2
1 nF
D 1
Photo - 1 nF
Cathode
1 nF
47 Ω
47 Ω
47 Ω
47 Ω
1 uF
1 uF
1 uF
VN2406
MOSFET
IN 965
5.1 MΩ
5.1 MΩ
4.3 MΩ
2.0 MΩ
2.0 MΩ
430 KΩ
360 KΩ
360 KΩ
360 KΩ
510 KΩ
360 KΩ
910 KΩ
10 KΩ
SHV Cable
- HV

Figure 2.9 Schematic of the upgraded active voltage divider used for the Miniball detectors [Hsi 95].

"booster" type which helps improve the linearity of the high peak current generated b large signals from the fast scintillator. A μ-metal shield was placed around th photomultiplier and cylindrical light guide to protect the photomultiplier currents from stray magnetic fields. To prevent sparking when the detectors are running in a poo vacuum, the entire divider chain, including the leads to the photomultiplier tube, wa encapsulated in silicone rubber (Dow Chemical Sylgard 184), thus protecting the FET' from destruction.

2.5.2 Electronic Setup

Figure 2.10 shows a block diagram of the electronics used to gather the data fo the Miniball. The typical anode current signal from the photomultipliers is shown i figure 2.11. In the figure one can see that a fast signal from the plastic scintillator i superimposed on a signal from the CsI(Tl) crystal. The fast CsI(Tl) component of th signal is of the order of several hundred nanoseconds and the slow component of th signal is of the order of several microseconds, and the size of these components depen on the mass and charge of the detected particle. This analog signal is separated by passive splitter into several branches called the “fast”, “slow”, “tail”, and “trigger” wher the typical relative amplitudes $I_{fast}:I_{slow}:I_{tail}:I_{trig}$ are 0.82:0.04:0.04:0.1. The slow and tai branches of the splitter are directly connected to their respective fast encoding readou analog-to-digital converters (FERAs).

From figure 2.11 one can see that the gates for the “slow” and “tail” FERAs ar 390 ns and 1.5 μs wide. For the fast branch, a linear gate is inserted between the passiv splitter and the “fast” FERA. This linear gate allows each of the “fast” channels to b individually gated by the discriminator signal for that detector, something that cannot b

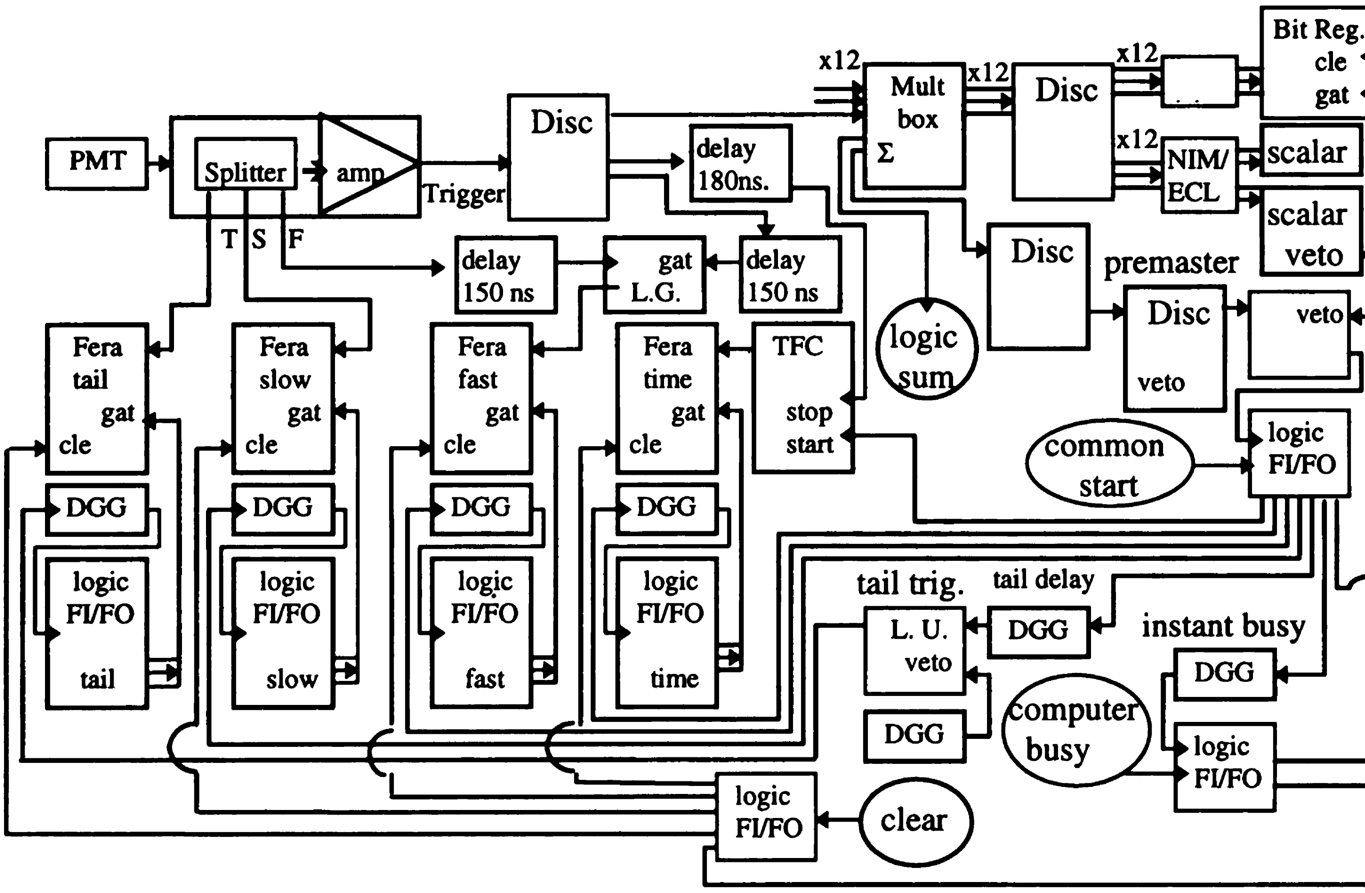
Bit Reg.
cle
gat
x12
Mult
box
Σ
x12
Disc
x12
. .
x12
NIM/
ECL
scalar
scalar
veto
PMT
Splitter
amp
Trigger
Disc
delay
180ns.
T
S
F
delay
150 ns
gat
L.G.
delay
150 ns
Disc
premaster
Disc
veto
veto
logic
sum
Fera
tail
gat
cle
Fera
slow
gat
cle
Fera
fast
gat
cle
Fera
time
gat
cle
TFC
stop
start
common
start
logic
FI/FO
DGG
DGG
DGG
DGG
logic
FI/FO
tail
logic
FI/FO
slow
logic
FI/FO
fast
logic
FI/FO
time
tail trig.
tail delay
L. U.
veto
DGG
instant busy
DGG
DGG
computer
busy
logic
FI/FO
logic
FI/FO
clear

Figure 2.10 Schematic electronics diagram of the electronics fc
Miniball array alone. The Disc, Split., DGG, Fera, Amp., L.U. and I
labels indicate the locations of discriminators, splitters, dela
generators, Fera ADC's, amplifiers, logical units and the fan in/fa
models respectively.

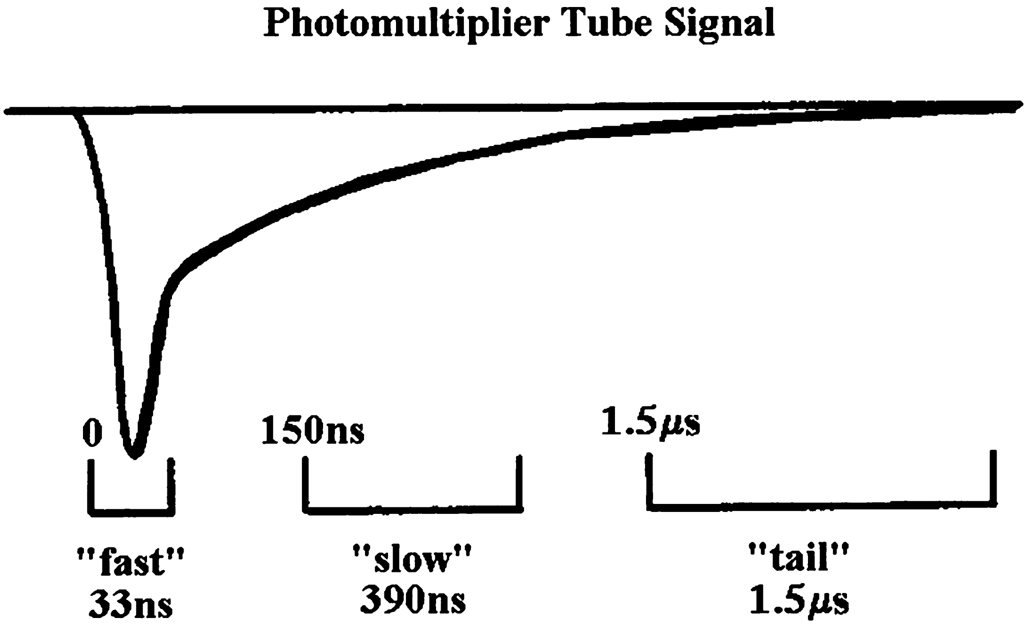
Photomultiplier Tube Signal
0
150ns
1.5μs
"fast"
33ns
"slow"
390ns
"tail"
1.5μs

Figure 2.11 This is schematic drawing of the analog signal of the phoswich detectors. The fast, slow, and tail gates of the Miniball are shown. The top numbers show when the gates open after the first gate has opened. The time intervals shown are the time durations for the gates.

done with the common gate FERAs. The linear gates are opened ≈ 20 ns prior to the leading edge of the linear signal and for a duration of 33 ns as shown in figure 2.11. Then the fast FERA gate is set to precede the gated fast signal and has a width of 150 ns. The trigger branch, I_{trig} is reamplified by a fast amplifier and fed into a leading edge discriminator module, the output of which provides the stop signal for the Time-to-FERA Converter (TFC) and opens the linear gate for the fast channel.

Each discriminator module has an output called the sum output, which is the linear sum of attenuated output signals for all of the 16 channels. The amplitude of the sum signal is $N \bullet 50$ mV where N is the number of channels with a signal greater then the discriminator level. The sum outputs of each discriminator are used as the inputs of the "Mult Box", which is another linear summer that generates an output that is proportional to the number of channels that are triggered in the event. By placing a discriminator level on the output of the "Mult Box" one gets a simple multiplicity trigger.

Since the size of the analog signal from the detectors is reduced as the signal travels through the cables, it is advantageous to place the data acquisition electronics as close to the detectors as possible. To accomplish this, it is necessary to place the electronics in the vault near the detectors and to control the discriminator thresholds and the photomultiplier gains remotely with the computer. Then the signals from each of the detectors can be checked remotely. This is done looking at the sum output of the linear gate modules while selectively masking the discriminator and linear gate outputs.

The electronic setup of the Miniwall was a little different than that of the Miniball see figure 2.12. The anode signal first passes through a fast amplifier and is then split into the fast, slow, and tail components. The fast signal is processed through a Philips

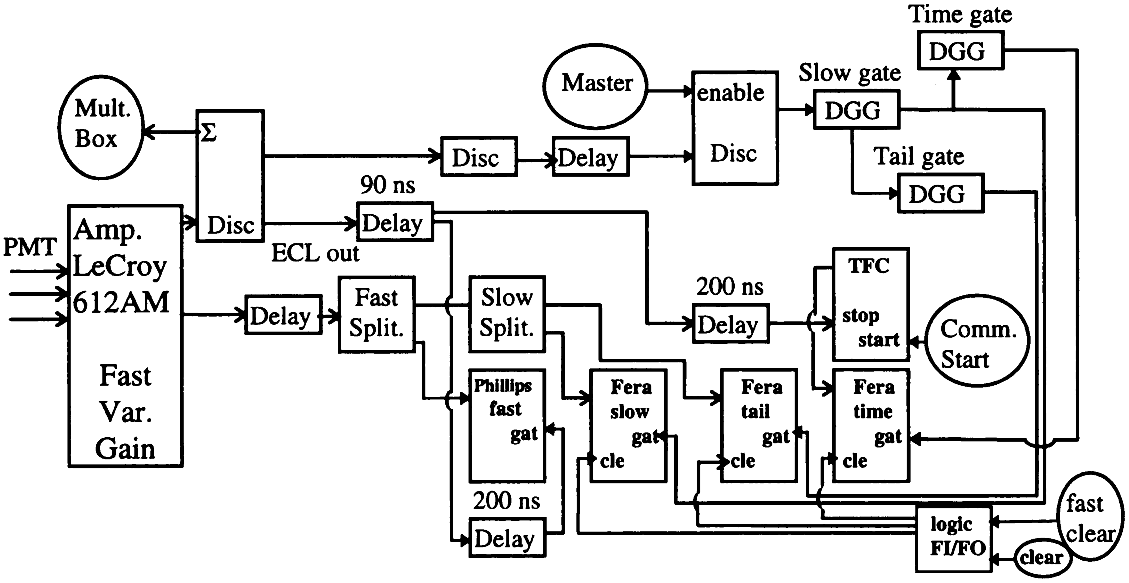
Time gate
DGG
Master
enable
Disc
Slow gate
DGG
Mult.
Box
Σ
Disc
Delay
Tail gate
DGG
90 ns
Delay
PMT
Amp.
LeCroy
612AM
Fast
Var.
Gain
Disc
ECL out
Delay
Fast
Split.
Slow
Split.
200 ns
Delay
TFC
stop
start
Comm.
Start
Phillips
fast
gat
Fera
slow
gat
cle
Fera
tail
gat
cle
Fera
time
gat
cle
200 ns
Delay
logic
FI/FO
fast
clear
clear

Figure 2.12 Schematic diagram of the data acquisition electronics for the Miniwall array alone.

(QDC). The slow and tail are still processed through FERA ADC's. The time signal is taken from the discriminator and passes through about 290 ns of delay before going to into a TFC and then is sent to a FERA.

Chapter 3

Data Analysis

The detectors in the Miniball/Miniwall array are plastic scintillator, CsI(Tl) phoswich devices. The response of these detectors is non-linear and can also present problems for precise particle identification. The methods for dealing with these difficulties are presented in this chapter. The chapter begins with a description of the particle identification procedure followed with a description of the energy calibrations.

3.1 Particle Identification

There are two basic types of spectra that are used to identify the particles; the choice of spectra depends on the particle to be identified. They are the Slow vs Tail and the Fast vs Slow spectra [deSo 90, Kim 91]. Figures 3.1 through 3.4 give examples of these two spectra for both the Miniball and the Miniwall. While both of these spectra are good for identifying particles, it turns out that by applying a few transformations to these spectra, particle identification becomes much easier. The PID spectrum (Particle Identification), and the PDT spectrum (for the Slow vs Tail spectrum), are used for particle identification in this thesis.

3.1.1 PID Spectrum

The PID spectra are constructed by performing a transformation on the Fast and Slow components of the signal. These are constructed so that particles of the same

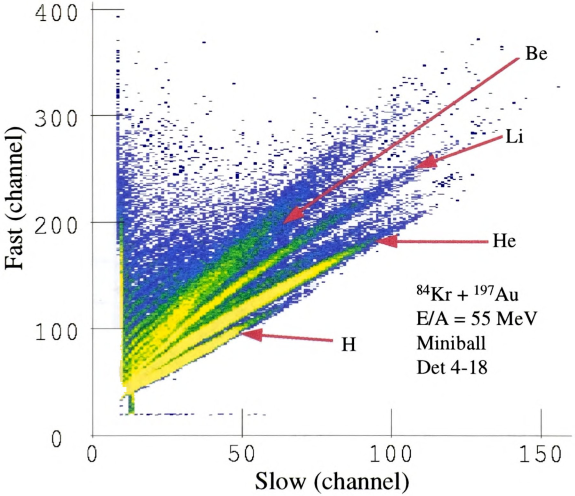

Figure 3.1 Fast versus Slow spectrum of detector 4-18 of the Miniball (ring 4 and position 18) from the ^{84}Kr + ^{197}Au collisions at E/A = 55 MeV.

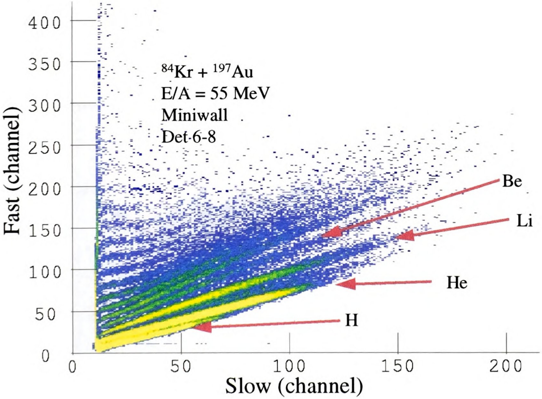

Figure 3.2 Fast versus Slow spectrum of detector 6-8 of the Miniwall (ring 6 and position 8) from the ^{84}Kr + ^{197}Au collisions at E/A = 55 MeV.

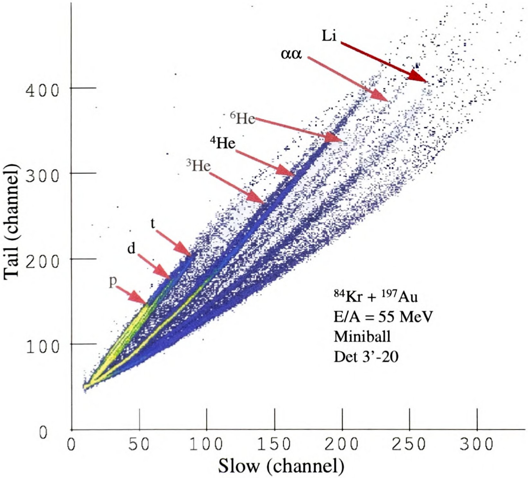

Figure 3.3 Tail versus Slow spectrum of detector 3'-20 of the Miniball (ring 3' and 20 position) from the ^{84}Kr + ^{197}Au collisions at E/A = 55 MeV.

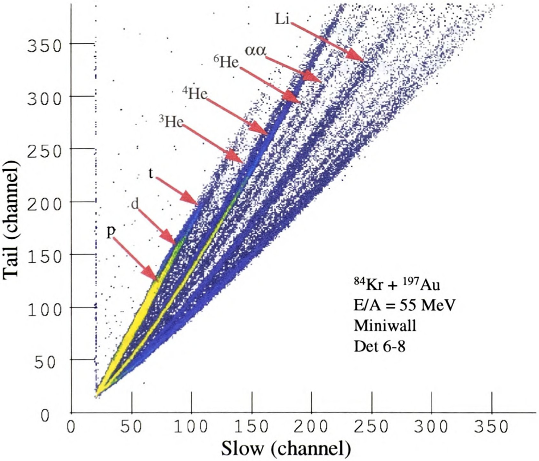

Figure 3.4 Tail versus Slow spectrum of detector 6-8 of the Miniwall (ring 6' and position 8) from the ^{84}Kr + ^{197}Au collisions at E/A = 55 MeV.

charge appear on the same horizontal line, see figures 3.5 and 3.6. This makes it easier to draw the charge gates, and to extrapolate gates to higher charge states that may be harder to see. The success of this procedure relies on the uniformity of the Miniball/Miniwall crystals, i.e. the crystals all have the same doping factor and thickness. This allows one to develop a transformation procedure for a detector and use it on the other detectors.

These transformations requires normalizing the Fast vs Slow spectra to a common reference spectrum. The normalization is done by matching the punch-through energies of the hydrogen and helium isotopes of the detectors to those of the reference detector. The punch through energies are defined as the minimum amount of energy a particle must have to completely pass through the crystal. Once the Fast vs Slow spectra are normalized to the reference spectrum, the transformation used to produce the PID spectrum for the reference spectrum is then used on the spectra for the other detectors to produce their PID spectra.

To construct the PID spectra the normal Fast vs Slow is changed so that the charge particle lines form horizontal lines and have equal separation between each of the lines. The first step in transforming the spectrum is to draw a line on the maxima of all the charge lines in the Fast vs Slow spectra of the reference spectrum. The Fast signals that lie on these charge lines are assigned values according to $Y = Z \bullet 20$, where Z is the charge of the fragment. A new two-dimensional plot is then constructed with this Y value and with an X value is equal to the Slow component. To transform the points between the charge lines the following equations are used:

$$X = \text{Slow} \tag{3.1}$$

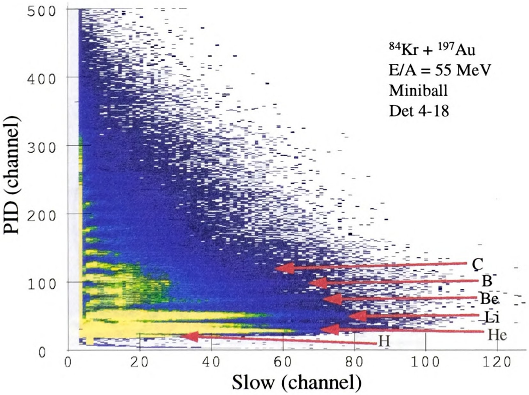

Figure 3.5 This is a plot of a Slow versus PID spectrum of detector 4-18 of the Miniball. Visible are the different charge lines making it easier to draw the gates for particle identification when analyzing the data.

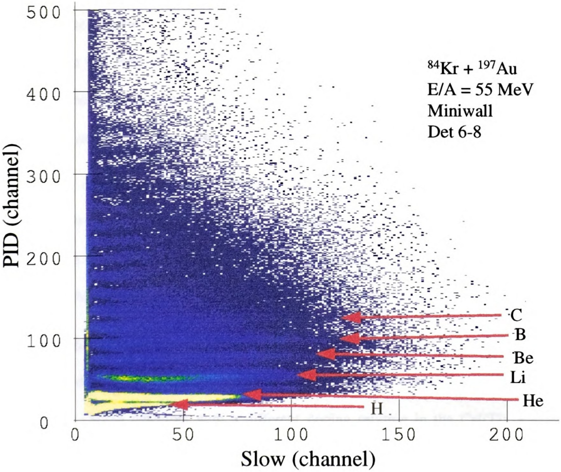

Figure 3.6 This is a plot of a Slow versus PID spectrum of detector 6-8 of the Miniwall. Visible are the different charge lines making it easier to draw the gates for particle identification when analyzing the data.

$$Y = 20 \cdot \left(Z_{\text{Lower}} + \frac{\text{Fast} - \text{Fast}_{\text{Lower}}}{\text{Fast}_{\text{Upper}} - \text{Fast}_{\text{Lower}}} \right). \tag{3.2}$$

Note, that Slow is the slow channel of the detected particle, Fast is the fast channel of the detected particle, Z_{Lower} is the charge of the charge line immediately below the fast value for the detected particle, $\text{Fast}_{\text{Lower}}$ is the fast channel of that Z_{Lower} charge line, and $\text{Fast}_{\text{Upper}}$ is the fast channel of the Z charge line right above the detected particle. All of the fast channels in this expression have the same slow channel associated with them. The X and Y are the new channels in the PID spectra.

Using this method the PID spectrum have nearly horizontal charge lines with carbon expected at $Y \approx 120$ for example. The gates for charge particle identification are then drawn on this new PID spectra. Identification of the charge of the detected particles was done by this method for both the Miniball and the Miniwall.

3.1.2 Problem Detectors

Gates drawn on PID spectra were used to identify the charged particles in most of the detectors. Some detectors with a different doping mixture in the CsI(Tl) crystals, displayed poor Fast vs Slow spectra, and this method of particle identification could not be used. Instead Fast vs Tail spectra were used to identify the charges. Figure 3.7 shows how the charge lines can be separated in these spectra.

3.1.3 PDT Spectrum

Figure 3.5 shows that while the PID spectrum is useful for identifying the charge it is not sufficient to separate hydrogen and helium isotopes. Therefore a different "PDT" spectrum is used to separate the isotopes. The PDT spectra are made from the Slow and

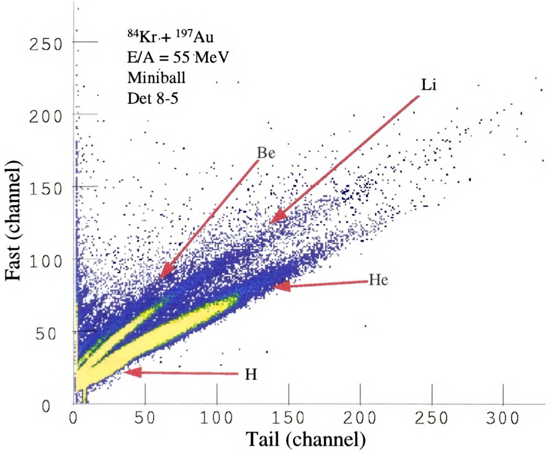

Figure 3.7 Tail versus Fast spectrum of detector 8-5 of the Miniball (ring 8 and position 5) from the ^{84}Kr + ^{197}Au collisions at E/A = 55 MeV.

Tail components of the detector signal by expanding the region where most of the data is located [Kim 91]. This is done by first drawing two gates lines which contain the detected data between them; figures 3.8 shows how these lines were drawn.

$$\mathrm{Tail}_1 = \mathrm{Line}_1(\mathrm{slow}) \tag{3.3}$$

$$\mathrm{Tail}_2 = \mathrm{Line}_2(\mathrm{slow}) \tag{3.4}$$

$$\Delta_{\mathrm{max}} = \mathrm{Tail}_1 - \mathrm{Tail}_2 \tag{3.5}$$

$$\Delta = \mathrm{Tail}_r - \mathrm{Tail}_2 \tag{3.6}$$

$$\mathrm{PDT} = 512 * (1 - \Delta/\Delta_{\mathrm{max}}) \tag{3.7}$$

Tail_1 and Tail_2 are functions that define the lines used in the transformation to obtain the PDT spectrum. The difference between two points at a given slow value is defined as Δ_{max}, and Δ is defined as the difference between Tail_2 and the Tail_r value of the data point. Multiplying the ratio of Δ to Δ_{max} by the number of displayable channels, 512, gives the quantity "PDT". The new PDT component becomes the x-coordinate and the Slow component becomes the y-coordinate of the PDT spectra. Figures 3.9 and 3.10 show the PDT spectra with all of the isotopes marked.

In the PDT spectra one can draw the gates for the hydrogen and helium isotopes fairly well up to the punch through energies. Particle identification beyond this point can be problematic and determining the energies of such particles is usually not possible.

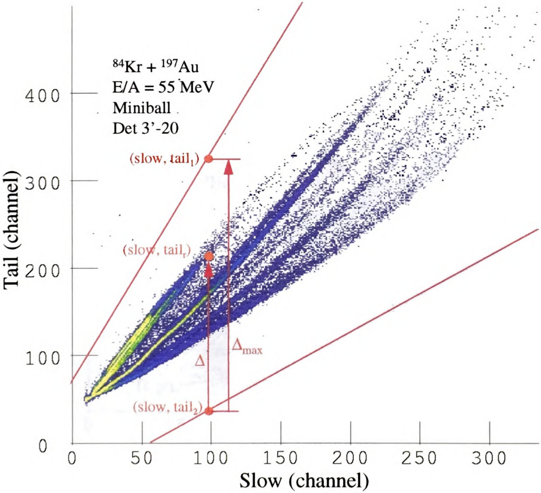

Figure 3.8 This is a plot of the Tail versus Slow and the variables that are used to make the PDT function. In the plot you can clearly see the relationships between Tail$_1$, Tail$_2$ and Tail$_r$.

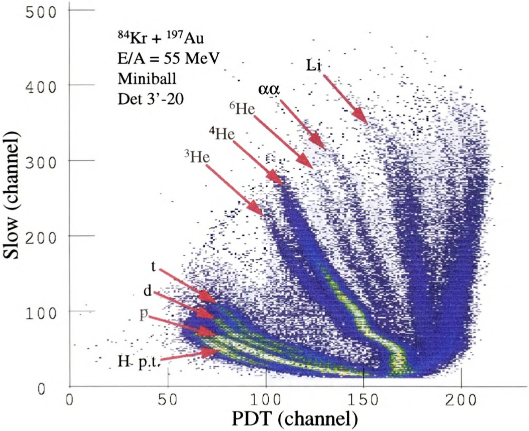

Figure 3.9 This is a plot of a PDT versus Slow spectrum of detector 3'-20 of the Miniball. Visible are the different Hydrogen isotopes, protons, deutrons, and tritons, as well as the Helium isotopes, ^{3}He and ^{4}He.

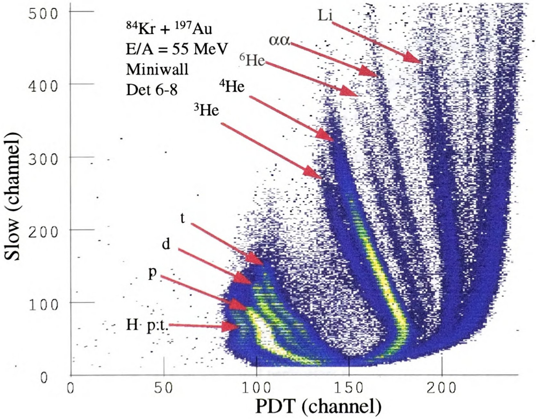

Figure 3.10 This is a plot of a PDT versus Slow spectrum of detector 6-8 of the Miniwall. Visible are the different Hydrogen isotopes, protons, deutrons, and tritons, as well as the Helium isotopes, ^{3}He and ^{4}He.

3.2 Energy Calibration

3.2.1 Light Output Equation

To find the energy of a detected particle one looks at the light output of the CsI(Tl) crystal. This light output is dependent on both the mass and the energy of the particle. This relationship was found by bombarding the CsI(Tl) crystals with different types of charged particles of known energies. The dependence of the light output can be written as a function that is dependent on Z, the charge of a particle, and E, the energy absorbed by the crystal from the particle [Stor 58, Quin 59, Alar 86, Gong 88, Souz 90, Kim 91, Colo 92]. The following is the light output equation used for the Miniball detectors [Kim 91, Schw 94]:

$$L(E,Z)=\alpha(z)E+\beta(Z)\,[e^{-\gamma(Z)E}-1] \tag{3.8}$$

E is the energy of the particle and Z is the charge of the particle. The parameters α, β, and γ are also functions of the charge of the particle. Equation 3.8 predicts a light output that is not linear, but the value of the actual parameters are such that once the energy goes above 10 MeV/A the dependence of L on E is nearly linear.

The three parameters used in equation 3.8 are all functions dependent on the charge of the particle. It has been proposed by Colonna et al. [Colo 92] to use the following method for defining these calibration functions.

$$\alpha(Z)=a_1+a_2e^{-a_3Z} \tag{3.9a}$$

$$\beta(Z)=b_1+b_2e^{-b_3Z} \tag{3.9b}$$

$$\gamma(Z)=c_1+c_2e^{-c_3Z} \tag{3.9c}$$

The new parameters a_i, b_i, and c_i are all constants that are fitted to the calibration data. Using this method, the light output from the light particles ($Z \leq 2$) can not be fitted that well, so different α, β, and γ constants are found for the light particle data.

Since the thickness of the CsI(Tl) crystals of the array are known, 2 cm for the Miniball and 3 cm for the Miniwall, the punch through points can also be used to help calibrate the detectors. Comparing the punch through energies with those generated from equation 3.8, it is found that the light output from the detector should be about 20 ± 5% greater than what was observed for the punch through of α-particles. This difference was determined to be caused by a saturation effect within the PM tube.

3.2.2 Saturation Effect

This saturation was observed at large signals and was found to be related to the gain of the photo tubes. The capacitors on the final dynodes of the tubes were not large enough to prevent reduction in the inter dynode voltages for these signals.

To evaluate the saturation effect, 10 different detectors were directly bombarded with low intensity beams of ^{6}Li, ^{12}C, and ^{18}O, with known energies ranging from E/A = 22 - 80 MeV. Since the electronic circuit transmitting the slow signal to the ADC has a passive current and a well defined attenuator, the QCD Channel, Ch#, of the slow signal is proportional to the signal from the photomultiplier tube. By comparing the observed photomultiplier signal with that predicted for the light output by equation 3.8 a fractional deviation is obtained. The fractional deviation can be defined by the following equation:

$$f(\mathrm{Ch\#}) = \frac{\mathrm{Ch\#}_{\mathrm{norm}} - \mathrm{Ch\#}_{L(E,Z)}}{\mathrm{Ch\#}_{L(E,Z)}} \qquad (3.10)$$

The fractional deviation, f(Ch#), is the fractional amount that the data lies below the calibration curve and is presumed to be a function of Ch#. $Ch\#_{norm}$ is the observed QDC channels normalized so that the proton punch through of the detector is in channel 240.37. This normalization takes advantage of the fact that proton signals are small and have little saturation. The value of $Ch\#_{L(E,Z)}$ is the channel calculated from equation 3.8 given all the known energies of the particles, where it has been normalized in the same way as the QDC channel. It was found that f(Ch#) depends on the pulse height from the photomultiplier tube.

The fractional deviation for ^{12}C data was found and is plotted in the upper panel of figure 3.11. The data shows that, for large QDC channels, the observed pulse height is less than what is expected from the light output calculated in equation 3.8. The ^{12}C data was then fitted with the straight line, shown in both panels of the figure. The lower panel of figure 3.11 shows that this line also describes the saturation effect for the ^{6}Li data. The fit of the ^{12}C data is also in agreement with the saturation effect observed for ^{4}He, ^{6}Li, ^{10}B, ^{12}C, ^{14}N, ^{16}O, and ^{20}Ne particles in previous experiments with the Miniball [Kim 91, Peas 94].

By fitting the data in figure 3.11 a linear relationship between the QDC channel and the fractional deviation is obtained;

$$f(Ch\#) = m_{fd} * Ch\#_{norm} \tag{3.11}$$

where m_{fd} is the slope of the line. When this relationship is combined with equation 3.10 the following equation is obtained:

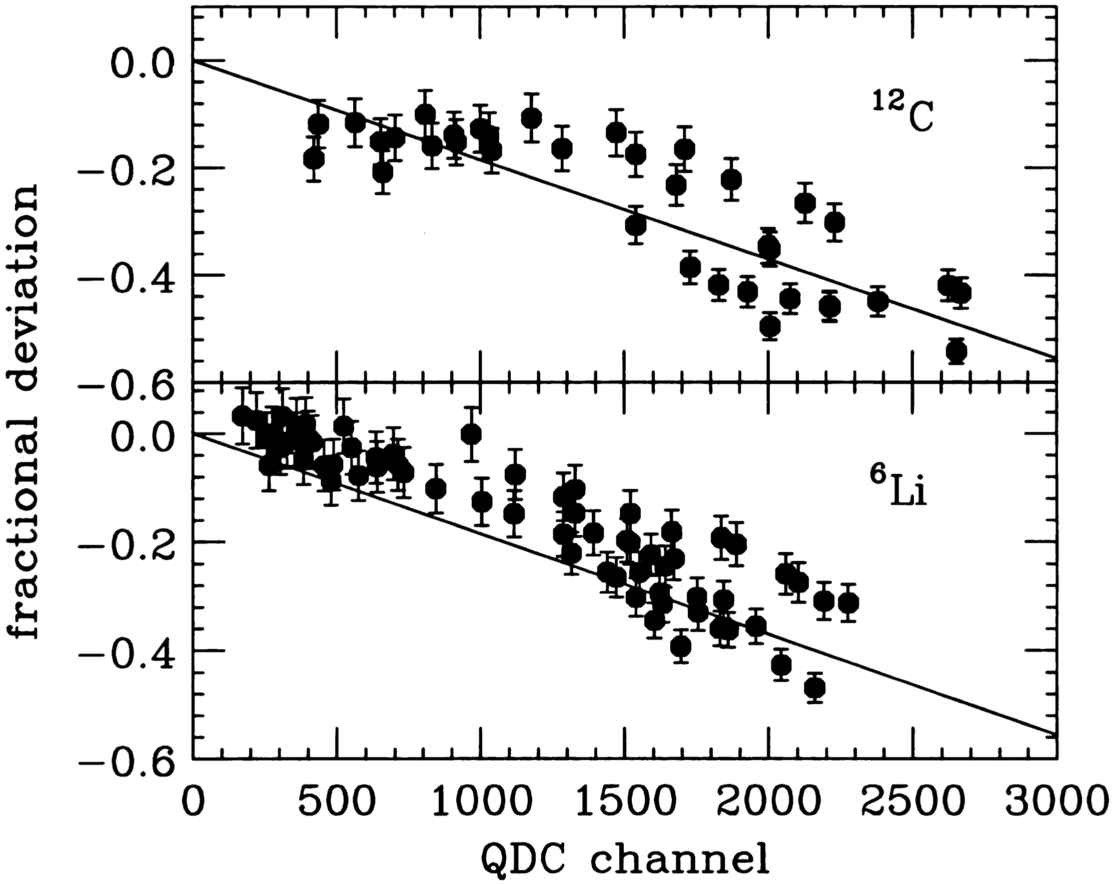

Figure 3.11 The upper panel shows the results obtain for the fractional deviation when using ^{12}C as the reference particle. The line is linear fit to the ^{12}C data and defines the function f(Ch#), the fractional deviations. The light output for the Miniball and Miniwall was less then the output predicted by equation 3.8. The lower panel shows how the result for f(Ch#) obtained from the ^{12}C data compares to the deviation observed for the ^{6}Li data.

$$\mathrm{Ch\#}_{L(E,Z)} = \frac{\mathrm{Ch\#}_{norm}}{1 + m_{fd} * \mathrm{Ch\#}_{norm}} \tag{3.12}$$

Equation 3.12 is used to find the QDC channel corresponding to the light output equation after the saturation effect is taken into account. This light output equation can then be inverted to find the energy. Figure 3.12 shows the corrected (closed points), and uncorrected (open points), calibration points for ^{4}He and ^{12}C. The graph shows how well the corrected data fits the energy calibration curve, obtained from equation 3.8, at the higher energies as opposed to the uncorrected data. The correction of the ^{12}C data at 250 MeV is about 10% and the correction for the He data at 300 MeV is about 30-40%.

The errors in finding the correct QDC channel with the fractional deviation can first be traced to the data points in figure 3.11. The fractional deviation values in figure 3.11 vary at fixed channel numbers by about 10-15%, which may reflect differences in the electronic components used to construct the PM tube. This fluctuation presumably could be removed by performing detailed calibrations of each detector. It is also expected that averaging over many detectors with the same polar angle will reduce the sensitivity to this systematic calibration uncertainty.

3.2.3 Determining the Parameters

There are now 13 different parameters to be fitted, including m_{fd}. These parameter are fitted by minimizing the χ^2 associated with the difference between the measured and calculated light output curves, using the constraint that none of the calibration lines cross each other. Using this method m_{fd} is found to be $-1.7\text{x}10^{-4}$ for

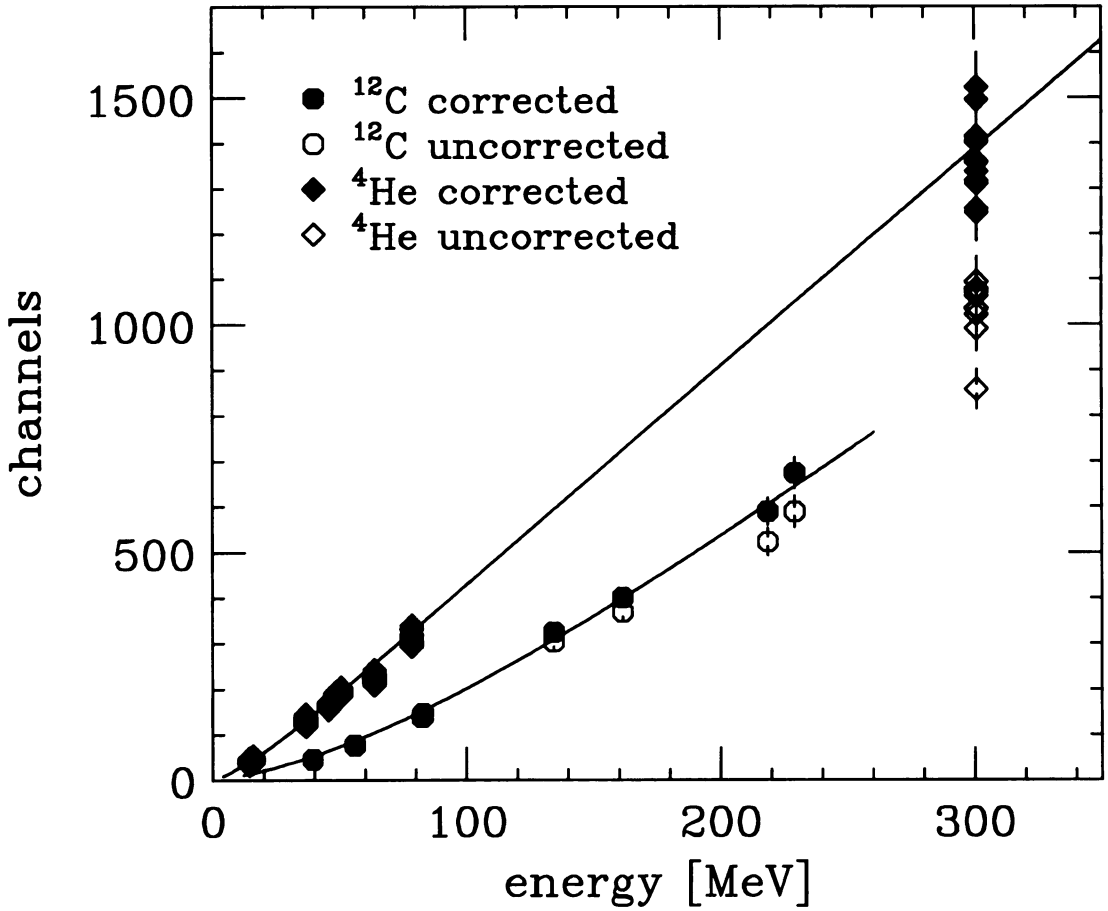

Figure 3.12 This is the calibration curve with the saturation correction for the ^{4}He and the ^{12}C particles. The top line is the ^{4}He energy calibration curve and the bottom line is the ^{12}C energy calibration curve using equation 3.8. The filled in symbols are the energy calibration data points using the saturation correction. The open symbols are the energy calibration data points without the saturation correction.

the Miniball and -1.860×10^{-4} for the Miniwall, and the values for a_i, b_i, and c_i listed in Table 3.1 are obtained for Z/A = 0.5.

Figure 3.13 shows the calibration curves and calibration data after all the corrections have been made and all the necessary constraints have been met. The insert in figure 3.13 shows how well the data fits at the lower energies. The ^{6}Li and ^{10}B points tend to fluctuate about their respective curves. This may reflect the fact that not all the calibration data were taken in the same experiment. For the energies larger than 30 MeV/A the calibrations are within 10-15% of the data points. At the lower energies the uncertainties are of the order 5-10% [Schw 94, Hsi 95].

Table 3.1 Values for the parameters a_i, b_i, and c_i for the functions $\alpha(Z)$, $\beta(Z)$ and $\gamma(Z)$ given in equation 3.9a, 3.9b, and 3.9c, where Z/A = 0.5.

$\chi^2/n = 3.27$	i = 1	i = 2	i = 3
a_i	0.4142	4.995	7.824E-2
b_i	229.7	5.039E-3	1.967E-4
c_i	1.339E-2	5.925E-3	3.846

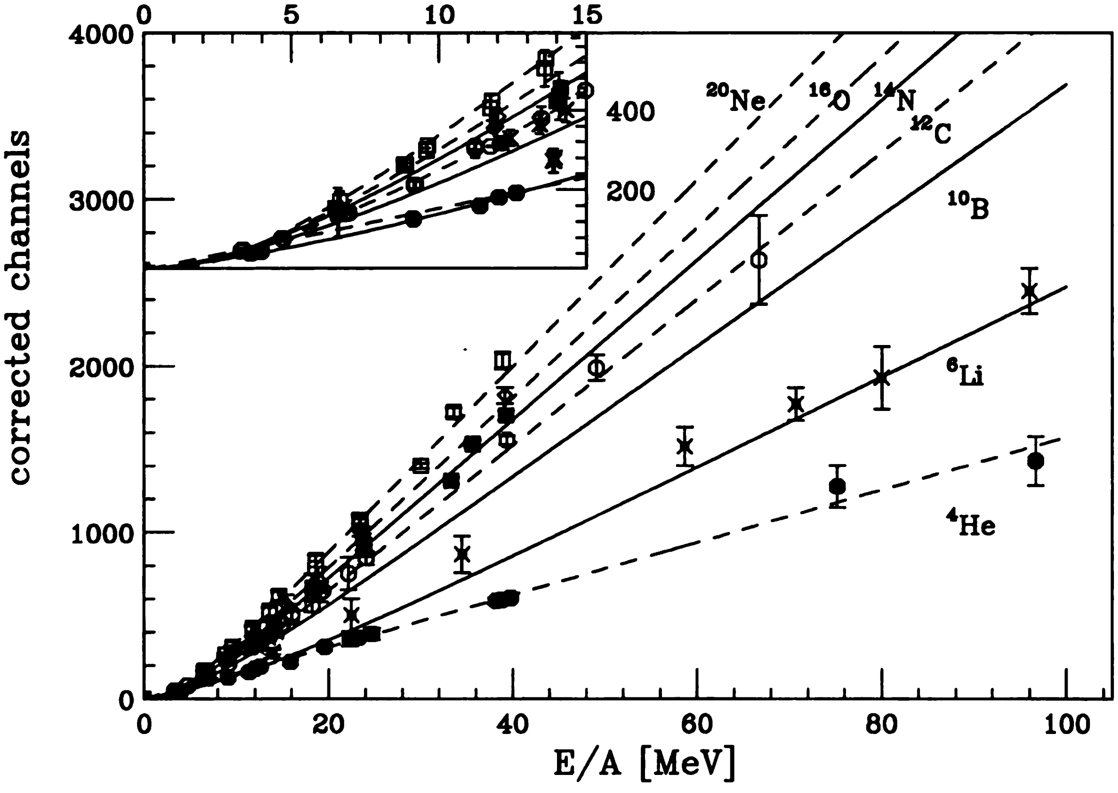

Figure 3.13 This plot shows the calibration curves for the detected particles with Z/A = 0.5. Also plotted are the calibration data for: ^{4}He, (solid circles), ^{6}Li, (open fancy crosses), ^{10}B, (crosses), ^{12}C, (open circles), ^{14}N, (solid squares), ^{16}O, (open diamonds), and ^{20}Ne, (open squares) particles.

Chapter 4

Data and Calculations

This chapter will discuss the results of the data analysis and compare them to various nuclear models. These models will be compared to the measured charge distributions, multiplicities and transverse energies at the various incident energies of the ^{84}Kr + ^{197}Au system. In these comparisons, both the data and the models must be gated on the impact parameter and have the same energy thresholds.

4.1 Impact Parameter

The impact parameter of a collision [Gold 80] can be obtained by looking at several variables that one can obtain from the data. Examples of such variables are the total charge particle multiplicity, N_C, the total proton participant multiplicity, N_p, or the total detected charge, Z_{tot}, since they are all sensitive to the impact parameter [Phai 92]. In this dissertation the charged particle multiplicity, N_C, is used to select the impact parameter.

4.1.1 Equation

To construct an impact parameter filter based on the charged particle multiplicity, we presume that the charged particle multiplicity decreases monotonically as the impact parameter increases. Under this relationship the following general geometrical equation can be used to assign the impact parameter for a specific event:

$$\hat{b}(N_C) = \frac{b(N_C)}{b_{\max}} = \left[\int_{N_C}^{\infty} P(X')dX'\right]^{1/2} / \left[\int_{N_C(b_{\max})}^{\infty} P(X')dX'\right]^{1/2}. \qquad (4.1)$$

Here P(X) ≡ P(N_C) is the experimental charged particle multiplicity distribution, N_C is the charged particle multiplicity, and $N_C(b_{\max}) = 4$ is the minimum bias charged particle multiplicity corresponding to $b_{\max}$. The "reduced" impact parameter, $\hat{b}$, is the ratio of the impact parameter for the particular event to the maximum impact parameter $b_{\max}$ corresponding to the minimum bias of N_C. According to this definition $\hat{b}$ ranges over the interval $0 \leq \hat{b} \leq 1$. At E/A = 200 MeV, $b_{\max}$ was determined to be 10 fm for $N_C(b_{\max}) = 4$ using direct beam counting, and should be roughly the same at the other energies.

The charged particle multiplicity, N_C, consists of all charge particles detected in the Miniball/Minimal array. This includes the unidentifiable particles, like heavy fragments that stop in the fast plastic and light particles that punch through the CsI(Tl). Multiple hits in a detector increment N_C by one, even when double hit events can be identified. Double α's hits in one detector are an example of a clear double hit that is that is counted as a single particle. Figure 4.1 shows the normalized probability distribution P(N_C) for the six incident energies. The reduced" impact parameter is indicated at the top of each panel in the figure. Figure 4.2 shows the relationship between N_C and $\hat{b}$ for the six energies.

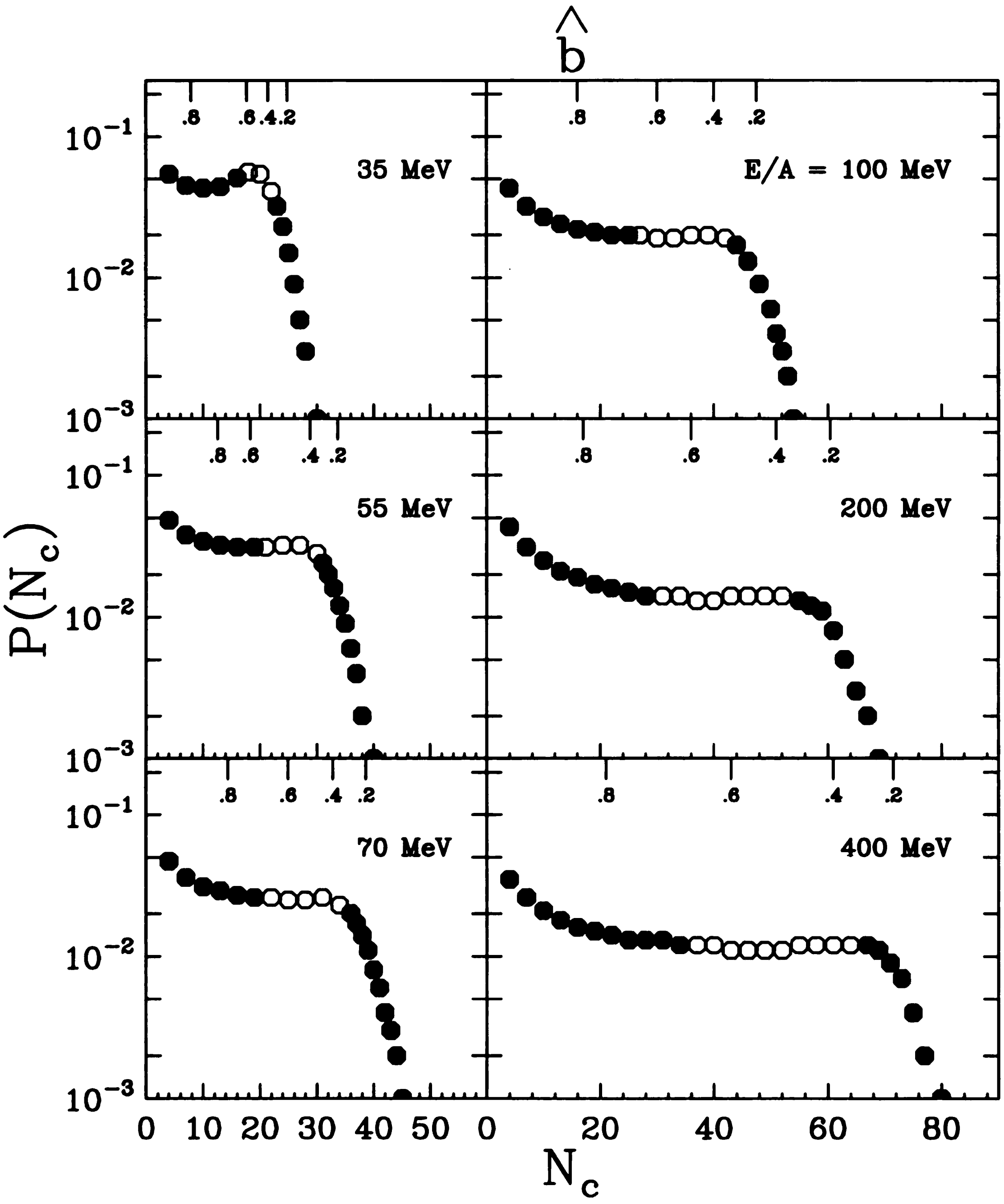

Figure 4.1 Normalized probability distributions for the charged particle multiplicity N_C for E/A = 35, 55, 70, 100, 200, and 400 MeV. The reduced impact parameter, $\hat{b}$, is shown at the top of the panels. The open circles indicate the middle impact parameters, $0.3 < \hat{b} < 0.66$.

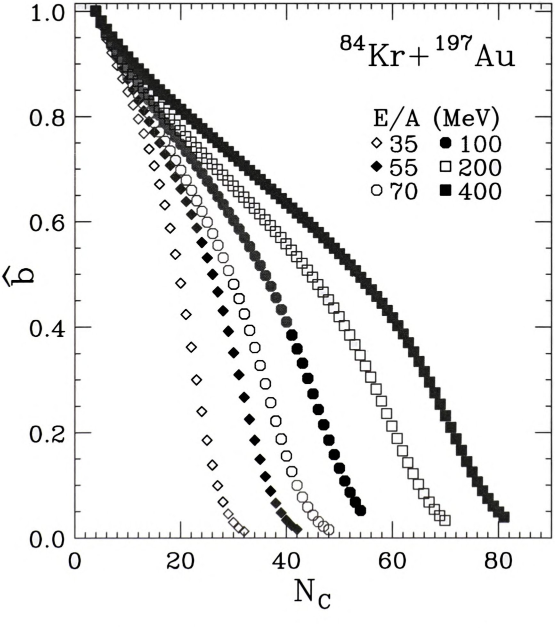

Figure 4.2 The dependence of reduced impact parameter, $\hat{b}$, upon the charged particle multiplicity, N_C, for E/A = 35, 55, 70, 100, 200, and 400 MeV.

4.1.2 Total Charge

If the Miniball/Miniwall was a perfect device, all the charged particles would be detected. Unfortunately, particles stop in the target or in the external foil of the Miniball/Miniwall detectors, or escape through the beam line hole in the forward array and are not detected. At larger impact parameters most of the charge remains in a projectile residue that passes down the beam tube, or it is in a target-like residue which stops in the target or the external foils of the detectors. Figure 4.3 show the relationship between the average total detected charge, $\langle Z_{tot} \rangle$, and N_C for the six incident energies. This figure shows that as N_C increases so does the efficiency of the array.

Since the relationship between N_C and $\hat{b}$ has been established for all six energies we can plot $\langle Z_{tot} \rangle$ vs. $\hat{b}$ and to look at the efficiency of the array in terms of $\hat{b}$. Figure 4.4 shows that as the $\hat{b}$ approaches zero (the largest value of N_C), the efficiency of the device improves for all of the incident energies. At the three highest incident energies and $\hat{b} \approx 0$, the ratio of the detected charge over the total charge approaches the geometrical efficiency (90%) of the experimental array.

4.2 Intermediate Mass Fragments

Using this impact parameter selection, examination of the properties of the Intermediate Mass Fragments, IMF's, charged particles with $3 \leq Z \leq 20$, begins. General phase space and barrier penetrability arguments [More 75, Frie 83, Lync 87, Gros 90, Sobo 83] lead to the prediction that the fragment emission probabilities should exhibit a strong initial rise as a function of temperature. However, at very high temperatures, the

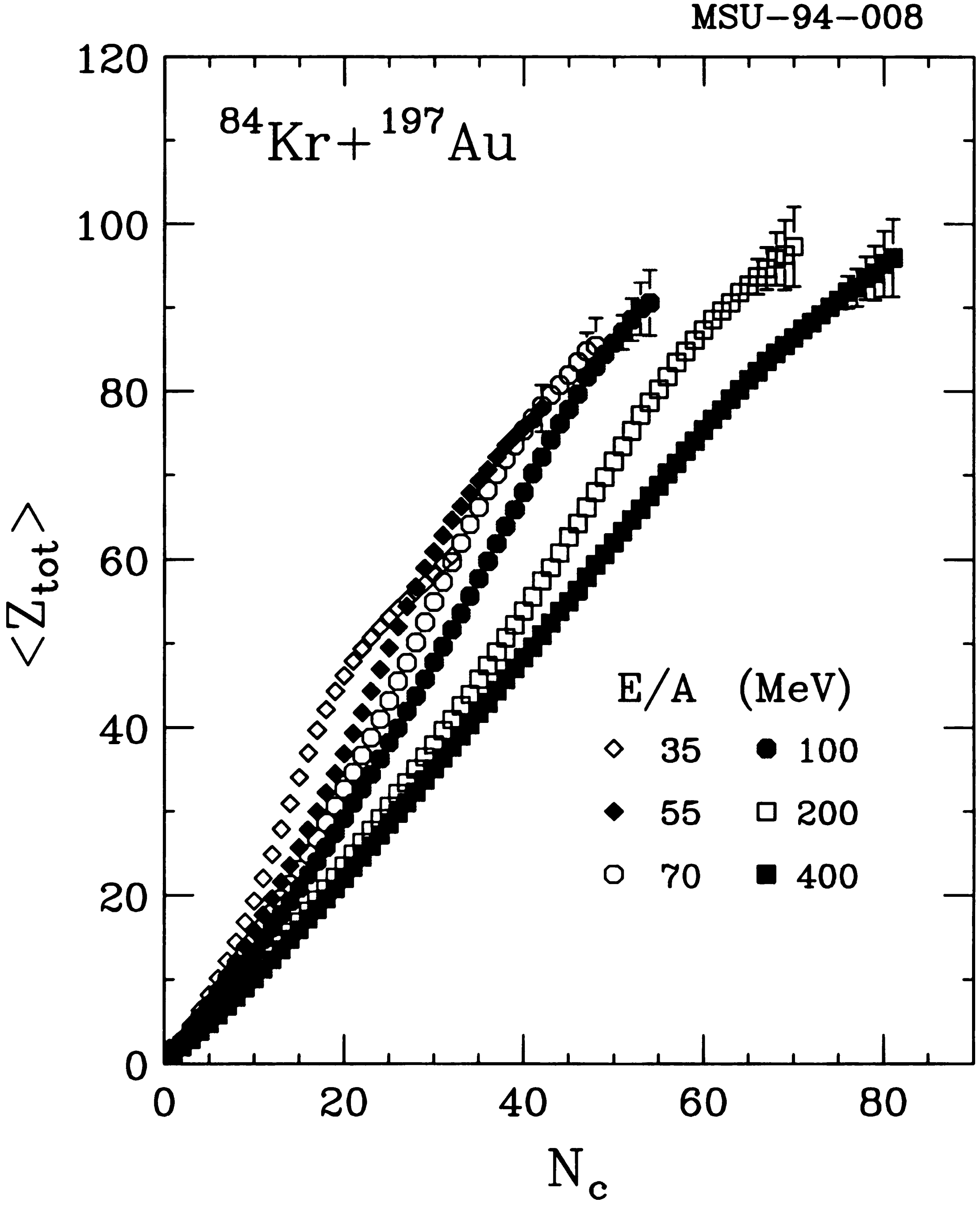

Figure 4.3 The dependence of the total charge, <Z_{tot}>, on the total charged particle multiplicity for E/A = 35, 55, 70, 100, 200, and 400 MeV.

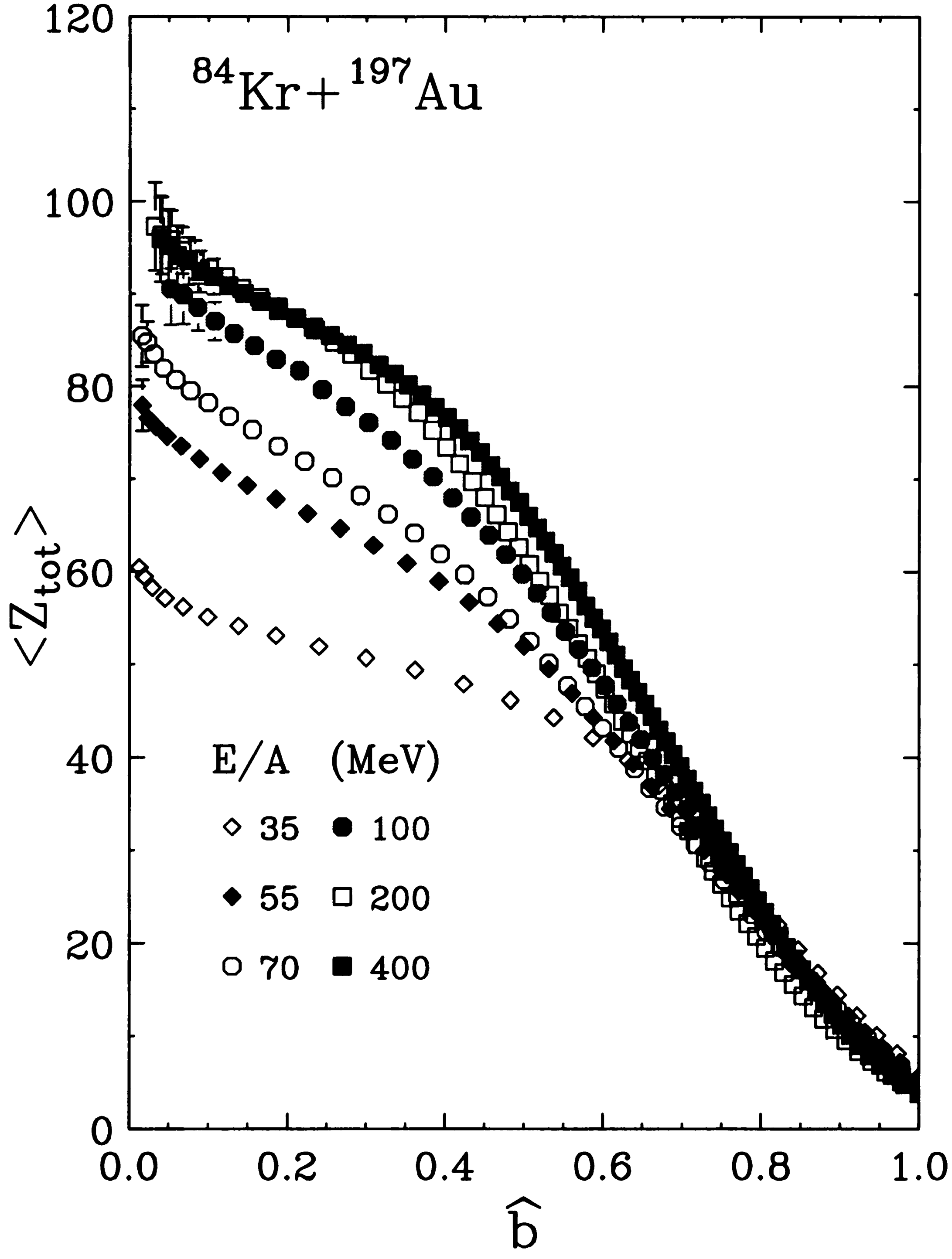

Figure 4.4 The dependence of the total charge, $<Z_{tot}>$, upon the reduced impact parameter, $\hat{b}$, for E/A = 35, 55, 70, 100, 200, and 400 MeV.

entropy of the system becomes so high that fragment production is suppressed. These two conditions together cause the fragment multiplicities to exhibit a maximum at some intermediate temperature, which may depend on the total charge of the fragmenting system.

The dependence of the fragment multiplicity on impact parameter was measured for projectile fragmentation of Au nuclei at E/A = 600 MeV. These measurements two showed the fragment multiplicity to increase with decreasing impact parameter to a maximum multiplicity, and then it decreases as the impact parameter is reduced further. This suggest that there is an excitation energy where fragment multiplicity reveals a maximum, and that the multiplicity decreases at higher excitation energy, as the system begins to vaporize [Ogil 91, Hube 91]. Looking at central collision of ^{36}Ar + ^{197}Au for incident energies of E/A = 35 - 110 MeV, the IMF multiplicity was found to increase with the incident energies [deSo 91], but a maximum in the fragment multiplicity with excitation energy was not observed. A decrease in the IMF multiplicity as the incident energy increases [Tsan 93, Wien 93, Kuhn 93] was observed for central Au + Au collisions at incident energies of E/A = 100 - 400 MeV; but the domain at lower energies where the fragment multiplicities increase with incident energy was not observed. One was lacking measurements of both the rise and the decline of multifragmentation at fixed impact parameter for a single system, so that the incident energy corresponding to the location of the maximum in the fragment multiplicity could be determined. Here such measurements are presented.

4.2.1 Experimental Data

Figure 4.5 shows the observed mean IMF multiplicity, $<N_{IMF}>$, as a function of detected charged particle multiplicity, N_C and figure 4.6 shows $<N_{IMF}>$ as a function of $\hat{b}$. For E/A = 35 - 100 MeV, the dependence of $<N_{IMF}>$ upon N_C follows a common trend roughly independent of incident energy: a similar effect was observed for ^{36}Ar + ^{197}Au collisions at incident energies ranging over E/A = 35 - 110 MeV [deSo 91]. Some fragments from the statistical decay of projectile-like residues, are lost because they are emitted to angles smaller than 5.4°. This loss is most important at the two highest incident energies, and leads to an unknown reduction in the fragment multiplicities at the medium to low values of N_C. This problem has little effect on the data for central collisions characterized by large values of N_C. At E/A = 35 - 200 MeV, the peak IMF multiplicity is observed at the most central collision characterized by the largest values of N_C. But at E/A = 400 MeV, the maximum $<N_{IMF}>$ occurs at $N_C = 60$ corresponding to $\hat{b} \approx 0.4$, and $<N_{IMF}>$ decreases for more central collision. This decline in $<N_{IMF}>$ is not a consequence of charge conservation or due to a loss in detection efficiency in the experimental setup, since the observed values of $<Z_{tot}>$ (shown in figure 4.3) increase with N_C and approach yields consistent with the geometrical efficiency.

The lower panel in figure 4.7 shows the relationship between the incident energy and $<N_{IMF}>$ for central collisions with $\hat{b} < 0.25$. For E/A<100 MeV, the increase of $<N_{IMF}>$ is likely due to increases in the thermal excitation energy and in the collective expansion velocity. Both drive the system towards densities less than $0.4\rho_o$ where

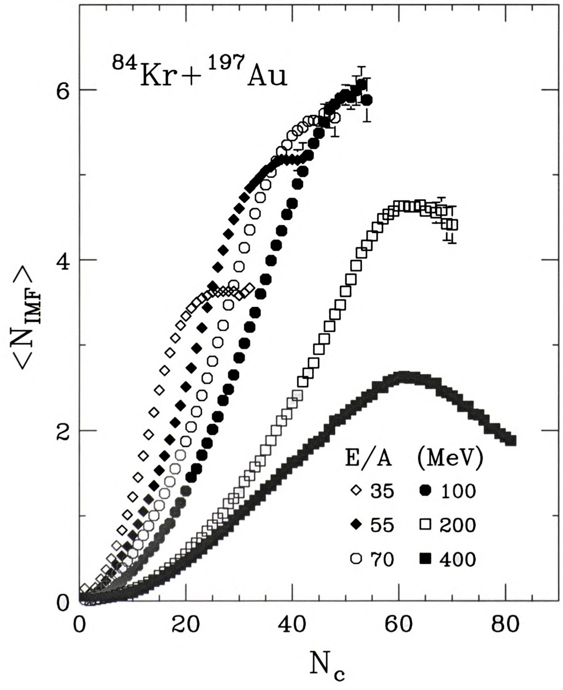

Figure 4.5 The dependence of the mean intermediate mass fragment multiplicity, $\langle N_{IMF} \rangle$, upon the charged particle multiplicity for E/A = 35, 55, 70, 100, 200, and 400 MeV.

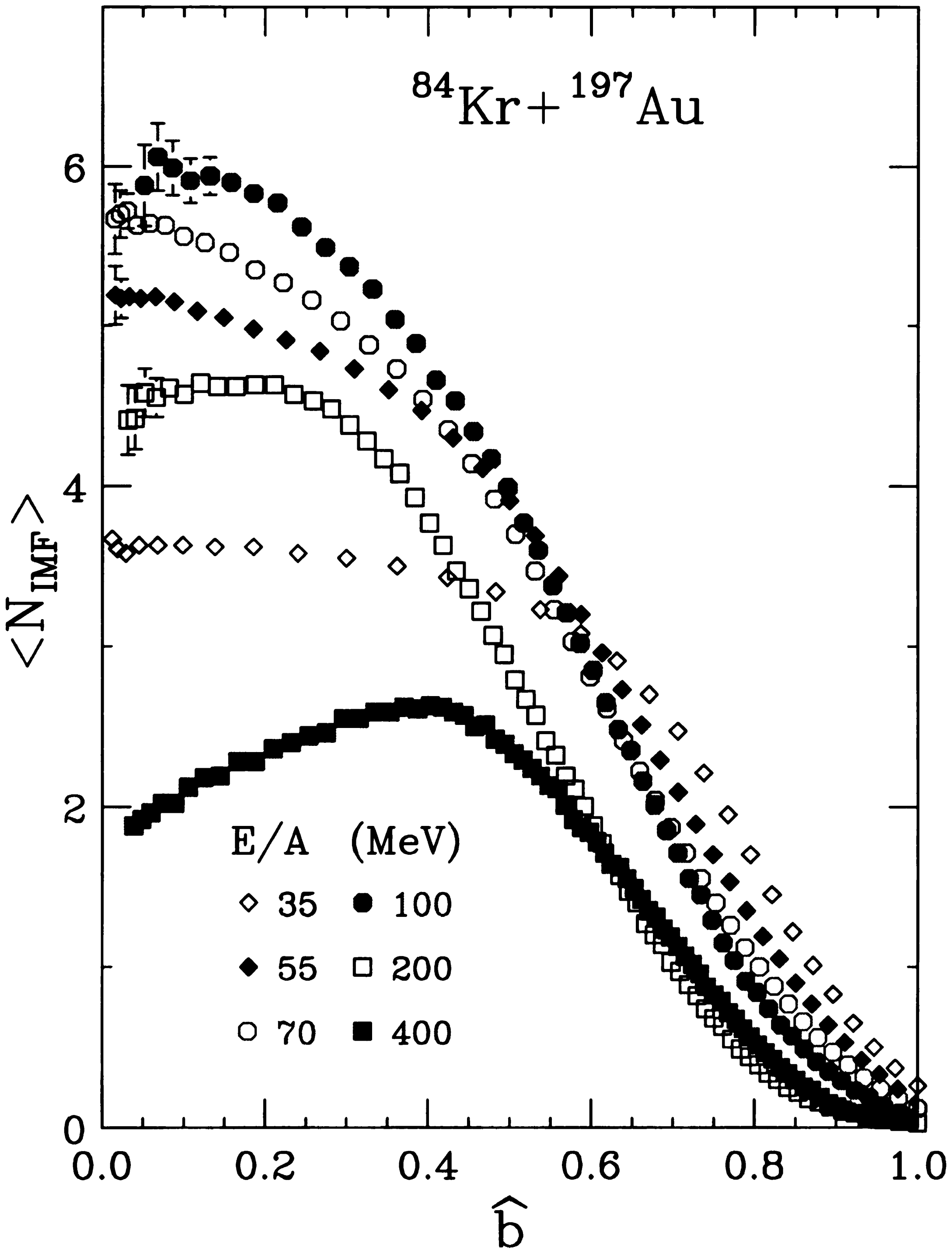

Figure 4.6 The dependence of the mean intermediate fragment multiplicity, <N_{IMF}>, upon the reduced impact parameter, $\hat{b}$, for E/A = 35, 55, 70, 100, 200, and 400 MeV.

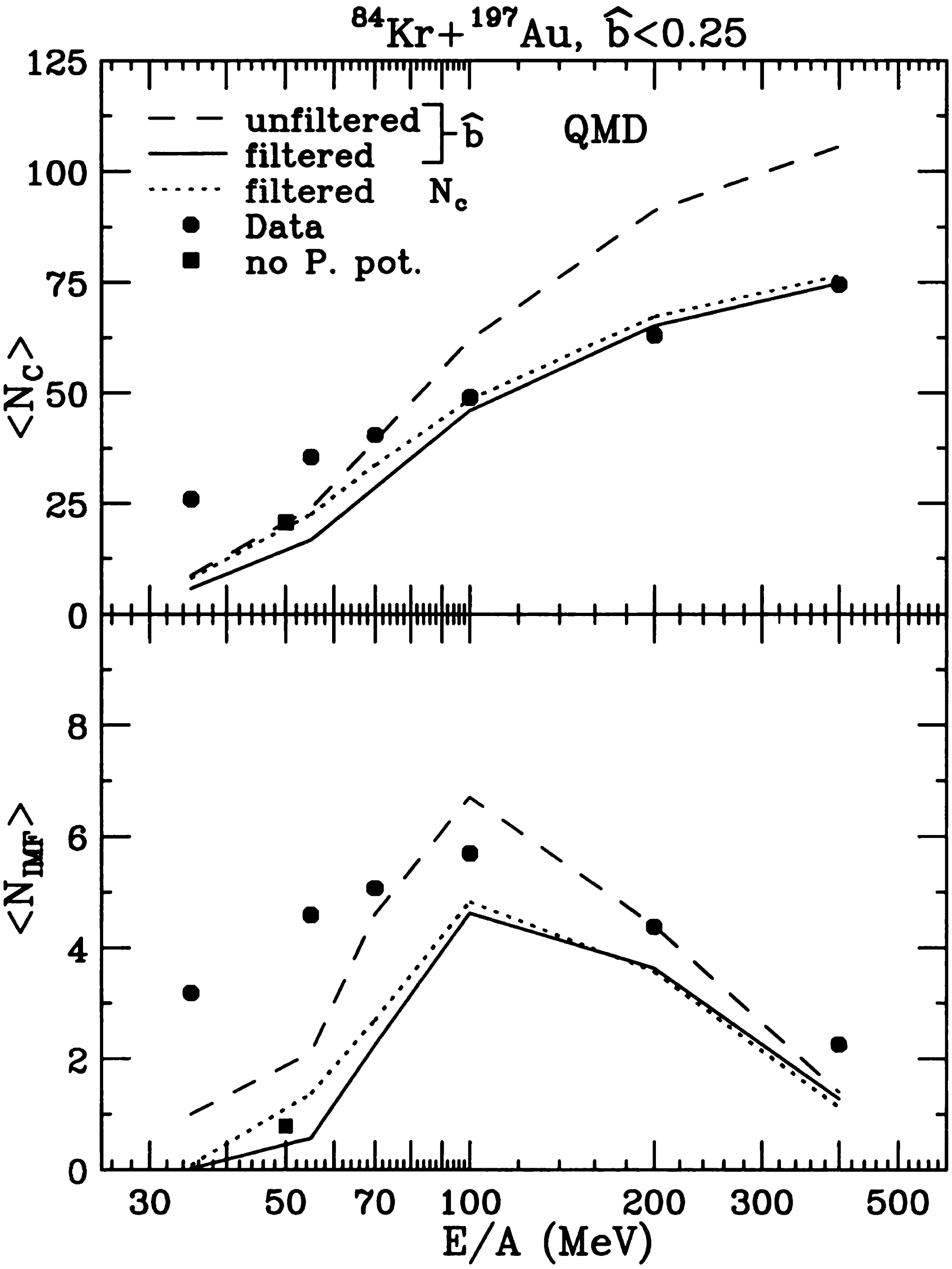

Figure 4.7 The upper panel shows a comparison between the measured mean charge particle multiplicity, <N_C>, and QMD calculations for central collisions as a function of incident energy. The lower panel shows the corresponding values for the mean IMF multiplicity, <N_{IMF}>. The solid dots are the experimental data points. The corresponding statistical uncertainties are smaller than the data points. The dashed lines are from unfiltered QMD calculations. The solid and dotted lines are QMD calculations filtered by the experimental acceptence. The solid square is the prediction of QMD calculations without the Pauli potential.

fragment production is enhanced [Frie 90, Bowm 92, Bond 95, Gros 90] and generally increases with temperature for $0 < T < 10$ MeV [Frie 90, Bond 95, Gros 90]. For E/A > 100 MeV, the decrease of the multiplicities with incident energy very likely reflects the suppression of fragment production at high temperature, $T > 10$ MeV and higher entropy [Tsan 93, Bond 95, Gros 90]. (Note that bound fragments comprise a small portion of the total phase space at excitation energies that significantly exceed the total binding energy of the system.) In this domain, collective expansion can also suppress fragment emission because the spatial variation in the collective velocity field makes for a small overlap with the wave functions of bound fragments [Kund 95]. Figure 4.7 is consistent with these expected trends and provides the first approximate determination of the energy at which the decrease in fragment production commences.

4.2.2 QMD Calculations

A similar maximum at E/A = 100 MeV was predicted by microscopic molecular dynamics models [Peil 89] for Nb + Nb collisions. It is therefore interesting to see whether such models can describe the present data. The lower panel of figure 4.7 also contains the result of QMD model calculations for central ^{84}Kr + ^{197}Au collisions for $\langle N_{IMF} \rangle$ versus the incident energy and the upper panel of figure 4.7 contains the result for $\langle N_C \rangle$ verses the incident energy. The dashed lines in the figure are the unfiltered results from the QMD model including the Pauli potential as described in refs. [Peil 91, Peil 92] and Chapter 1, where $b_{max} = 10$ fm is presumed. The solid lines show the filtered QMD calculations after correcting for the experimental acceptance. Some of the general energy dependent trends of the data are reproduced with the calculation, i.e. a maximum in $<N_{IMF}>$ at E/A = 100 MeV and monotonically increasing values for $<N_C>$. However, the calculations greatly underestimate the values of N_C and N_{IMF} when E/A < 100 MeV.

4.2.3 QMD+SMM Calculations

The failure of QMD calculations to reproduce the large IMF multiplicities observed at low incident energies has been attributed to an inadequate treatment of the decay of highly excited heavy reaction residues produced in the QMD calculations. As shown in refs. [Peil 92, Sang 92], the description of the statistical decay of a thermally excited nucleus is not adequate with the present QMD model. The exact cause of this deficiency of the QMD model is not clear, but could be attributed to the classical heat capacities of the computation QMD nuclei that result in low residue temperatures that are physically unreasonable. To correct for this deficiency, the decays of all fragments with $A \geq 4$ were calculated via the SMM [Bond 85, Botv 87]. The input excitation energies and masses for the SMM calculations were taken from the QMD calculations; after an elapsed reaction time of 200 fm/c. The basic parameters of the source, its mass, excitation energy, and the resulting yields, do not vary drastically with the reaction time [Peil 93]. Typical excitation energies of 5 - 8 MeV/A, were determined by subtracting the ground state energy of each fragment from the total energy in the fragment in the rest frame. For details about the determination of the ground state energies, see refs. [Peil 91, Peil 92].

The results of these two stage calculations, QMD + SMM, are shown by in figure 4.8. The lower panel of this figure shows that the calculations over predict the $<N_{IMF}>$

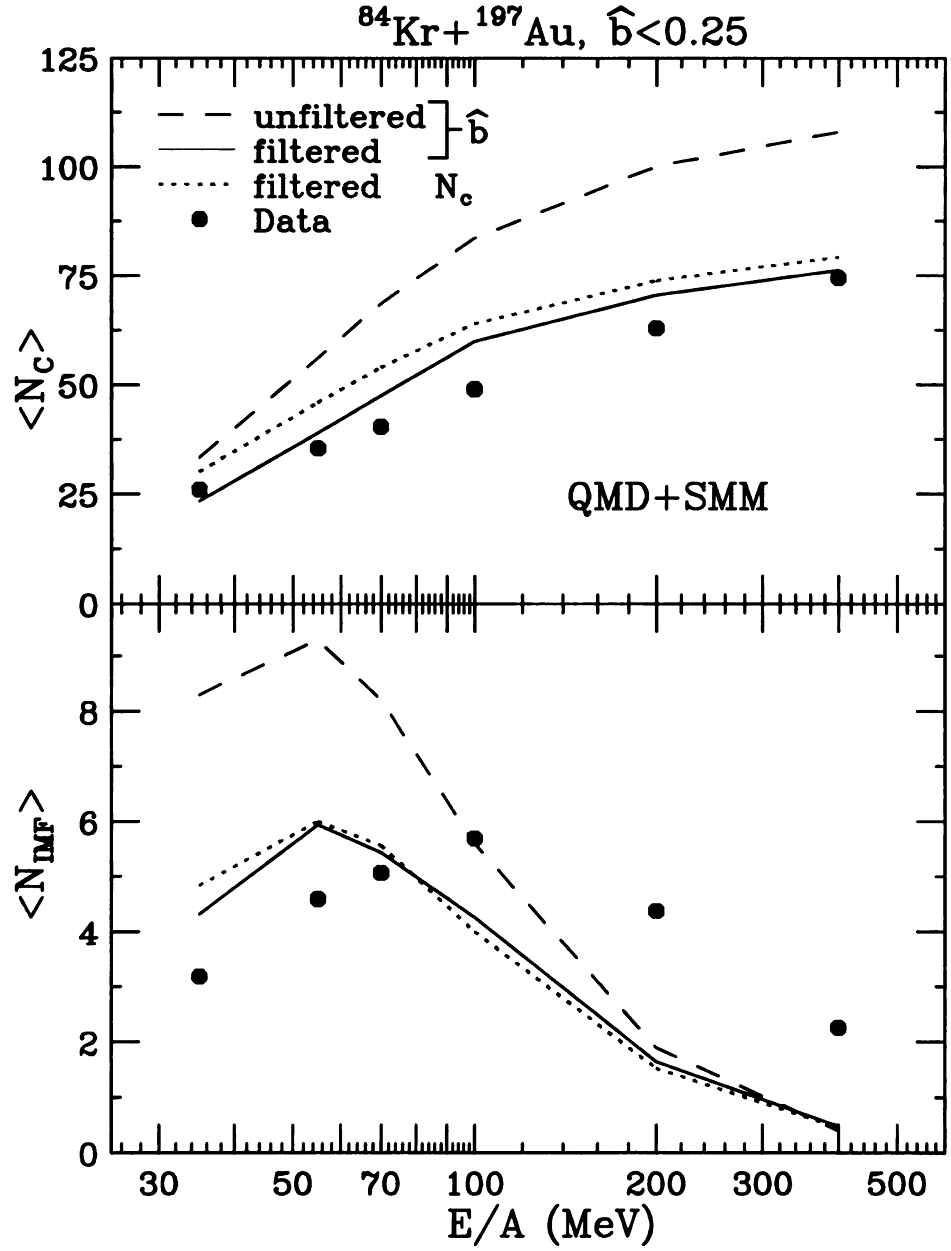

Figure 4.8 The upper panel shows a comparison between the measured mean charge particle multiplicity, <N_C>, and QMD+SMM calculations for central collisions as a function of incident energy. The lower panel shows the corresponding values for the mean IMF multiplicity, <N_{IMF}>. The solid dots are the experimental data points. The corresponding statistical uncertainties are smaller than the data points. The dashed lines are from unfiltered QMD+SMM calculations. The solid and dotted lines are from QMD+SMM calculations filtered by the experimental acceptance.

for E/A < 100 MeV/A; this additional yield comes from the contributions from the decay of the heavy residue in SMM stage. These calculations also under predict the $<N_{IMF}>$ at higher energies because many fragments produced by the QMD stage are evaporated away in the SMM stage. When these calculation are filtered through the experimental acceptance (solid lines), the values for $<N_{IMF}>$ are very close to the data at E/A < 100 MeV. Note, that the IMF detection efficiency is significantly reduced when E/A < 100 MeV, reflecting the fact that the QMD+SMM calculations are peaked at the low kinetic energies. This leaves the measured spectra and many of the predicted fragments below the experimental thresholds.

The upper panel of figure 4.8 shows a comparison between the $<N_C>$ values for the filtered and unfiltered QMD+SMM calculations and the data. In general, the filtered charged particle multiplicities follow qualitatively the experimental trends. Yet there is a tendency for the calculations to overpredict the production of charged particles at the higher energies; most of the extra yield is in the form of light particles.

In the previous comparisons, the impact parameters for the data were determined using equation 4.1, while the impact parameters for the calculations were among the input parameters to the calculations. To check whether the discrepancies between the calculations and data are caused by the impact parameter filter, calculations were performed in which the QMD and QMD+SMM calculations were impact parameter selected as if they were experimental data. The dotted lines in both figure 4.7 and figure 4.8 are calculations in which the impact parameter was defined by the calculated N_C

values. The latter calculations are essentially the same as the calculations previously shown for a fixed theoretical impact parameter.

4.2.4 SMM Calculations

It is interesting to investigate whether the discrepancies between the measurements and the QMD+SMM calculations reflect a fundamental limitation of the SMM model or whether a satisfactory agreement might be obtained with input parameters that are chosen independently of the predictions of the QMD model. To explore this issue, SMM calculations were performed, varying the excitation energy, density, and collective flow of the fragmenting system. Collective flow was calculated in the limits of a purely rotational flow and a self-similar radial flow. The collective velocity fields for the rotational $(\vec{\mathbf{v}}_{rot})$ and radial $(\vec{\mathbf{v}}_{rad})$ flow were given by $\vec{\mathbf{v}}_{rot} = \vec{\omega} \otimes \vec{\mathbf{r}}$ and the $\vec{\mathbf{v}}_{rad} = \beta_{\exp} \frac{\vec{\mathbf{r}}}{R}$, respectively, where ω is the angular velocity and $\beta_{\exp}$ is the radial expansion velocity. Since two-fragment correlation provide evidence that the limit of a single freezeout time is not attained [Corn 95], only a fraction f_A of the system containing a fraction f_E of the total excitation energy per nucleon is presumed to be equilibrated. The remaining excitation energy and mass of the system is presumed to be contained in a preequilibrium source that is too hot to emit fragments [Bond 95]. The parameters f_A, f_E, and rotational or radial flow were adjusted to reproduce the fragment multiplicities, charge distributions, and transverse energies, respectively. The resulting parameter values are given in table 4.1.

Figure 4.9 compares the SMM calculations for $\langle N_{IMF} \rangle$ to the data. Unfiltered and filtered rotational flow calculations are depicted by dot-dashed and solid lines,

Table 4.1 Parameters of SMM calculations chosen so that calculations will match the experimental data.

E_{Beam}/A (MeV)	Set	f_A	f_E	$<E_{rot}/A>$ (MeV)	$<E_r/A>$ (MeV)
35	1	0.650	0.890	1.2	0.0
35	2	0.650	0.850	0.0	0.9
55	1	0.650	0.760	2.5	0.0
55	2	0.595	0.710	0.0	1.9
70	1	0.625	0.740	4.0	0.0
70	2	0.563	0.670	0.0	3.0
100	1	0.568	0.760	8.0	0.0
100	2	0.509	0.665	0.0	6.0
200	1	0.420	0.585	15.0	0.0
200	2	0.378	0.490	0.0	11.0
400	1	0.248	0.440	25.0	0.0
400	2	0.207	0.360	0.0	19.0

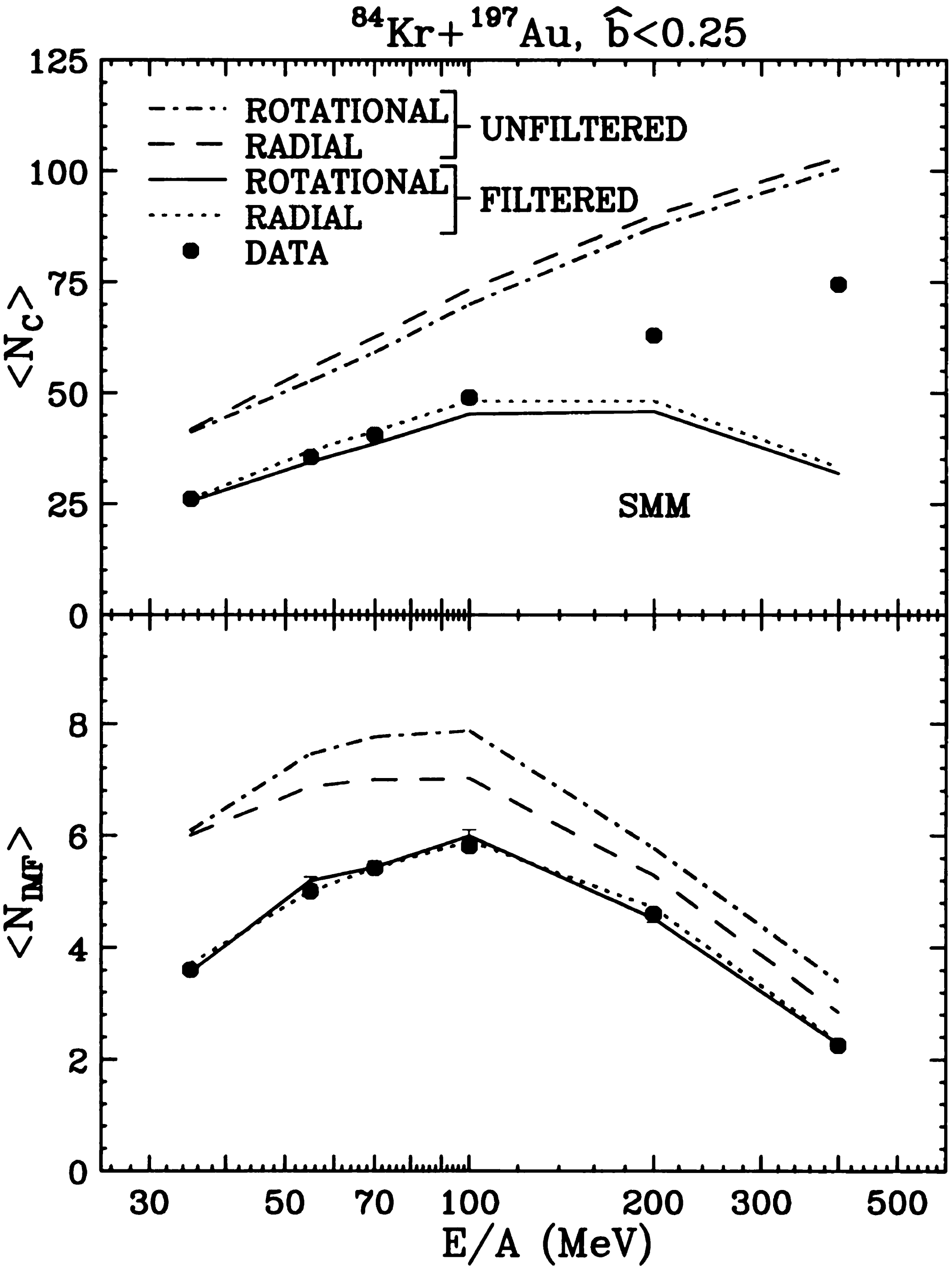

Figure 4.9 The upper panel shows a comparison between the measured mean charge particle multiplicity, $<N_C>$, and SMM calculations for central collisions as a function of incident energy. The lower panel shows the corresponding values for the mean IMF multiplicity, $<N_{IMF}>$. The solid dots are the experimental data points. The corresponding statistical uncertainties are smaller than the data points. The dashed and dot-dashed lines describe unfiltered SMM calculations which include radial and rotational flow, respectively. The dotted and solid lines are the corresponding filtered SMM calculations.

respectively. Unfiltered and filtered radial flow calculations are depicted by dashed and dotted lines, respectively. The conclusions are basically the same for radial flow as for rotational flow. The $<N_{IMF}>$ values for the unfiltered calculations exceed the experimental data. When corrections for the experimental acceptance are made, the filtered calculations essentially reproduce the experimental fragment multiplicities.

4.3 Charge Distributions

One of the earliest foci of the experimental investigations of fragmentation and multifragmentation was the excitation energy dependence of the fragment charge distributions. In many investigations the charge distributions were fitted by power law distributions $Y(Z) \sim A^{-\tau}$. Such fits were motivated by arguments based upon the Fisher liquid drop model phenomenology [Finn 92]. In calculations from these models, fragments were presumed to be associated with clustering near the critical point of the liquid-gas diagram, where relationships between thermodynamic parameters are largely governed by a set of critical exponents [Fish 67, Wils 71]. In this picture, the exponent τ is derived from the power law fit of the charge distribution, and is expected to be largest for reaction trajectories that pass through the critical point or critical region.

There are many issues that complicate this simple picture. One such issue is that the Coulomb potential energy does not scale linearly with the volume; long range Coulomb interactions complicate the extrapolation of increasingly heavy laboratory systems towards the thermodynamic limit characteristic of critical phenomena [Fish 67, Wils 71]. Aspects of such Coulomb effects are manifested by classical molecular dynamics calculations of highly charged systems. Such calculations predict a monotonic evolution of the fragment charge distributions from flat charge distributions at low excitation energies, with $\tau \approx 1$, to steeply falling distributions at high excitation energies [Pan 95, Kund 96]. Such a trend is inconsistent with the presumptions of critical exponent analyses [Lato 95, Camp 88, Gilk 94, Mahi 88, Li 93] which presume a minimum value of τ will be observed at intermediate excitation energies where reaction trajectories pass through a "critical region". Local chemical equilibrium may also not be achieved during the collision [Prat 95]. A loss of chemical equilibrium will alter relationships between the observed fragment distributions and those characteristic of an equilibrated system at the same temperature and density [Prat 95]. Where local equilibrium is attained, experimental observables can differ from the equilibrium values because post-breakup secondary decays of excited fragments [Fiel 87] change the fragment charge distributions from those of an equilibrated system at breakup. All the above effects were presumed to be negligible in previous analyses [Gilk 94, Mahi 88, Li 93].

Extremely flat charge distribution have been observed in central Au + Au collisions at E/A = 35 MeV [D'Ago 95]. While this observation offers support for the predictions [Pan 95, Kund 96] for highly charged systems to have a monotonic decreasing slope of the fragment charge distributions with increasing incident energy, an experimental demonstration of such an energy dependence was not provided until this dissertation.

4.3.1 Experimental Data

The charge distributions for the central collision, $\hat{b} < 0.25$, of the six incident energies are shown in figure 4.10. These distributions decrease monotonically with fragment charge and can be described by a power law of the form $Y(Z) = C \bullet Z^{-\tau}$. Fits using this functional form, shown by the solid lines, are very close to the experimental yields.

In figure 4.11 the extracted values of τ are shown as the solid points. The observed trend of monotonically increasing values of τ is consistent with classical molecular dynamics calculations for highly charged systems [Pan 95, Kund 96]. This trend is contrary to the presumptions in critical exponent analyses of minimum τ values at intermediate energies. The lowest value obtained for τ ($\tau = 1.4$ at E/A=35 MeV) is somewhat more than half the value $\tau = 2.3$, which characterizes the mass distribution of a system at the critical point in the liquid-gas phase diagram [Fish 67, Wils 71].

The charge distributions and the power law fits for the data measured at mid-impact parameter collisions, $0.35 < \hat{b} < 0.45$, are also shown in figure 4.12. Figure 4.13 show the corresponding values for the extracted slope parameter τ as a function of the incident energy. The values taken from these measurements follow the same trends as the central collisions.

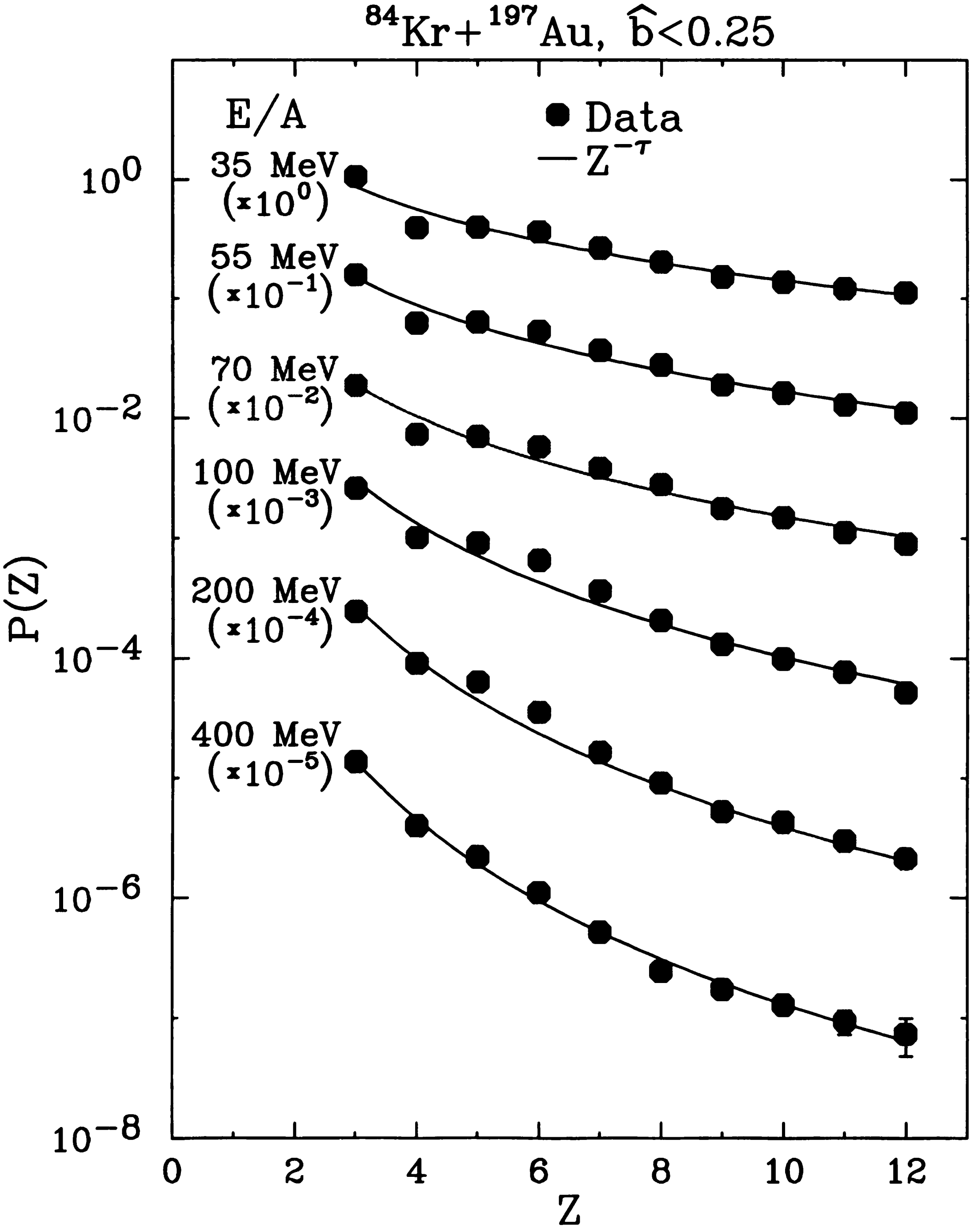

Figure 4.10 The probability of emitting a fragment of charge, Z, per central collision at the six incident energies. The solid dots are the experimental data points. The statistical uncertainties of the data are smaller than the data points. The solid line is the power law fit.

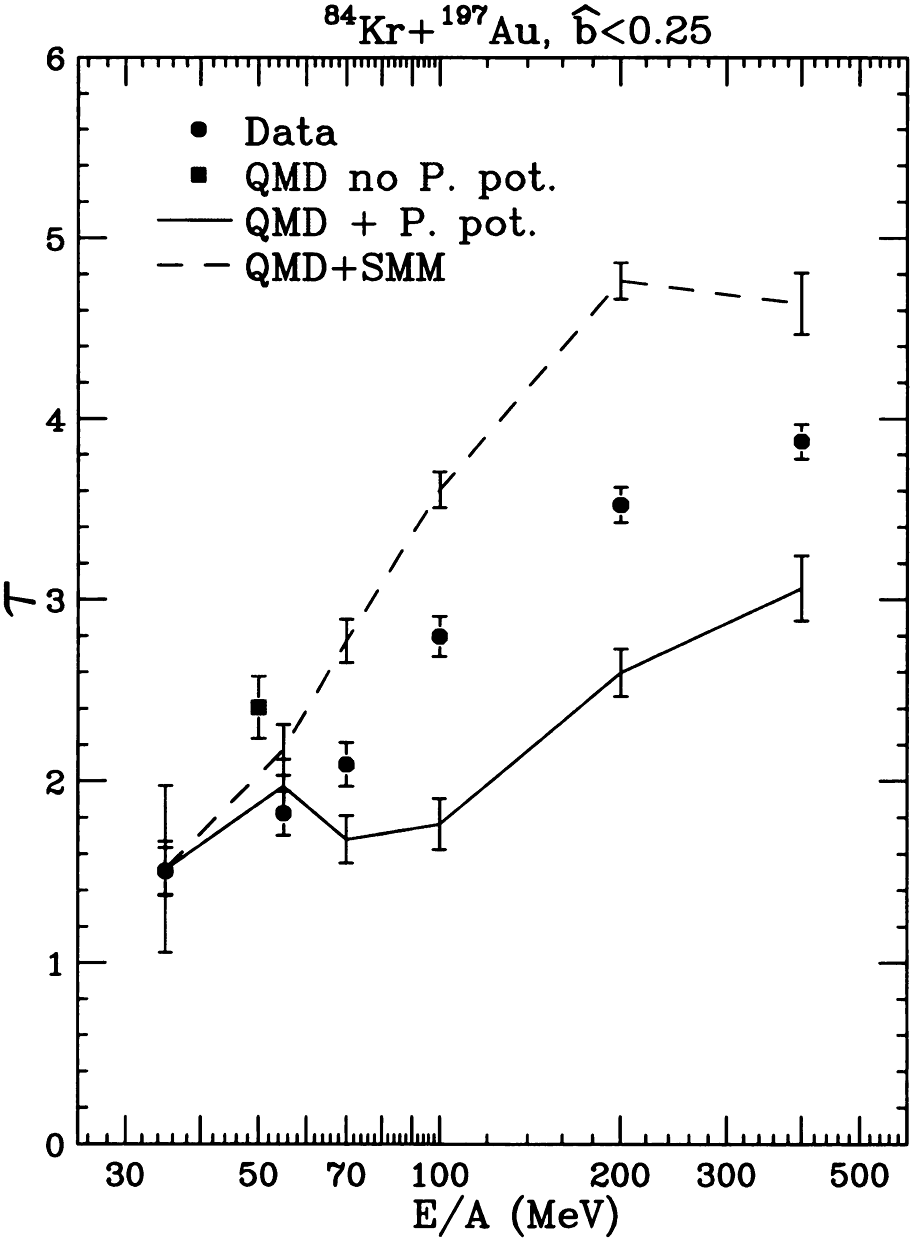

Figure 4.11 Comparison of the energy dependences of the charge distribution exponent τ from the data to QMD and QMD+SMM calculations for central ^{84}Kr + ^{197}Au collisions. The solid line describes the τ values from the QMD calculations using the Pauli potential. The dashed line describes the τ values from QMD+SMM calculations. The solid square is the τ value at E/A = 50 MeV from a QMD calculation that does not use the Pauli potential. The solid points are values for τ extracted from the experimental data.

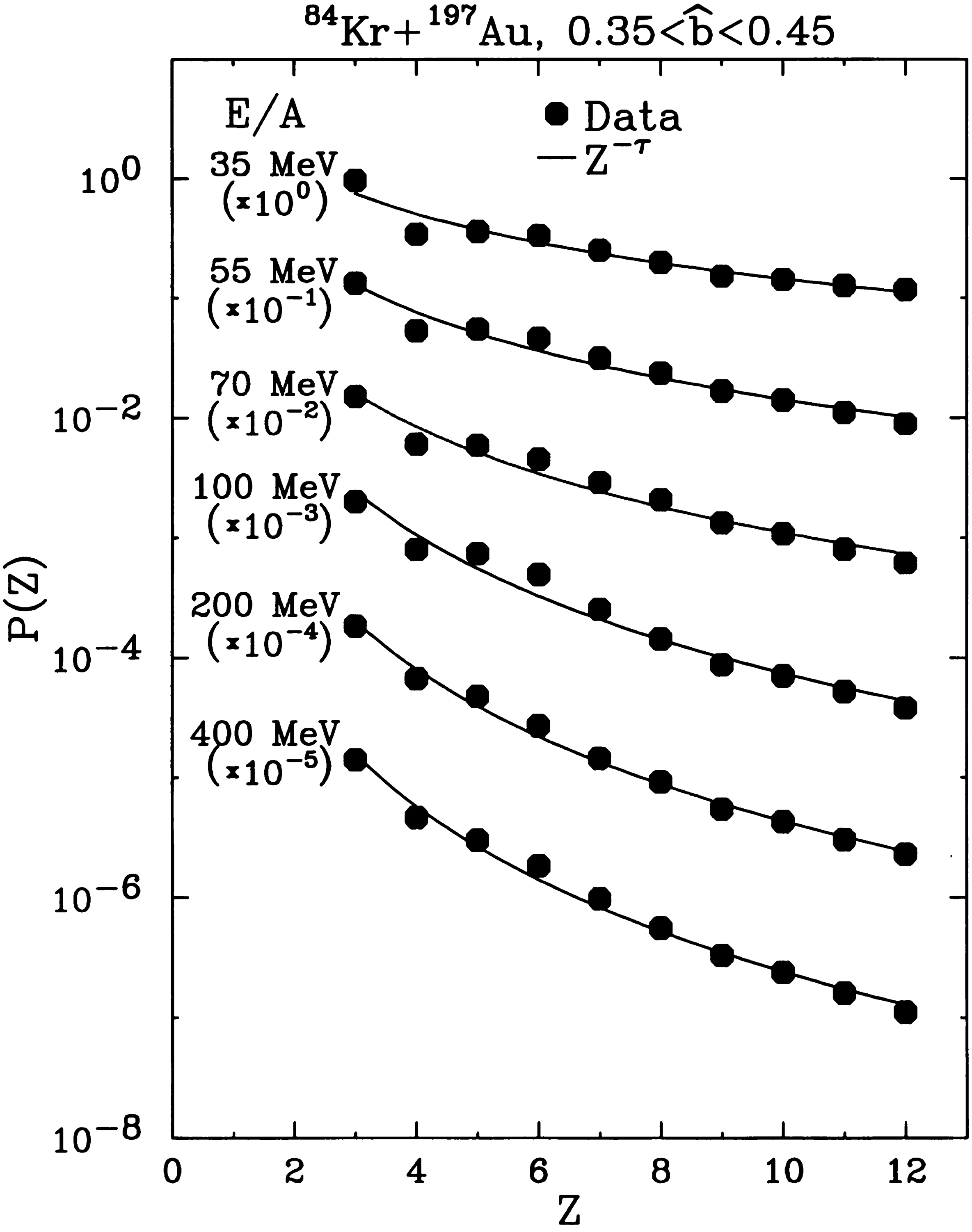

Figure 4.12 The probability of emitting a charge, Z, per mid-impact parameter collision at the six incident energies. The solid dots are the experimental data points. The statistical uncertainties of the data are smaller than the data points. The solid lines are the power law fits.

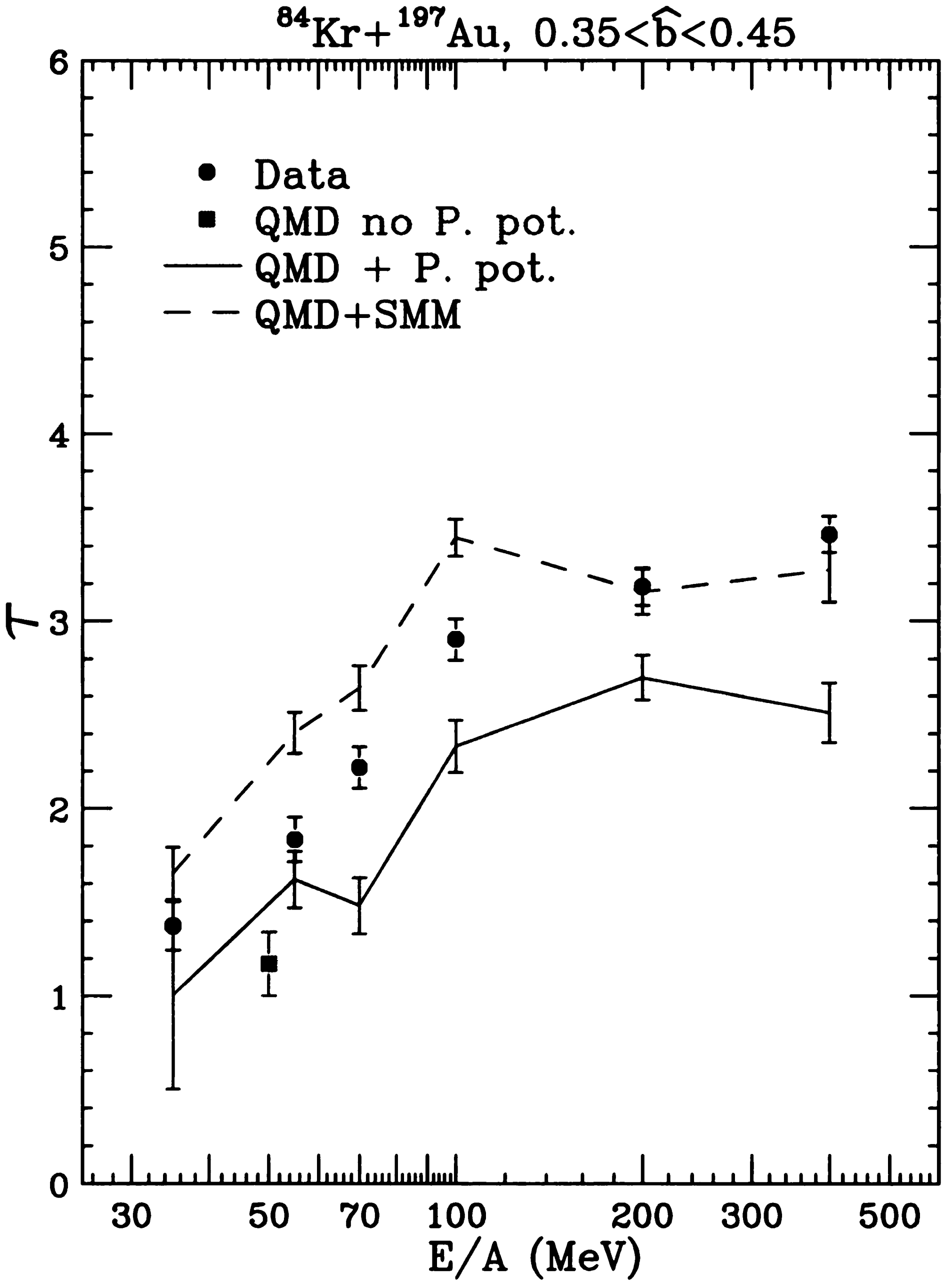

Figure 4.13 Comparison of the energy dependences of the charge distribution exponent τ from the data to QMD and QMD+SMM calculations for mid-impact parameter ^{84}Kr + ^{197}Au collisions. The solid line describes the τ values from the QMD calculations using the Pauli potential. The dashed line describes the τ values from QMD+SMM calculations. The solid square is a τ value at E/A = 50 MeV from a QMD calculation that does not use the Pauli potential. The solid dots are values for τ extracted from the experimental data.

4.3.2 Comparisons with QMD Calculations

Classical molecular dynamics simulations like those of reference [Pan 95], can reproduce the monotonically increasing values for τ. Because nuclei are quantal systems, it is relevant to know whether similar agreement can be obtained with molecular dynamics calculations which attempt to respect the Pauli exclusion principal. As mentioned in section 4.2.2 and 4.2.3, there are difficulties with the present semi-classical molecular dynamics calculations. To further illustrate these problems, we performed analogous fits of the charge distribution predicted by the Quantum Molecular Dynamics model, QMD, of reference [Peil 92, Peil 93] in which the Pauli principle is modeled by a repulsive "Pauli potential" which acts in phase space.

Fits of these calculations for central collisions are depicted by the solid lines figure 4.11. These calculation show a much more gradual dependence of τ upon incident energy than which is experimentally observed. The solid square at E/A = 50 MeV in figure 4.11 shows the corresponding calculations without the Pauli potential as described in reference [Peil 89]. Calculations for the charge distribution using the code of reference [Goss 95], which also does not include a Pauli potential are not available. Figure 4.13 shows the corresponding calculations for the mid-impact parameter collisions. The trends of the experimental data and the QMD calculations with the Pauli potential are similar to those observed in the central collisions.

4.3.3 Comparisons with QMD+SMM Calculations

Discrepancies between theoretical and experimental fragment multiplicities and charge distributions at low incident energies may be traced to the production of hot residues within the QMD calculations. These residue do not decay by fragment emission due to their high classical heat capacities [Lync 92]. As mentioned previously, this problem can be relieved by allowing these residues to decay via statistical models [Bowm 92, Sang 92, Kono 93]. The input excitation energies and masses for the SMM calculations were taken from the QMD calculations at a elapsed reaction time of 200 fm/c.

The dashed lines in figure 4.11 are the results obtained for the central collisions when the decays of all fragments with $A \geq 4$ were calculated using the SMM [Peas 94, Botv 87, Bond 95], which contains a "cracking" phase transition at low density. The larger values for τ which characterize the QMD+SMM calculations indicate that the corresponding fragment charge distributions are much steeper than those experimentally observed, even for incident energies E/A = 55 and 70 MeV where the fragment multiplicities are well reproduced [Peas 94]. The dashed lines in figure 4.13 depict the results for the intermediate impact parameters. The trends initially observed in figure 4.11 for the central collisions are also observed at intermediate impact parameters.

4.3.4 Comparisons with SMM Calculations

Figure 4.14 shows a comparison between the values of τ obtained from the experimental data and those obtained from the SMM calculation presuming rotational (solid lines) and radial (dotted lines) flow. The excitation energies per nucleon, E^*/A, of the SMM calculations were essentially constrained by the slope parameters, τ, of the fragment charge distribution. These E^*/A values are smaller than the total available excitation energy per nucleon. This fact is reflected by the small values for f_E given in

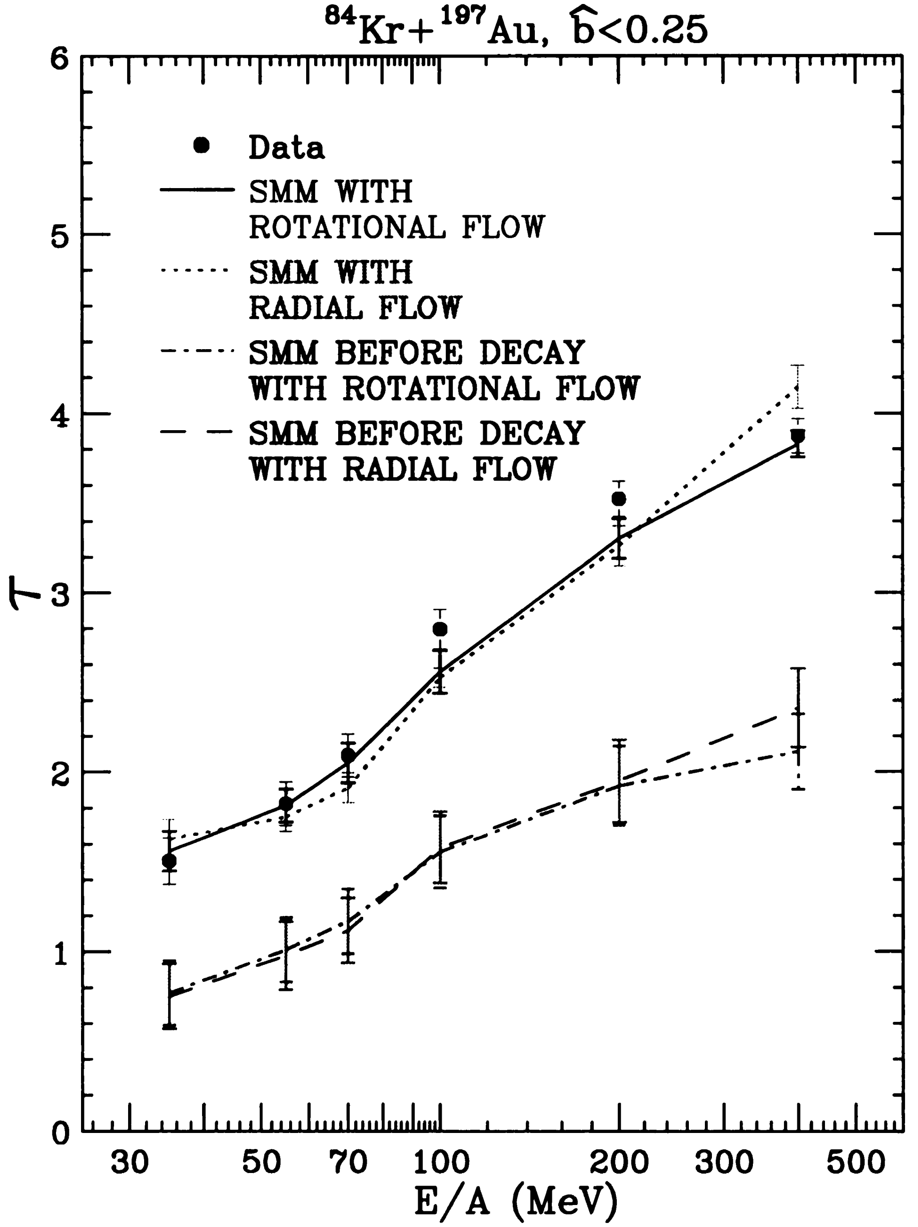

Figure 4.14 Comparison of the measured energy dependences of the charge distribution exponent τ from the data to SMM calculations for central ^{84}Kr + ^{197}Au collisions. The dashed and dashed-dotted lines describes the τ values from SMM calculations assuming radial and rotational flow, respectively, before secondary decay is allowed to occur. The dotted and solid lines describes the corresponding τ values for SMM calculations after secondary decay of the excited fragments. The solid dots are values for τ extracted from the experimental data.

table 4.1, which denote the ratios of the excitation energies per nucleon used in the SMM calculations to the total available excitation energies per nucleon at the various incident energies. The local thermal environment at breakup is much cooler than would be expected if the total available energy were thermalized.

Neither nature nor the SMM model have any difficulty producing fragmentation events with a slope parameter τ that is far less than the minimum value, $\tau = 2.3$, characteristic of a macroscopic (and therefore neutral) liquid-gas phase mixture at the critical point. These low values for τ become even more difficult to explain via critical exponent analyses [Camp 88, Mahi 88, Li 93, Gilk 94] when one considers the influence of secondary decay on the fragment charge distributions. Present critical exponent analyses require knowledge of the fragment charge distributions before secondary decay. Experimental measurements provide the charge distributions after secondary decay. The charge distributions after secondary decay are predicted to be steeper than the ones before decay.

To illustrate the magnitude of such effects, secondary decay was calculated with the SMM model and the charge distributions before and after the decay were compared. The dot-dashed and dashed lines in figure 4.14 depict the values for τ obtained from the calculated charge distributions before secondary decay for rotational and radial flow, respectively. Note that the differences between the τ values before decay and values given by the corresponding solid and dashed lines after decay are very large. Indeed the predicted τ values ($\tau < 1$) before secondary decay cannot be understood using the Fisher liquid drop phenomenology advocated by proponents of critical exponent analyses.

4.4 Multiplicity Dependence of the Charge Distribution

The behavior of fragment charge distributions may be significantly altered by the breakup geometry [Phai 93], and finite size effects [Phai 93] for the nuclear systems that can be produced and studied in the laboratory. Some of these alterations arise from the constraints imposed by conservation laws, and others from the time dependence imposed by the expansion and disintegration of the system into the surrounding vacuum.

The influence of charge conservation constraints upon the intermediate mass fragment (IMF) dependent charge distributions was studied in references [Phai 95, Ferr 96, More 95]. There, the fragment charge distributions were found to follow a simple exponential relationship:

$$P_{N_{IMF}}(Z) \propto \exp\left[-(\alpha_o + c \cdot N_{IMF})Z\right] \tag{4.2}$$

Here N_{IMF} is the multiplicity of intermediate mass fragments, and Z is the charge of a specific element. The variables α_0 and c are constants dependent on the system and its excitation energy. Studies with the percolation model [More 95] suggest that c should be inversely proportional to the charge of the prefragment ($c \propto \frac{1}{Z_0}$).

The dependence of c upon the total transverse energy of the system E_t has been investigated [Phai 95, Ferr 96, More 95]. The total transverse energy , E_t, is given by:

$$E_t = \sum_i E_i \sin^2\theta_i . \tag{4.3}$$

Here, E_i is the kinetic energy, θ_i is the scattering angle of the i-th particle and the summation runs over the detected particles in an event. These investigations suggest that c vanishes at small E_t and increases with E_t until reaching a saturation value. The $c = 0$ (liquid-gas coexistence) region was interpreted [More 95] as being due to the presence of a large residue with a mixed phase in the final state, which weakens the charge conservation constraints on the fragment distributions. The larger values of c were interpreted as reflecting constraints imposed by charge conservation for a final state consisting of a gas of nucleons, and fragments without a large residue [More 95].

The relationship between excitation energy deposition and charge conservation constraints can be explored in two ways. One is by varying the impact parameter at fixed bombarding energy and the other is by varying the bombarding energy at fixed impact parameter. Both techniques have their disadvantages. Collision geometries and source sizes vary significantly with impact parameter [Phai 92] while flow and reaction time scales vary significantly with incident energy [More 93, Bowm 93, Kim 91, Lace 93, Corn 95]. Figure 4.15 shows the extracted values of c as a function of the total transverse energy for the six incident energies. The values for c increases rapidly with E_t from the negative values observed in peripheral collisions at smallest E_t, except at the higher energies. It passes through zero and then increases slowly and comes to a maximum value between 0.02 to 0.03.

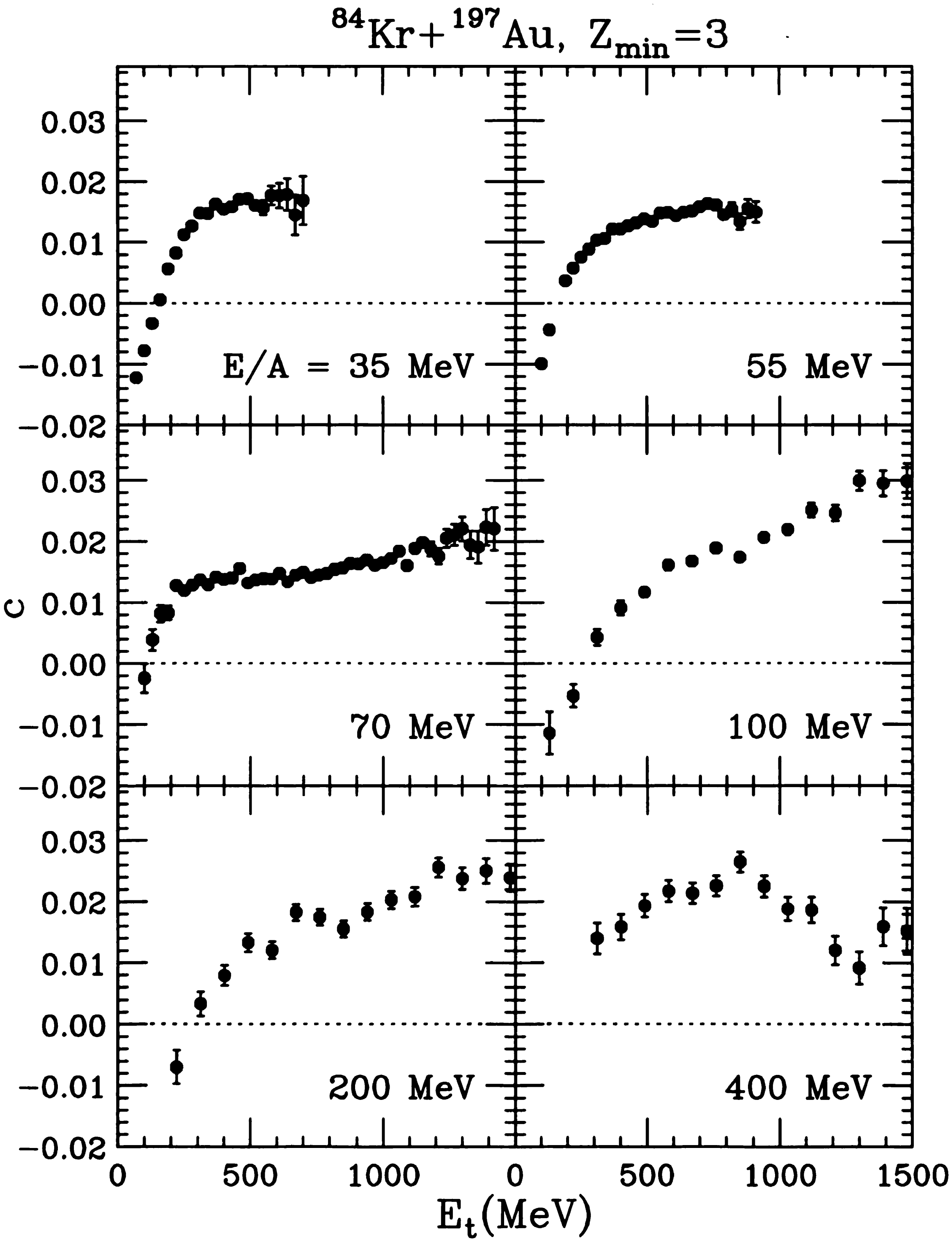

Figure 4.15 Charge conservation parameter *c* as a function of transverse energy E_t for the ^{84}Kr + ^{197}Au system at incident energies of E/A = 35 - 400 MeV.

The observation of $c < 0$ indicates that the fragment distributions become flatter as fragment multiplicity increases. Such a trend cannot be explained as being caused by charge conservation. Small E_t corresponds to peripheral collisions where the excitation energy is primarily carried away by undetectable neutrons and not by detectable charged particles. Thus the constraint of small E_t may be rather ineffective for constraining the excitation energy deposition at large impact parameters. Shifts in the mean impact parameter can occur at fixed E_t when additional gates are placed on the IMF multiplicity, because the IMF multiplicity is strongly impact parameter dependent at large impact parameters. This may be the cause of the negative c values.

To explore the magnitude of these cross gating effects, α-α azimuthal correlations were analyzed at a fixed E_t as functions of N_{IMF}. Correlations contain information about the angular momentum and directed transverse flow. Previous analyses have shown that these correlations are more anisotropic at larger impact parameters [Phai 92] consistent with larger angular momentum or "rotational flow" effects. Figure 4.16 shows the α-α correlations of ^{84}Kr + ^{197}Au reaction at E/A = 35 MeV for events with different values of the IMF multiplicity and for $E_t < 100$ MeV. These anisotropies decrease with N_{IMF}, consistent with smaller average impact parameter and larger average excitation energy deposition when the events have a large IMF multiplicity. This suggests that the negative values of c may be due to the impact parameter bias, and to the flatter charge distributions obtained from more central collisions [Kim 92]. The vanishing values for c in figure 4.15 and ref. [Phai 95, Ferr 96, More 95] only reflect a mixture between collisions with poorly defined impact parameter having a negative c and more central collisions having a

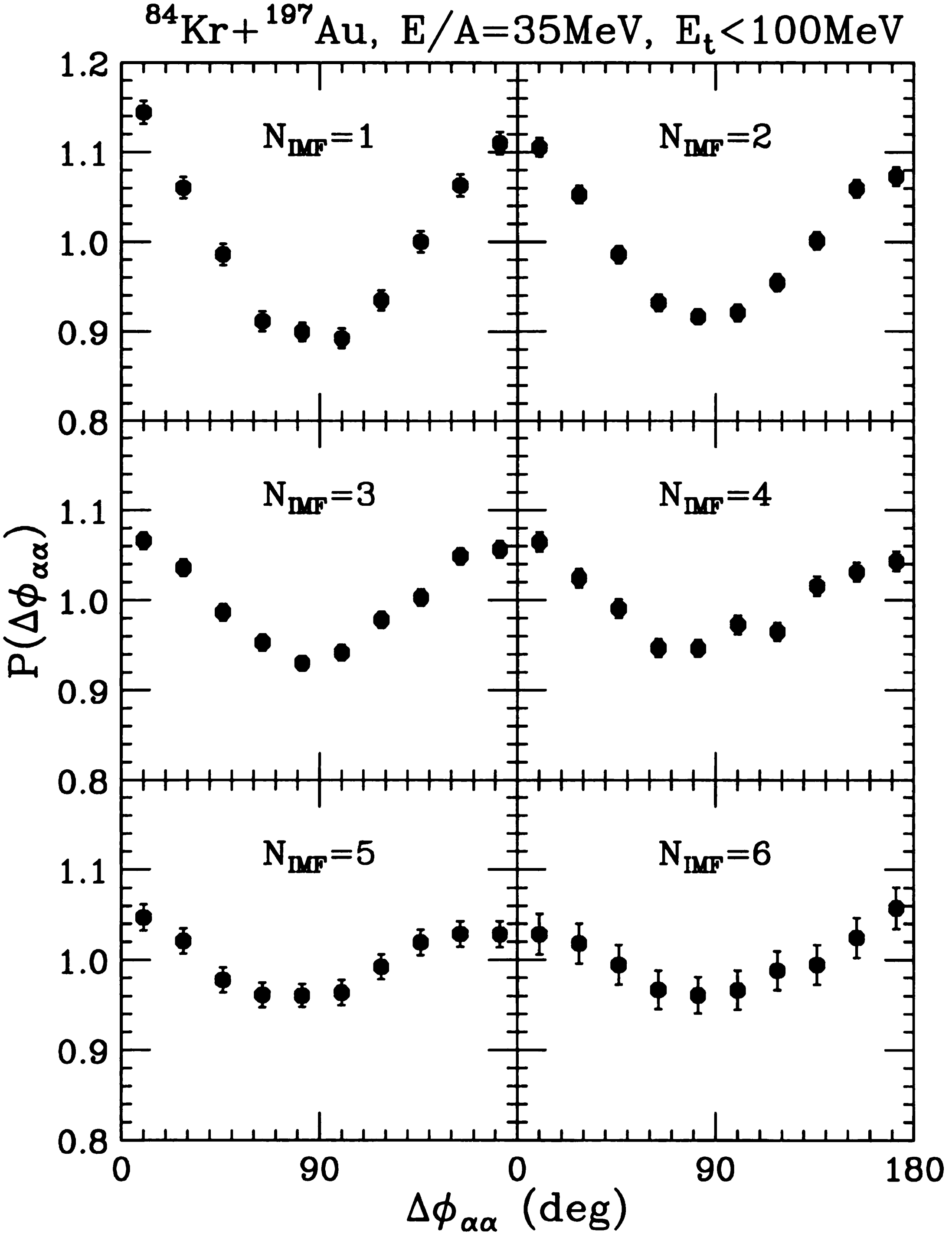

Figure 4.16 IMF multiplicity gated α-α correlation functions for the ^{84}Kr + ^{197}Au system at E/A = 35 MeV and E_t < 100 MeV.

positive c. Therefore $c = 0$ does not provide an definite signature for the co-existence region [More 95].

Figure 4.15 suggests that it may be easier to investigate c in central collisions where the charge distributions may be less sensitive to impact parameter and the experimental impact parameter selection may be sufficient. Thus we obtain values of c for a central collision gate of $\hat{b} < 0.25$ as before. The solid point in left panel of figure 4.17 are the values of c that come from fitting the multiplicity dependent charge distributions for fragments with $Z \geq 3$. These points are gradually increasing as the incident energy increases. This is consistent with the requirements imposed by charge conservation accompanied by the general increase in the charge particle multiplicity with incident energy and excitation energy deposition.

Such considerations are generally embodied in statistical multifragmentation models [Char 88, Frie 90, Gros 90, D'Ago 96]. To show how measurements of multiplicity dependent fragment charge distributions can provide meaningful constraints on statistical models, c was evaluated via SMM calculations. The SMM model pressumes the bulk fragmentation of a thermalized prefragment [Botv 87, Bond 95]. A more detailed description of this method was previously given in section 4.2.4 where predicted values for the fragment multiplicities and charged distributions are presented. Corresponding values for c from SMM calculations are plotted as the open points in the left panel of figure 4.17. (All theoretical calculations have been filtered through the experimental detection arrays.) The solid lines are drawn to guide the eye. In general, the

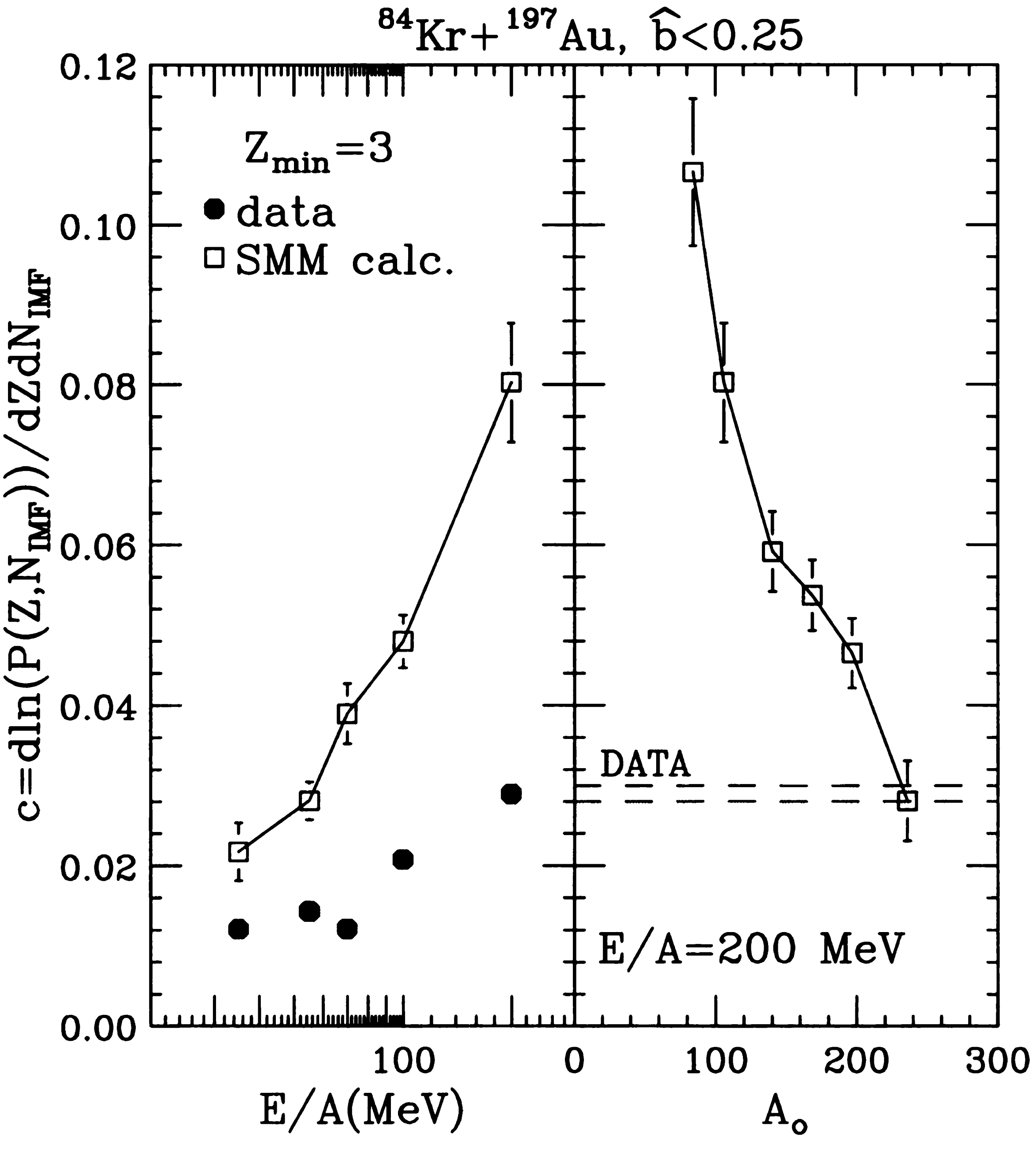

Figure 4.17 Left hand panel: *c* plotted as a function of incident energy and central collisions for data (solid points) and SMM predictions (open points). Right hand panel: *c* plotted as a function of source size used in the SMM calculations for E/A = 200 MeV. The dashed lines bound the value for *c* consistent with the experimental data.

predicted ***c*** is much higher than the experimental values indicating a stronger charge and energy conservation constraint within these calculations than is experimentally observed.

The source sizes, A_o , used in the SMM calculations were smaller than that of the total system. For the total system of ^{84}Kr + ^{197}Au, the source size is $A_o = 281$, but in the calculation $A_o = f_A \bullet 281$, where f_A is given in table 4.1 for the different energies. To show how much larger the calculated system should be in order to reproduce ***c***, A_o was increased in the calculations for ^{84}Kr + ^{197}Au at E/A = 200 MeV. While increasing A_o:

1) The excitation energies (8.5 MeV per nucleon) and therefore the charge distributions are held constant.

2) The expansion energy (11 MeV per nucleon) and therefore the mean transverse energies are held constant.

The right panel of figure 4.17 shows the resulting calculated dependence of ***c*** upon A_o. In order for the calculated values of ***c*** to agree with the experimental measurements (bound by the two dashed lines), the source size must be increased from 118 to 240. Unfortunately, an increase like this in source size would result in the SMM calculations predicting the mean number of IMF to be a factor of two larger than the experimental multiplicities. This analysis suggests that testing the charge conservation constraints contained in the multiplicity dependent fragment charge distributions provides unique and useful information about the size of the thermalized prefragment.

4.5 Collective Flow

The low values of f_E in table 4.1 suggest that a sizable fraction of the total energy is not thermalized. Experiments indicate that this energy is probably lost to collective motion. The energy spectra and consequently the detection efficiency for fragments in the experimental array are influenced by collective motion. Collective flow is not a feature predicted by the SMM model, and must be incorporated into the kinematics of the model by hand.

Previous investigations indicate that at low incident energies the attractive nuclear mean field can support a form of "rotational" flow [Tsan 86, Botv 95]. At higher incident energies the rotational flow decreases and flow becomes primarily outward or "radial" in direction [Jeon 94, Hsi 94]. This "radial" flow is caused by pressure from nucleon-nucleon collisions and from the repulsive high density nuclear equation of state in the overlapping central region.

The dependence of the mean transverse energy, $<E_t>$, upon the fragment charge has been used [deSo 91] to experimentally constrain the collective flow. The mean transverse energy , $<E_t>$, is given by:

$$\langle E_t \rangle = \frac{\sum_i E_i \sin^2\theta_i}{\mathrm{N}} \tag{4.4}$$

Here E_i is the kinetic energy, and θ_i is the scattering angle of the i-th fragment, and N is the total number of fragments of a specific charge. Experimental values of $<E_t>$ for central collisions, $\hat{b} < 0.25$, are shown as the solid points in figure 4.18 for the different

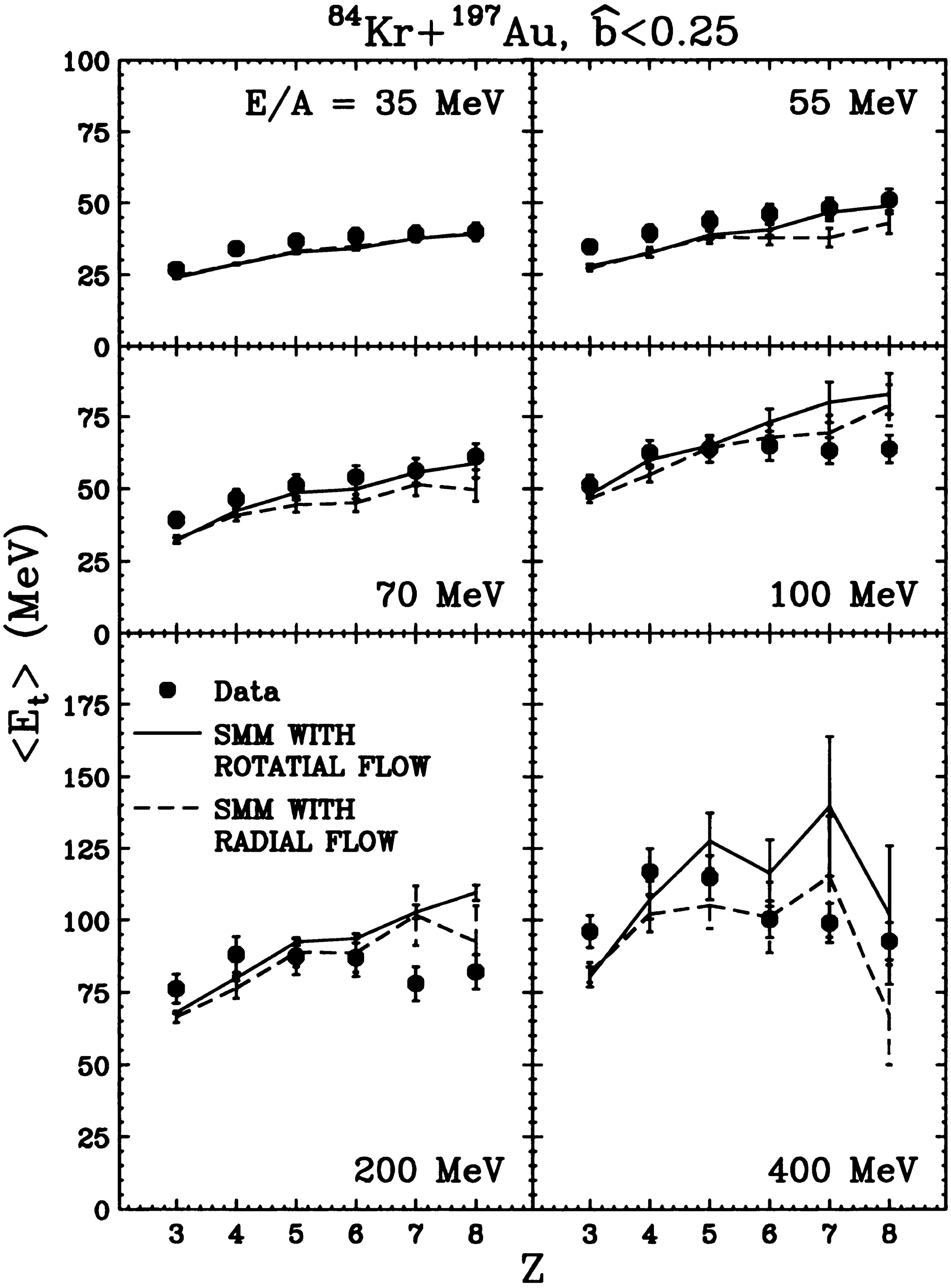

Figure 4.18 Comparison of the measured mean transverse energy, $<E_t>$, (solid points) to SMM calculations with radial (dashed lines) and rotational (solid lines) flow as a function of fragment charge at E/A = 35, 55, 70, 100, 200, and 400 MeV and $\hat{b} < 0.25$.

incident energies. As previously mentioned, SMM model calculations were performed with excitation energies per nucleon, equilibrium source sizes, and collective flow velocities chosen to optimize the agreement with the experimental fragment charge distributions, total fragment multiplicities, and transverse energies. Table 4.1 contains the values of the parameters used in these calculations. The dashed and solid lines in figure 4.18 show the mean transverse energies from SMM calculations with collective radial and rotational flow velocities respectively. In the calculations, the mean rotational flow energy per nucleon $<E_{rot}/A>$ and the mean radial flow energy per nucleon $<E_r/A>$ were chosen to provide the same transverse energy. This can be achieved by setting $2<E_r>/3 = <E_{rot}>/2$.

Figure 4.19 shows values for $<E_t>$ calculated by the QMD model with (solid lines) and without (solid squares) the Pauli potential. Hybrid QMD+SMM calculations are shown by the dashed lines. In these calculations, the collective flow is a prediction of the molecular dynamics solutions of the A-body equations of motion. Clearly the model underestimates the transverse energies at E/A > 55 MeV. This shows that the experimental data displays a transverse expansion that the fragments produced by QMD and QMD+SMM models do not. This failure is probably related to the inability of the models to reproduce the observed preequilibrium fragment emission.

4.6 Collective Expansion

It is impossible to reproduce the large fragment multiplicities shown in Figure 4.9 from statistical models without presuming that the system has expanded to subnuclear density. The SMM model uses a typical breakup density of about 1/6 of normal nuclear

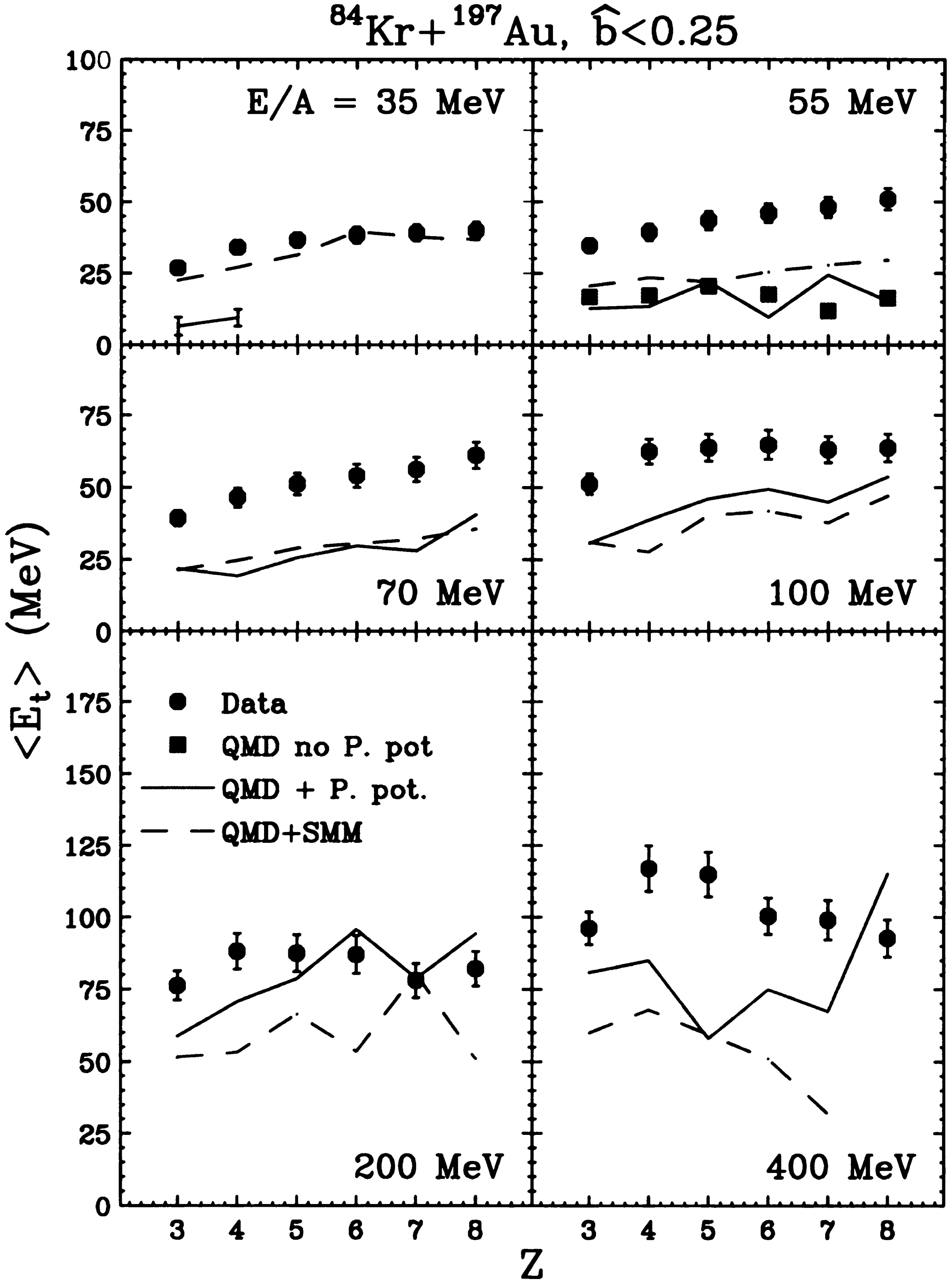

Figure 4.19 Comparison of the measured mean transverse energy, <E$_t$>, (solid points) to QMD calculations without the Pauli potential (solid squares) at E/A = 50MeV, QMD and QMD+SMM calculations with the Pauli potential (solid and dashed lines, respectively), as a function of fragment charge at E/A = 35, 55, 70, 100, 200, and 400 MeV and $\hat{b}$ < 0.25. Note, charged particles are not produced with Z > 4 within the QMD model for 35 MeV at this reduced impact parameter.

matter density. Break up densities as large as 1/3 of normal nuclear matter density can be used by the SMM model. Larger densities are not compatible with the SMM model, because SMM and similar models require that the fragments do not overlap at breakup.

Slightly lower densities are possible, but presuming an equilibrium decay at very low densities is not credible. However, the actual lower limit on the density is not known. For a systems to undergo a bulk fragmentation at a reasonable value of the density, it is necessary for the systems to expand over a short timescale. This reasoning leads to the idea that there is some collective expansion in the reaction.

Direct evidence for a collective expansion has been obtained for mass symmetric ^{197}Au + ^{197}Au collisions by fitting the fragment energy spectra. This was done by fitting with a source parameterization that presumes the superposition of a self-similar radial expansion and random (thermal) motion [Hsi 94]. Alternatively, similar information has been obtained by comparing the mass dependence of the mean fragment energies in the center of mass system with the expectations of models that superimpose a thermal breakup upon a self similar radial expansion [Jeon 94]. In either analysis, roughly 1/3 to 1/2 of the total energy per nucleon in the center of mass system is found to be carried away by the collective expansion. The open diamonds in figure 4.20 represent the mean collective radial expansion velocities extracted for the ^{197}Au + ^{197}Au system at E/A = 100 and 250 MeV by Wen Chien Hsi [Hsi 95]. The horizontal coordinate of the plot is the energy per nucleon of a participant source calculated from the geometrical overlap of projectile and target nuclei. For symmetric systems, it coincides with the total incident kinetic energy per nucleon in the center of mass system. The open circles depict mean

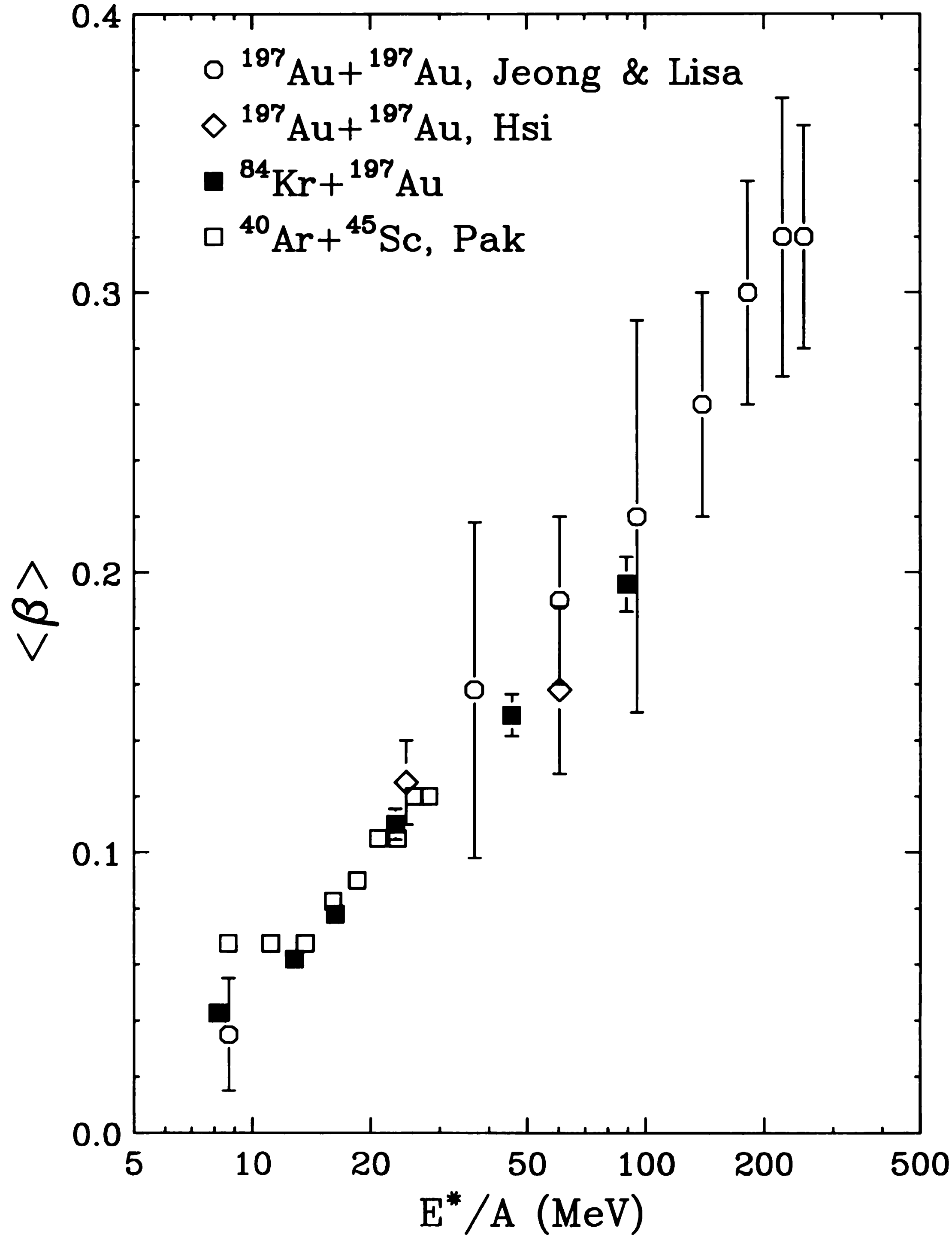

Figure 4.20 The mean collective velocity. <β>, versus the excitation energy per nucleon, E*/A of the participant source. The solid squares are from the analysis of the ^{84}Kr + ^{197}Au system. The other data are described in the text.

collective radial velocities extracted from light particle spectra measured in central Au+Au collisions at even higher incident energies [Lisa 95].

In mass asymmetric systems, like the one studied in this dissertation, moving source fits require more parameters than for symmetric systems, since they lack symmetry (on the average) between the emission in the projectile and target spectator domains. The results for collective expansion derived from thermal approaches, like the SMM, may provide a more straightforward estimate of the collective expansion velocity. The solid squares in the figure show the mean radial expansion velocity for the ^{84}Kr+^{197}Au system calculated according to $\langle\beta\rangle = 1.37 \cdot \left[\langle E_r\rangle / \left(m_N c^2\right)\right]^{1/2}$, where m_N is the nucleon mass, as a function of the excitation energy per nucleon of the participant source. Also shown are the flow values obtained for ^{197}Au + ^{197}Au collisions by Jeong et al. [Jeon 94] (open circles) and for ^{40}Ar+^{45}Sc collisions by Pak et al [Pak 96] (open squares). These systematics suggests that radial flow is essential determined early on in the collision by the conditions that prevail in the region of initial overlap of projectile and target nuclei.

Chapter 5

Conclusion

At the outset of this dissertation work, little was known about the impact parameter or energy dependence of multifragmentation. While both dynamical and statistical models for the fragmentation process had been developed, there was little experimental data to constrain them. The existence of multifragmentation had already been demonstrated in central collisions of Au + Au at E/A = 200 MeV. The results of dynamical QMD calculations were roughly consistent with the Au + Au measurements. Comparisons between the various models and various inclusive experimental fragmentation data were also made. It was found that models which predicted a multifragmentation decay and those which predicted the evaporative emission of one or two fragments were both successful in reproducing much of the inclusive experimental data. Information concerning the actual multiplicities of fragments could have distinguished these models, but was unavailable.

By the summer preceding the dissertation measurements, information confirming the existence of multifragmentation in central Xe + Au and semi-central Au + C, Al, and Cu collisions became available. Questions concerning the optimal incident energy for multifragmentation studies in central collisions became highly relevant. The present study addressed many of these questions.

5.1 Main results

Chapter Four contains many of the important conclusions of this dissertation. The most important result concerns the dependence of the fragment multiplicities for central collisions on the incident energy. There was a maximum at higher energies in the fragment multiplicity when the incident energy is about 100 MeV and a subsequent decrease with incident energy, consistent with the onset of nuclear vaporization. This observation clearly shows that most of the interesting energy range needed for nuclear multifragmentation measurements is accessible with beams at the NSCL.

5.1.1 Fragment Yields

This experimental data allows comparisons with theoretical models. Of such models, the most logical candidates for comparison were molecular dynamics models such as the Quantum Molecular Dynamics (QMD) model of the Frankfurt-Nantes collaboration [Aich 86, Peil 89]. When this dissertation was initiated, the Frankfurt group had abandoned the original formulation of the QMD model in favor of a model which included a Pauli potential which repelled nucleons from each other in phase space. Due to problems in describing the statistical decays of hot reaction residues that may be related to the classical heat copacities of the QMD nuclei. The Frankfurt group later added a secondary decay stage to the QMD model creating the dynamical-staticistical hybrid QMD+SMM model. Comparisons of this hybrid model to the measured fragment multiplicities are given in figure 4.8. Reasonable agreement between experimental and theoretical multiplicities are observed at low incident energies where the fragments are predicted to originate principally from the multifragment decay from a single large equilibrated composite residue. Within these hybrid simulations, the decay of this residue is calculated via the Statistical Multifragmentation Model (SMM) model of the Copenhagen-Moscow group [Bond 85, Botv 87] wherein the yields of the various emitted species are produced within an expanded and equilibrated system undergoing a "cracking phase transition". At higher incident energies, fragments are produced via the QMD model during a rapid non-equilibrium expansion. Many of these fragments are too highly excited to survive the secondary decay stages, however, and the predicted fragment yields fall far below the experimental values. The predicted fragment charge distributions fall more steeply with fragment charge than the measured ones as well.

Direct comparisons with the results of the SMM model were made to assess whether the discrepancies with the QMD+SMM model calculations were essentially due to an incorrect prediction by the QMD model for the excitation of the system during the non-equilibrium initial stages of the collision. Excellent agreement with the fragment charge distributions for central collisions were obtained by presuming an excited prefragments with total charges, masses, expansion velocities and excitation energies as free parameters. Excellent agreement with the measured fragment multiplicities, charge distributions and mean transverse energies were thereby obtained. The presumed values of the total mass and excitation energy of the equilibrated systems, however, were significantly less than half of that available raising questions about the presumption in the model that the early non-equilibrium stages produced a negligible fraction of the observed fragments.

5.1.2 Charge Distributions

The dependence of the fragment charge distributions upon the fragment multiplicity was used to further test the SMM. This observable is sensitive to constraints imposed upon the multifragment decay configuration by charge conservation. Using a method developed by the LBL group [More 75], where the charge conservation constraints are related to a parameter *c*, the multiplicity dependence of the fragment charge distributions was analyzed for the experimental data and for the SMM model calculations, (which reproduced the average experimental charge distributions). The values for *c* from the SMM model greatly exceeded the values for *c* obtained from the experimental data. This result is consistent with the conclusion that SMM model presumes an equilibrated prefragment that is much too small.

Some consideration was given to the incident energy dependence of the measured fragment charge distributions. To discuss such trends compactly, these charge distributions were parameterized by power law distributions of the form $Y(z) = C \bullet Z^{-\tau}$. In contrast to measurements for smaller total systems and the naive expectations of advocates of the Fisher liquid drop phenomenology, the measured values for τ increase monotonically with incident energy. Exploration of this effect within Lattice Gas Model (LGM) calculations [Pan 95] reveals that this is a likely consequence of the destabilizing Coulomb interaction, an feature that has been also observed in studies within the SMM model [Mish 96]. If true, this raises serious questions about interpretations within models like the Fisher liquid drop model, which attribute the abundant production of fragments to clustering near the critical point in the liquid-gas phase diagram. Clearly, long range interactions like the Coulomb force make contributions to the excitation energy which do not scale as intensive quantities. To the extent that the multifragment decay configurations reflect the Coulomb interaction, the result density fluctuations will not be scale invariant as expected near the critical point.

Detailed examination of SMM calculations reveal other significant shortcomings of critical exponent analyses when using the Fisher liquid drop phenomenology. These analyses require that the observed fragment distributions are an accurate reproduction of the fragment distributions at breakup. But between breakup and final detection, the highly excited fragments predicted in thermal approaches will decay. Investigations of these secondary decay corrections with SMM calculations shown in section 4.2.4 reveal that the charge distributions before the secondary decay are flatter than those after secondary decay. Thus, "critical exponents" extracted by fitting the observed fragment distributions have nothing to do with those that characterize the fragment distributions at breakup. Therefore they cannot be compared directly to the predictions of Fisher liquid drop theory or to percolation theory without extensive corrections for secondary decay.

5.1.3 Collective Expansion

Indirect evidence for expansion in the data can be found in the comparisons of statistical predictions to experimental data for the fragment multiplicities and charge distributions. More direct indications of expansion can be obtained from the examination of the fragment momentum distributions or the energy and angular distributions. Such evidence was obtained by examining the energy spectra obtained for symmetric Au + Au collisions in 1994 [Hsi 95]. Alternatively, evidence for the role of collective expansion can be obtained by comparing the measured mean fragment energies to statistical calculations with and without the superposition of a collective flow velocity [Jeon 94, deSo 93].

In this dissertation the mean transverse energies of fragments were so compared to SMM calculation while superimposed thermal motions upon a collective radial expansion. The values for this collective radial expansion velocity were then extracted. Comparison of these values to those obtained for central collisions between symmetric ^{197}Au + ^{197}Au collisions indicates that a common systematics can be found if all the data are plotted as a function of the excitation energy of a putative participant source. This indicates that the collective expansion is determined in the early stage of the collision by the dynamics in the region where nucleons from the projectile and target are overlapping.

5.2 Future Outlook

Putting into perspective the systematics obtained in this dissertation, a persuasive case can be made for the exploration of ^{84}Kr + ^{197}Au collisions and other similar systems at E/A < 100 MeV, i.e. at energies less than that corresponding to the maximum in fragment production. At higher energies, our measurements indicate that systems expand rapidly and there may be difficulties in determining the extent to which the reduction in fragment multiplicities can be better understood as being due to a purely thermal vaporization or as being due to low cluster production rates within a region of low phase space density [Kund 95]. At the lower energies, on the other hand, there is considerably more elapsed time between the initial overlap of projectile and target at the final breakup, making it more likely that local thermal equilibrium can be achieved.

In this lower energy domain, it is very important to determine whether simple freezeout approximations like those employed by the SMM model are sufficient or should be replaced by rate equation approaches like that employed in conventional compound nuclear decay or the Expanding Evaporating Source (EES) model [Frie 83a]. If a region of validity or either approach can be determined, it becomes important to place constraints upon the excitation energy, and in the case of the bulk multifragmentation models like the SMM approach, information about the density at breakup. Such investigations will greatly further and hopefully conclude this quest to determine the thermal properties of hot and low density nuclear matter and its phase transitions.

Bibliography

[Aich 86] J. Aichelin and H. Stöker, Phys. Lett. **B176**, 12 (1986).

[Aich 88] J. Aichelin et al., Phys. Rev. **C37**, 2451 (1988).

[Aich 91] J. Aichelin et al., Phys. Rep. **202**, 233 (1991).

[Alar 86] J.Alarja et al., Nucl. Inst. and Meth. **A242**, 352 (1986).

[Alar 92] J.P. Alard et al, Phys. Rev. Lett. **69**, 889 (1992).

[Aldi 89] The ALADIN collaboration, Nachrichten GSI 02-89 of GSI at Darmstadt Germany 1988 (Unpublished).

[Amsd 75] A.A. Amsden et al., Phys. Rev. Lett. **35**, 905 (1975).

[Bade 82] A. Baden et al., Nucl. Inst. and Meth. **A203**, 189 (1982).

[Barz 86] H.W. Barz et al., Nucl. Phys. **A448**, 753 (1986).

[Barz 91] H.W. Barz et al., Nucl. Phys. **A531**, 453 (1991).

[Batk 92] G. Batko, J. Randrup and T. Vetter, Nucl. Phys. **A536**, 786 (1992).

[Baue 85] W. Bauer et al., Phys. Lett. **B150**, 53 (1985).

[Baue 92] W. Bauer et al., Phys. Rev. Lett. **69**, 1888 (1992).

[Baue 93] W. Bauer et al., Phys. Rev. **C47**, R1838 (1993).

[Baug 93] E. Bauge et al., Phys. Rev. Lett. **70**, 3705 (1993).

[Bauh 85] W. Bauhoff et al., Phys. Rev. **C32**, 1915 (1985).

[Bere 92] M. Berenguer et al., J. Phys. **G18**, 655 (1992).

[Bert 83] G. Bertsch and P. J. Siemens, Phys. Lett. **B126**, 9 (1983).

[Bert 87] G.F. Bertsch, W.G. Lynch and M.B. Tsang, Phys. Lett.**B189**, 384 (1987).

[Birk 64] J.B. Birks, *The theory and Practice of Scintillation counting,* P.2 (Pergamon Press, New York, 1964).

[Blum 91] Y. Blumenfeld et al., Phys. Rev. Lett. **66**, 576 (1991).

[Boal 83] D.H. Boal Phys. Rev. **C28**, 2568 (1983).

[Boal 88a] D.H. Boal and J.N. Glosli, Phys. Rev. **C37**, 91 (1988).

[Boal 88b] D.H. Boal and J.N. Glosli, Phys. Rev. **C38**, 1870 (1988).

[Boal 88c] D.H. Boal and J.N. Glosli, Phys. Rev. **C38**, 2621 (1988)

[Boal 89] D.H. Boal et al., Phys Rev. **C40**, 601 (1989)

[Boal 90] D.H. Boal and James N. Glosli, Phys. Rev. **C42**, R502 (1990).

[Bogo 62] N. N. Bogoliubov, *Studies in Stastical Mechanics*, J. de Boer and G.E. Uhlenbeck Eds., **Vol. 1** (North-Holland, Amsterdam 1962). The BBGKY stands for Bogoliubov-Born-Green-Kirkwood-Yvon.

[Bond 85a] J.P. Bondorf et al., Nucl. Phys. **A443**, 321 (1985).

[Bond 85b] J.P. Bondorf et al., Nucl. Phys. **A444**, 460 (1985).

[Bond 94] J.P. Bondorf et al., Phys. Rev. Lett. **73**, 625 (1994).

[Bond 95] J.P. Bondorf et al., Phys. Rep. **257**, 133 (1995).

[Bord 93] B. Borderie et al., Phys. Lett. **B302**, 15 (1993).

[Botv 87] A.S. Botvina et al., Nucl. Phys. **A475**, 663 (1987).

[Botv 90] A.S. Botvina et al., Nucl. Phys. **A507**, 649 (1990).

[Botv 92] A.S. Botvina and I.N. Mishustin, Phys. Lett **B294** (1992).

[Botv 93] A.S. Botvina et al., Z. Phys. **A345**, 297 (1993).

[Boug 87] R. Bougault et al., Phys. Rev. **C36**, 830 (1987).

[Boug 88] R. Bougault et al., Nucl. Phys. **A488**, 255 (1988).

[Boug 89] R. Bougault et al., Proceeding of the Symposium on Nuclear Dynamics and Nuclear Disassembly, P.193 (1989).

[Bowm 91] D.R. Bowman et al., Phys. Rev. Lett. **67**, 1527 (1991).

[Bowm 92] D.R. Bowman et al., Phys. Rev. **C46**, 1834 (1992).

[Bowm 93] D.R. Bowman et. al., Phys. Rev. Lett. **70**, 3534 (1993).

[Bowm 95] D.R. Bowman et al., Phys. Rev. **C52** 818 (1995).

[Buja 85] A. Bujak, et. al., Phys. Rev. **C32**, 620 (1985).

[Camp 88] X. Campi, Phys. Lett. **B208** 351 (1988)

[Cava 90] C. Cavata et al., Phys. Rev. **C42**, 1760 (1990).

[Cebr 90] D. Cebra et al., Phys. Rev. Lett. **64**, 2246, (1990).

[Char 88] R.J. Charity et al., Nucl. Phys. **A483**, 371 (1988).

[Chen 88] Z. Chen and C.K. Gelbke, Phys. Rev. **C38**, 2630 (1988).

[Chit 83] C. B. Chitwood et al., Phys. Lett. **B131**, 289 (1983).

[Chit 86] C.B. Chitwood et al., Phys. Rev. **C34**, 858 (1986).

[Colo 92] N. Colonna, Nucl. Inst. and Meth. **A321**, 529 (1992).

[Corn 95] E. Cornell et al., Phys. Rev. Lett. **75**, 1475 (1995)

[Cser 86] L. P. Csernai and Kapusta, Phys. Rep. **131**, 223 (1986), and references therein.

[Curt 83] M.W. Curtain et al., Phys. Lett. **B123**, 289 (1983)

[Cuss 85] Y. Cusson et al., Phys. Rev. Lett. **55**, 2786 (1985).

[D'Ago 95] M. D'Agostino et al., Phys. Rev. Lett. **75**, 4373 (1995)

[D'Ago 96] M. D'Agostino et al., Phys. Lett. **B371**, 175 (1996)

[Dani 85] P. Danielewicz and G. Odynice, Phys. Lett. **B157**, 146 (1985).

[Dani 88] P. Danielewicz et al., Phys. Rev. **C38**, 120 (1988).

[Dani 91] P. Danielewicz and G.F. Bertsch, Nucl. Phys. **A553**,712 (1991).

[Dani 92] Pawel Danielewicz and Qiubao Pan, Phys. Rev. **C46**, 2004 (1992).

[deSo 90] R.T. de Souza et al., Nucl. Instr. and Meth. **A295**, 109 (1990).

[deSo 91] R.T. de Souza et al., Phys. Lett. **B268**, 6 (1991).

[deSo 93] R.T. DeSouza et al., Phys. Lett. **B300**, 29 (1993).

[Dors 88] C. Dorso and J. Randrup, Phys. Lett. **B215**, 611 (1988).

[Doss 85] K.G.R. Doss et al., Phys. Rev. **C32**, 116 (1985).

[Doss 87] K.G.R. Doss, et al., Phys. Rev. Lett. **59**, 2720 (1987).

[Fai 82] G. Fai and J. Randrup, J. Nucl. Phys. **A381**, 557 (1982).

[Fai 83] G. Fai and J. Randrup, Nucl. Phys. **A404**, 551 (1983).

[Faty 85] M. Fatyga et al., Phys Rev. Lett. **55**, 1376 (1985).

[Feld 90] H. Feldmeier, Nucl. Phys. **A515**, 147 (1990).

[Ferr 96] A. Ferrero et al., Phys. Rev. **C53**, R5 (1996)

[Fiel 87] D.J. Fields et al., Phys. Let. **B187** 257 (1987)

[Finn 82] J.E. Finn et al., Phys. Rev. Lett. **49**,1321 (1982).

[Fish 67] M. E. Fisher, Rep. Prog. Phys. **30** 615 (1967), and refs. therein.

[Fish 67] M.E. Fisher, Rep. Prog. Phys. **30** 615 (1967), and refs.therein.

[Fox 86] D. Fox et al., Nucl. Inst. and Meth. **A368**, 709(1996).

[Fox 93] D. Fox et al., Phys. Rev. **C47**, R421 (1993).

[Frie 83a] W.A. Friedman and W.G. Lynch, Phys. Rev. **C28**, 16 (1983).

[Frie 83b] W.A. Friedman and W.G. Lynch, Phys. Rev. **C28**, 950 (1983).

[Frie 88] W.A. Friedman, Phys. Rev. Lett. **60**, 2125 (1988).

[Frie 90] W.A. Friedman, et al., Phys. Rev. **C42**, 667(1990).

[Gale 87] C.B. Gale, G. Bertsch and S.D. Gupta, Phys. Rev. **C35**, 1666 (1987).

[Gelb 88] C.K. Gelbke and D. H. Boal, Rev. Mod. Phys. **60**, 33 (1988).

[Gilk 94] M.L. Gilkes et al., Phys. Rev. Lett. **73** 590 (1994)

[Gobb 93] A. Gobb et al., Nucl. Inst. and Meth. **A324**, 156 (1993).

[Gold 80] H. Goldstein, Classical Mechanics, Addison-Wesley Publishing Company (1980) p.106

[Gong 90] W.G. Gong et al., Nucl. Inst. and Meth. **A287**, 639 (1990).

[Good 84] A.L. Goodman et al., Phys. Rev. **C30**, 851 (1984)

[Goss 95] P.B. Gossiaux, and J. Aichelin, Rapport Interne SUBATECH - 95 - 04.

[Greg 87] C. Gregoire et al., Nucl Phys. **A465** 317 (1987)

[Gros 82] D.H.E. Gross et al., Z. Phys. **A309**, 41 (1982).

[Gros 85] D.H.E. Gross and Ciao-Ze Zhang, Phys. Lett. **B161**, 47 (1985).

[Gros 86] D.H.E. Gross et al., Phys. Rev. Lett. **56**, 1544 (1986).

[Gros 90] D.H.E. Gross et al., Rep. Prog. Phys. **53**, 605 (1990), and references therein.

[Gupt 67] A.K. Gupta and N. Nath, Nucl. Inst. and Meth. **53**, 352 (1967).

[Gust 88] H. Å Gustafsson et al., Modern Physics Letter A, Vol. **3**, No. **14**, 1323 (1988).

[Gutb 89a] H.H. Gutbrod, A.M. Poskanzer and H.G. Ritter, Rep. Prog. Phys. **52**, 1267 (1989).

[Gutb 89b] H.H. Gutbrod et al., Phys. Lett. **B216**, 267 (1989).

[Gutb 90] H.H. Gutbrod et al., Phys. Rev. **C42**, 640 (1990).

[Hage 92] K. Hagel et al., Phys. Rev. Lett. **68**, 2141 (1992).

[Harr 87] J.W. Harris et al., Nucl. Phys. **A471**, 241c (1987).

[Haus 52] W. Hauseer and H. Feshbech, Phys. Rev. **87**, 366 (1952).

[Hirs 84] A.S. Hirsch, et al., Phys. Rev. **C29**, 508 (1984).

[Hori 91] Hisashi Horiuchi, Nucl. Phys. **A522**, 257 (1991).

[Horn 92] D. Horn et al., Nucl. Inst. and Meth. **A320**, 273 (1992).

[Hsi 94] W.C. Hsi et al., Phys. Rev. Lett. **73**, 3367 (1994).

[Huan 63] Kerson Hunag, *Statistical Mechanics*, p69, John Wiley & Sons Inc, 1963.

[Hube 91] J. Hubele, et al. Z. Phys. **A340**, 263 (1991).

[Hube 92] J. Hubele, et al., Phys. Rev. **C46**, R1577 (1992).

[Jaca 87] B.V. Jacak et al., Phys. Rev. Lett. **51**, 1846 (1983).

[Jacq 83] H.E. Jacqaman et al., Phys. Rev. **C27**, 2782 (1983).

[Jeon 94] S.G. Jeong et al., Phys. Rev. Lett. **72**, 3468 (1994).

[Kämp 93] B. Kämpfer et al., Phys. Rev. **C48**, R995 (1993).

[Kamp 89] K.H.Kampert, J. Phys. G. Nucl. Part. Phys. **15**, 691 (1989).

[Kapu 95] J.I. Kapusta et al., Phys. Rev. **C51**, 90 (1995).

[Kauf 80] S.B. Kaufman and E.P. Steinberg, Phys. Rev. **C22**, 167 (1980).

[Kean 94] D. Keane et al., Preprint LBL-36370, September 1994.

[Kim 89] Y.D. Kim et al., Phys. Rev. Lett. **63**, 494 (1989).

[Kim 91a] Y.D. Kim et al., Phys. Rev. Lett. **67**, 14 (1991).

[Kim 91b] Y.D. Kim, PhD Thesis, Michigan State University, 1991.

[Kim 92] Y.D. Kim et al., Phys. Rev. **C45**, 338 (1992).

[Knol 79] Glenn F. Knoll, Chapter 10, *Radiation Detection and Measurement*, John Wiley & Son Inc.(1979).

[Koch 91] V. Koch et al., Nucl. Phys. **A532**, 317 (1991).

[Kono 93] J. Konopka, et al., Prog. Part. Nucl. Phys. **30** 301 (1993)

[Krus 85] H. Kruse et al., Phys. Rev. Lett. **54**, 289 (1985).

[Kuhn 93] C. Kuhn et al., Phys. Rev. **C48**, 1232 (1993)

[Kund 94] G.J. Kunde PhD thesis, Unversity Frankfort 1994.

[Kund 95] G.J. Kunde et al., Phys. Rev. Lett. **74**, 38 (1995).

[Kwia 95] K. Kwiatkowski et al., Phys. Rev. Lett. **74**, 3756 (1995).

[Lace 93] R.A. Lacey et al., Phys. Rev. Lett. **70**, 1224 (1993).

[Land 80] L.D. Landau and E.M. Lifshitz, *Statistical Physics* (Pegammon Press, New York, 1980), 3rd ed.

[Lato 94] V. Latora et.al., Phys. Rev. Lett. **73** 1765 (1994).

[Leif 93] Y. Leifels et al., Phys. Rev. Lett. **71**, 963 (1993).

[Lenk 86] R.J. Lenk and V.R. Pandharipabde, Phys. Rev. **C34**, 177 (1986).

[Lenn 31] J.E. Lennard-Jones, Proc. Cambridge Phi. Soc. **27**, 469 (1931).

[Li 93] T. Li et al., Phys. Rev. Lett. **70**, 1924 (1993)

[Lind 93] V. Lindenstruth, GSI-93-18, ISN 0171-45446, May, 1993.

[Litt 94] U. Littmark and J.F. Ziegler, *Handbook of Range Distributions for Energetic Ions in All Elements*, Vol. 6 of the *Stopping and Ranges of Ions in Matter*, ed. J.F. Ziegler (Pergamon, New York, 1980).

[Lync 87] W.G. Lynch, Ann. Rev. Nucl. Part. Sci. **37**, 493 (1987), and refs. therein.

[Lync 92] W.G. Lynch, Nucl. Phys. **A545**, 199c (1992).

[Lync 95] W.G. Lynch, Nucl. Phys. **A583** 471 (1995)

[Mahi 88] Mahi et al., Phys. Rev. Lett. **60**, 1936 (1988)

[Mana 62] W.W. Managan, IRE Trans. Nucl. Sci. NS-9(3), 8 (1962).

[Mari 70] Jerry B. Marion, *Classical Dynamics*, p220 (Academic Press Inc. 1970).

[Mekj 77] A.Z. Mekjian Phys. Rev. Lett. **38**, 640 (1977).

[Meye 78] D. Meyerhofer, J. Appl. Phys. **49**, 3993 (1978).

[Milk 93] U. Milkau et al., Z. Phys. **A346**, 227 (1993).

[Mish 96] I. Mishastin, private communication

[More 75] L.G. Moretto, Nucl. Phys. **A247**, 211 (1975).

[More 93] L.G. Moretto and G.J. Wozniak, Ann. Rev. Nucl. Part. Sci. **43**, 379 (1993).

[More 95] L.G. Moretto et al., Phys. Rev. Lett. **74**, 1530 (1995).

[Morr 78] D.J. Morrissey et al., Phys. Rev. **C18**, 1267 (1987).

[Müll 95] W.F.J Müller, J. Pochodzalla and W. Trautmann for ALADIN/LAND collaboration, GSI 03-95 (1995).

[Myer 82] W.D. Myers and W.J. Swiatecki, Ann. Rev. Nucl. Part. Sci. **32**, 309 (1982).

[Norb 78] E. Norbeck et al., Nucl. Inst. and Meth. **A262**, 546 (1978).

[Nord 28] L.W. Nordheim, Proc. Roy. Soc. **A49**, 689 (1928).

[Ogil 90] C.A. Ogilvie et al., Phys. Rev. **C42**, R10 (1990).

[Ogil 91] C.A. Ogilvie, et al., Phys. Rev. Lett. **67**, 1214 (1991).

[Pan 93] Q. Pan and P. Danielewizc, Phys. Rev. Lett. **70**, 2060 (1993).

[Pan 95] J. Pan and S. DasGupta, Phys. Rev. **C53** 1319 (1995)

[Peas 94] G.F. Peaslee et al., Phys. Rev. **C49**, R2271 (1994).

[Peil 89] G. Peilert et al., Phys. Rev. **C39**, 1402 (1989) and refrences therein.

[Peil 91] G. Peilert et al, Phys. Lett. **B260**, 271 (1991)

[Peil 92] G. Peilert et al., Phys. Rev. **C46**, 1457 (1992).

[Peil 93] G. Peilert et al, Dissertation Universitat Frankfurt, GSI Report 92-13 (1993).

[Phai 92] L. Phair et al., Nucl. Phys. **A548**, 489 (1992).

[Phai 93a] L. Phair et al., Nucl. Phys. **A564**, 453 (1993)

[Phai 93b] L. Phair et al., Phys. Lett. **B314**, 271 (1993)

[Phai 95] L. Phair et al., Phys. Rev. Lett. **75**, 213 (1995)

[Prat 95] S. Pratt et al., Phys. Lett. **B349** (1995)

[Pres 86] Williams H. Press, Brain P. Flannery, Saul A. Teukolsky and William T. Vttterling; Numerical Recipes The Art of Scientific Computing, Cambridge University Press 1989.

[Quin 59] A.R. Quinton et al., Phys. Rev. **115**, 886 (1959).

[Rabe 89] H.J. Rabe et al., Phys. Lett. **B196**, 439 (1987).

[Sain 84] Saint-Laurent et al., Nucl. Phys. **A422**, 307 (1984).

[Sang 92] T.C. Sangster et al., Phys. Rev. **C46**, 1404 (1991).

[Saue 76] G. Sauer, H. Chandra and U. Mosel, Nucl. Phys. **A264**, 221 (1976).

[Sche 74] W. Scheid et al., Phys. Rev. Lett. **32**, 741 (1974).

[Schl 87] T.J. Schlagel and V.R. Pandharipande, Phys. Rev. **C36**, 162 (1987).

[Schu 84] H. Schulz et al., Phys. Lett. **B147**, 17 (1984).

[Schw 93] C. Schwarz et al., p.248, NSCL/MSU Annual Report 1993.

[Siem 79] Philip J. Siemens and Joseph I. Kapusta, Phys. Rev. Lett. **43**, 1486 (1979).

[Siem 83] P.J. Siemens, Nature **305**, 410 (1983).

[Slat 75] John. C. Slater, *Solid-State and Molecular Theory: A Scientific Biography,* P92-95, Wiley-Intersience Publication 1975.

[Snep 88] K. Sneppen, et al., Nucl. Phys. **A480**, 342 (1988).

[Soba 83] L.G. Sobotka, Phys. Rev. Lett. **51**, 2187 (1983).

[Souz 94] S.R. Souza et al., Nucl. Phys. **A571**, 159 (1994).

[Stau 79] D. Stauffer, Phys. Rep. **54**, 1 (1979).

[StÖc 80] H. StÖcker, J. Maruhn and W. Greiner, Phys. Rev. Lett. **44**, 725 (1980).

[StÖc 83] H. StÖcker et al., Nucl. Phys. **A400**, 63c (1983).

[StÖc 86] H. StÖcker and W. Greiner, Phys. Rep. **137**, 279(1986), and references therein.

[Stor 58] R.S. Storey et al., Proceedings of the Phys. Society **72**, 1 (1958).

[Stra 90] D.W. Stracener et al., Nucl. Inst. and Meth. **A294**, 485 (1990).

[Sura 89] E. Suraud et al., Nucl. Phys. **A495**, 73c (1989).

[Trau 93] W. Trautmann et al., Z. Phys. **A344**, 447 (1993)

[Trip 93] R.K. Tripathi et al., Phys. Rev. **C47**, R935 (1993)

[Troc 85] R. Trockel, Prog. Part. Nucl. Phys. **15**, 225 (1985).

[Troc 89] R. Trockel et al., Phys. Rev. **C39**, 729, 1989.

[Tsan 84] M.B. Tsang et al., Phys. Lett. **148B**, 265 (1984).

[Tsan 86] M.B. Tsang et al., Phys. Rev. Lett. **57** 59 (1986)

[Tsan 91] M.B. Tsang et al., Phys. Rev. **C44**, 2065 (1991).

[Tsan 93a] M.B. Tsang et al., Phys. Rev. **C47**, 2717 (1993).

[Tsan 93b] M.B. Tsang et al., Phys. Rev. Lett. **71**, 1502 (1993)

[Uehl 33] E.A. Uehling and G.E. Uhlenbeck, Phys. Rev. **43**, 552 (1933).

[Valt 90] E. Valtonen et al., Nucl. Inst. and Meth. **A286**, 169 (1990).

[Vice 85] A. Vicentini et al., Phys. Rev. **C31**, 1783 (1985).

[Vrie 87] H. de Vries et al., Atomic data nd Nuclear data table **36**, 495 (1987).

[Wang 95] S. Wang et al., Phys. Rev. Lett. **74**, 2646 (1995).

[Waps 77] A.H. Wapstra and K. Bos, Nucl. Data table **19**, 175; **20**, 1 (1977).

[Weis 37] V.F. Weisskopf, Phys. Rev. **52**, 295 (1937).

[West 85] G.D. Westfall et al., Nucl. Inst. and Meth. **A238**, 347 (1985).

[Wien 93] T. Wienold, Dissertation Universitat Heidelberg, GSI Report 93-28 (1993).

[Wile 91] J.L. Wile et al., Phys Lett **B264** 26 (1991).

[Wils 71] K.G. Wilson, Phys. Rev. **B4** 3174, 3184 (1971).

[Wils 92] W.K. Wilson et al., Phys. Rev. **C45**, 738 (1992).

[Zhu 92] F. Zhu et al., Phys. Lett. **B282**, 299 (1992).

MICHIGAN STATE UNIV. LIBRARIES
31293015635844